THESIS FOR THE DEGREE OF DOCTOR OF PHILOSOPHY

Temperature dependent atomic-scale modeling of interfaces in cemented carbides

Martin A. Gren

Department of Physics
CHALMERS UNIVERSITY OF TECHNOLOGY
Göteborg, Sweden 2020

Temperature dependent atomic-scale modeling of interfaces in cemented carbides
Martin A. Gren
Göteborg, 2020
ISBN 978-91-7905-319-2

Doktorsavhandlingar vid Chalmers tekniska högskola
Ny serie nr 4786
ISSN 0346-718X

Department of Physics
Chalmers University of Technology
SE-412 96 Göteborg, Sweden
Telephone +46 31 772 10 00

Cover: A WC/Co phase boundary with a cubic thin film in a Ti-doped cemented carbide. The atoms are colored according to: C (black), Co (blue), Ti (green) and W (red). The atomic structure was generated with ASE[1] and the image rendered with BLENDER[2]. Typeset in XeLaTeX

Chalmers reproservice
Göteborg, Sweden 2020

Temperature dependent atomic-scale modeling of interfaces in cemented carbides

Martin A. Gren
Department of Physics
Chalmers University of Technology

Abstract

Material properties can now be calculated directly from first principles using density functional theory (DFT) which has a great predictive power and can, in cases that are difficult to approach experimentally, provide crucial insights on the atomic and electronic level. Such cases include the thermodynamics of interfaces and surfaces which are crucial factors for the structure and macroscopic properties of many materials, where cemented carbides are one example.

Cemented carbides, or hardmetals, are composite materials manufactured by means of powder metallurgy, where carbide and binder metal powders are mixed, pressed, and sintered into a dense material. In this way the material gets a unique combination of hardness from the carbide and toughness from the binder. Cemented carbide is, therefore, an excellent choice of material in application where high hardness, wear-resistance, and toughness are crucial.

In this thesis bulk, interface, and surface thermodynamics in cemented carbides are studied using DFT, but also using other atomistic descriptions derived from DFT including analytical bond order potential (ABOP), cluster expansions (CE) and force constant (FC) models. Further, free energies are calculated using methods such as thermodynamic and temperature integration from both molecular dynamics (MD) and Monte Carlo (MC) simulations, quasi-harmonic approximation (QHA), effective harmonic models (EHM) from ab-initio molecular dynamics (AIMD), surface stress for liquid surface free energy and calculation of work of adhesion from separation and joining simulations.

Wetting of WC surfaces and WC/WC grain boundaries is investigated in WC–Co and WC–Ni cemented carbides at elevated temperatures and it is concluded that, at liquid sintering temperatures, wetting of WC surfaces is only partial in C-rich materials while perfect in W-rich materials. Further, WC/WC grain boundaries are predicted to be stable also at liquid phase sintering temperatures. WC/WC grain boundary sliding is shown to be facilitated by infiltration of binder phase of only a few atomic layers proportion. Moreover, the hexagonal and cubic WC phases are investigated at high temperatures and a phase diagram is generated. Finally, the formation of thin cubic carbide films (complexions) in WC/Co phase boundaries is studied in both undoped and Ti-doped cemented carbides. These films are predicted at liquid phase sintering temperatures in both cases and also at solid state sintering temperatures in the Ti-doped case. In Ti-doped cemented carbides, the Ti atoms are found to mostly segregate to the second layer of the thin film and leave an essentially pure W layer towards Co.

Keywords: cemented carbides, hardmetals, WC-Co, density functional theory, analytical bond order potential, interfaces, complexions, wetting, free energies, phase diagram

LIST OF PUBLICATIONS

This thesis consists of an introductory text and the following papers:

I **Wetting of surfaces and grain boundaries in cemented carbides and the effect of local chemistry**
M. A. Gren and G. Wahnström
Materialia 8 (2019)
DOI: 10.1016/j.mtla.2019.100470

II **A computational study of the temperature dependence of interface and surface energies in WC–Co cemented carbides**
M. A. Gren, E. Fransson, and G. Wahnström
International Journal of Refractory Metals and Hard Materials 87 (2020)
DOI: 10.1016/j.ijrmhm.2019.105114

III **Molecular dynamics simulation of WC/WC grain boundary sliding resistance in WC–Co cemented carbides at high temperature**
M. V. G. Petisme, M. A. Gren, and G. Wahnström
International Journal of Refractory Metals and Hard Materials 49 (2015)
DOI: 10.1016/j.ijrmhm.2014.07.037

IV **Modeling of vibrational and configurational degrees of freedom in hexagonal and cubic tungsten carbide**
M. A. Gren, E. Fransson, M. Ångqvist, P. Erhart, and G. Wahnström
In manuscript

V **Modeling of thin cubic film thermodynamics in undoped WC–Co cemented carbides**
E. Fransson, M. A. Gren, and G. Wahnström
In manuscript

VI **Modeling of thin cubic film thermodynamics in Ti-doped WC–Co cemented carbides**
M. A. Gren, E. Fransson and G. Wahnström
In manuscript

Specification of my contribution to the appended papers:

I The author did all the calculations and wrote the paper.

II The author did the modeling of the work of adhesion for the WC/Co phase boundary and wrote the paper.

III The author did some of the calculations and contributed to the development of the methodology.

IV The author did all DFT calculations including the ab-initio molecular dynamics simulations, the modeling of the electronic free energy and was the main author of the paper. The development of the overall methodology was a joint effort.

V The author did all DFT calculations and co-wrote the paper. The search for suitable stackings and suitable vacancy sites was a joint effort.

VI The author did all DFT calculations and was the main author of the paper. The search for suitable stackings and suitable substitutional and vacancy sites was a joint effort.

Contents

1 Introduction

As the computational power of computers and the efficiency of the theoretical tools have increased rapidly in the last decades, atomistic simulation methods are becoming increasingly important in materials science. Density functional theory (DFT) now allows us to calculate material properties direct from first principles. It has a great predictive power and can, in cases that are difficult to approach experimentally, provide crucial insights on the atomic and electronic level. An example of such a case is interface and surface energies which are hard to measure experimentally and in most cases one has to rely on estimations. When DFT calculations becomes too expensive, it is common to use other, simpler, models which are fitted to DFT data. Such models include inter-atomic potentials and cluster expansions, and with these models both system sizes and the configuration space can be increased significantly. The prize to pay for this decreased computational cost is, however, a reduction in accuracy.

For many materials, where cemented carbides is one example, the thermodynamics of interfaces and surfaces are important factors for the structure and macroscopic properties. For example, wetting, which is a measure of the interfacial and surface energies in a system, is an important technological parameter for many material processes such as joining, solidification, and composite processing[3].

Cemented carbides, or hardmetals, are composite materials with a unique combination of high hardness and good toughness [4]. In materials the *hardness* (the ability to resist plastic deformation by a certain load) and the *toughness* (the ability to absorb energy by deforming plastically without failure) are two competing properties, i.e., a material usually is hard and brittle or tough and soft. In Fig. 1.1, the hardness vs. toughness for a variety of hard materials is shown. We see that the extremely hard diamond is also highly brittle and the high-speed steels (HSS) are tougher but lack in hardness. However, cemented carbides manages to be simultaneously very hard and tough, which makes them a unique class of materials.

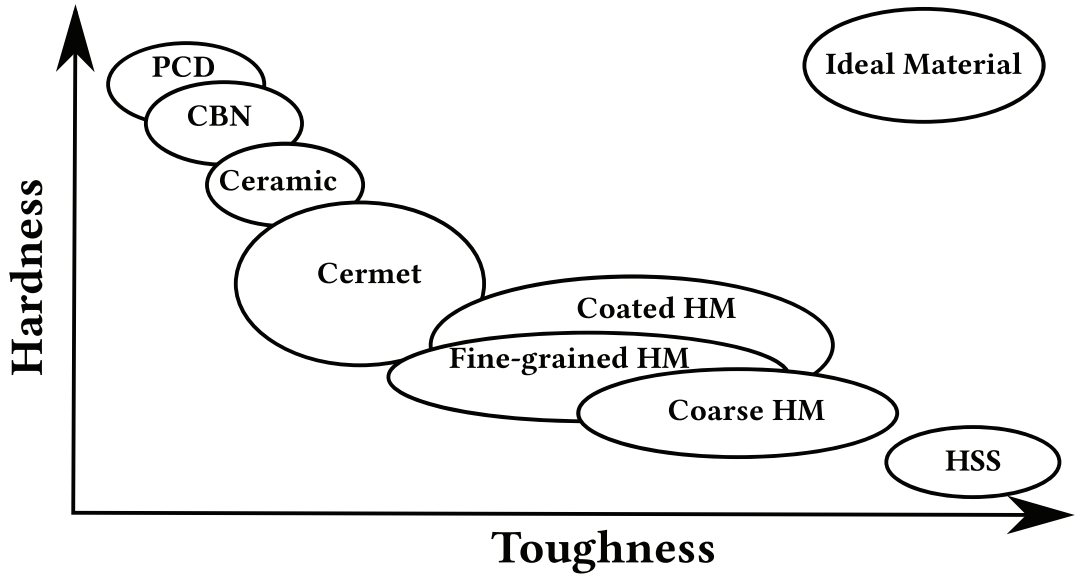

Figure 1.1: Sketch of the hardness vs. toughness for different types of hard materials. Here, PCD means polycrystalline diamond, CBN means cubic boron nitride, HM means hard metal and HSS means high-speed steel. Adapted from Figure 1 and 5 in Ref. [5].

Cemented carbides consist of two main components: a hard component, tungsten carbide (WC), and a more ductile binder component, which in a vast majority of cases is cobalt (Co). It is also common with several volume percent of cubic carbide additions (e.g. TiC, TaC and NbC) which then form a third phase, usually referred to as the gamma phase, in the material. These composite materials are manufactured by means of powder metallurgy, where carbide and binder powders are mixed, pressed, and sintered into a dense material [6]. In the microstructure of cemented carbides both the carbide (including the gamma phase if present) and binder grains are interconnected and build up two continuous inter-penetrating skeletons. In this way the hardness and toughness from the carbide phase(s) and the binder phase, respectively, are combined without too much loss, leading to both high hardness and toughness. Further, the hardness and toughness of the cemented carbide can be adjusted by varying the WC grain size, the binder content and/or the cubic carbide content.

These material properties makes cemented carbides an excellent choice of material in application where high wear-resistance and toughness are crucial [5]. Consequently, cemented carbide is the most widely used material for various metal machining operations such as turning, milling, drilling, threading, grooving, etc. A picture of a turning operation using the Sandvik Coromant CoroTurn® Prime tool is seen in Fig. 1.2. As the cemented carbides are of such technological importance, there is a great competition within the industry to improve and develop new grades. In the recent times cobalt has

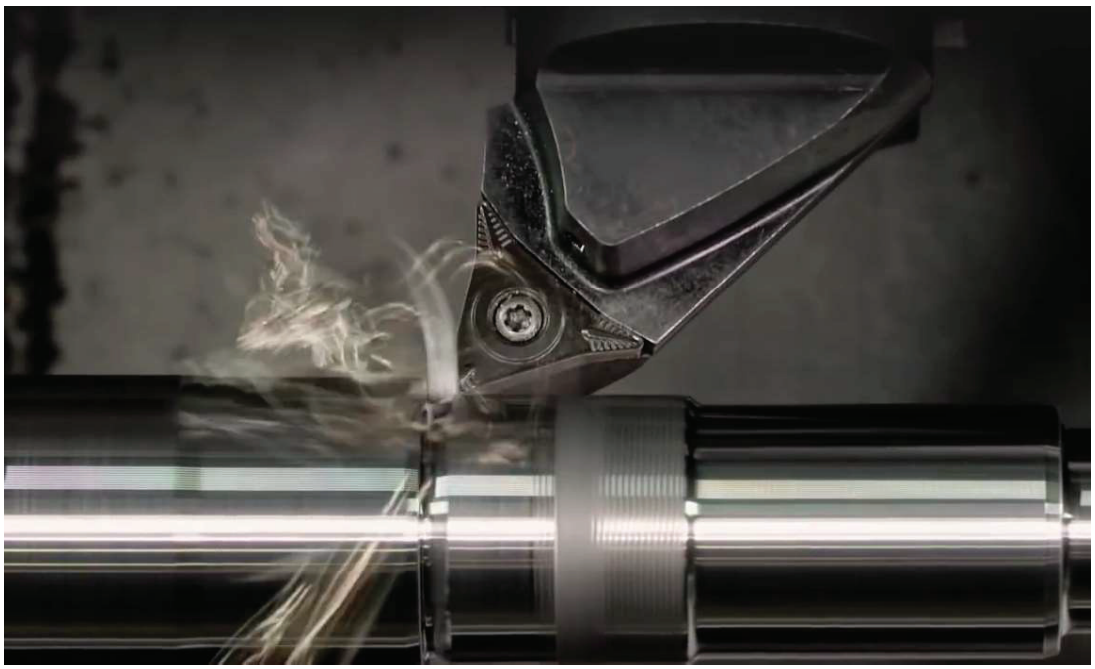

Figure 1.2: A turning operation using the Sandvik Coromant CoroTurn® Prime tool [7].

also been found to be toxic and carcinogenic, especially in the form of (WC–Co) hard-metal dust [8]. There is, therefore, also a large interest in replacing Co as the primary binder phase.

When studying interface and surface thermodynamics there are a lot of degrees of freedom that need to be handled and the computational cost for studying interface and surface thermodynamics is, therefore, high. Model interfaces must be specified from macroscopic geometrical parameters, i.e., the relative rotations and surface normals of grains. Additionally, the relative translation must be optimized. For surfaces, normals is sufficient to specify the surface. Further, for a full description of the interface/surface free energy the local chemistry and local structure must be optimized. Optimizing the local chemistry involves studying the effect of adsorption and segregation and optimizing the local structure involves looking at the formation of interface and surface thin films (complexions). Since interface and surface free energies are temperature dependent the effect of temperature should also be considered.

In this thesis a variety of atomistic descriptions and computational free energy methods are used in order to describe interface and surface thermodynamics in cemented carbides. The atomistic descriptions include density functional theory, analytical bond order potential (ABOP), cluster expansions (CE) and force constant (FC) models. Further, the free energy methods include thermodynamic and temperature integration

from both molecular dynamics (MD) and Monte Carlo (MC) simulations, quasi-harmonic approximation (QHA), effective harmonic models (EHMs) from ab-initio molecular dynamics (AIMD) simulations, surface stress for liquid surface free energy and calculation of work of adhesion from separation and joining simulations.

The wettability in cemented carbides is an important factor in the sintering of these composite materials. In Paper I wetting of WC surfaces and WC/WC grain boundaries in WC–Co and WC–Ni cemented carbides are investigated using DFT with a focus on the effect from changes in the local chemistry of the interface and the effect from temperature. Paper II is a companion study to Paper I where the temperature dependence of interface and surface energies using an ABOP is investigated.

It has been proposed that WC/WC grain boundary sliding is an important deformation mechanism in cemented carbides and that it is facilitated by grain boundaries being infiltrated by binder phase at high stresses[9]. In Paper III an ABOP is, therefore, fitted using DFT data for the W-C-Co system and WC/WC grain boundary sliding is investigated for various amounts of Co binder phase infiltrated in the grain boundary and for different temperatures.

It has been experminetally established that thin cubic films form at phase boundaries between WC and Co in both undoped and doped cemented carbides [10, 11, 12]. Moreover, these thin films likely inhibit the growth of WC grains during sintering, which is important to achieve a final material with high hardness. In Paper IV the cubic and hexagonal WC phases are investigated at high temperatures using a variety of atomistic descriptions and free energy methods. It is a companion study to Paper V where the formation of thin cubic WC films (complexions) at WC/Co phase boundaries in undoped cemented carbides is studied using similar methods. In the last paper, Paper VI, the formation of thin cubic (Ti,W)C films at WC/Co phase boundaries in Ti doped cemented carbides are studied.

2

Cemented carbides

Cemented carbides are composite materials with a hard component consisting of one or more carbides, and a more ductile binder component which acts as cement between the carbide grains, hence, the name cemented carbides [5, 6]. The hard component is almost always tungsten carbide (WC), to which sometimes also cubic carbides such as titanium, tantalum or niobium carbides (TiC, TaC or NbC) are added, and the binder is usually cobalt-rich with dissolved atoms from the carbide phase(s). These composite materials are manufactured by means of powder metallurgy, where powders of tungsten carbide and binder metal are mixed and milled, then pressed and finally sintered. The sintering is done at temperatures in the interval 1350 to 1500 °C, where the binder phase is molten, which accelerates the densification and this results in a material with almost 100% of theoretical density. The resulting material consists of a continuous skeleton of hard carbide grains inside a matrix of ductile binder phase, where the former serves to give the material significant hardness and wear resistance, while the later gives increased toughness [4]. This combination of both high hardness and toughness makes cemented carbides unique among hard materials, see Fig. 1.1. The hardness and toughness of the cemented carbide can also be adjusted by varying the WC grain size and the amount of cubic carbide addition, and the binder content and composition.

When manufacturing cemented carbides it is important to control the phase constitution to avoid deteriorating phases [13]. The desired phases in the microstructure of cemented carbides are hexagonal WC and fcc binder [14]. The phase constitution is to large degree controlled by the amount carbon (carbon activity) in the material and small changes in the amount of carbon may have large effects on the phase constitution. If the amount of carbon is too high, graphite will form in material, and if the amount of carbon is too low, complex carbides called eta phases will form. Both of these are considered to be deteriorating for the material properties [13]. There is, thus, a window of carbon contents within which no graphite, nor eta phase, is formed in the material.

This window is bound by the graphite and eta limits, which mark the carbon contents where the respective phases are formed. In this theses we refer to a material with a high carbon content as C-rich and a material with a low carbon content as W-rich.

Originally, in the 1920s, cemented carbides were developed in order to replace diamond in drawing dies for tungsten filament production [6]. However, it was soon realized that the main application for this material was metal cutting and rock drilling. The new cemented carbides radically outperformed the usual alloyed steels and stellites, which reduced the cost drastically, leading to a big increase in productivity. Today, cemented carbide is the most widely used material for various metal machining operations such as cutting, turning, milling, drilling, threading, grooving, etc. [5].

Ever since Karl Schröter proposed to bind tungsten carbide with cobalt in 1923, cobalt has been the traditional choice as binder metal [15]. A combination of its excellent mechanical properties and wetting of WC makes it a very good binder metal. Furthermore, it is less challenging to get a material free from graphite and η phase compared to other binders such as nickel and iron [14]. Although the occurrence of cobalt in the earth's crust is only slightly less than that of zinc or lead, the main ore deposits are located in areas less accessible to the industrial world, mainly in Central Africa [15, 16]. The price and supply of cobalt is therefore subject to large fluctuations. In the recent times cobalt has also been found to be toxic and carcinogenic, especially in the form of (WC–Co) hardmetal dust [8]. Consequently, there is a large drive for replacing cobalt completely or partially as binder. Initially, though, research was dedicated to replacing cobalt in order to avoid the early patent restrictions [16].

Historically nickel has received the most attention as an alternative binder to cobalt due to its similar properties [14]. A complete substitution of cobalt for nickel results in material with inferior hardness and strength due to the more ductile binder phase [15]. The higher stacking fault energy of Ni also makes the work hardening moderate compared to Co [8]. However, the fracture toughness and the wear resistance are improved and the corrosion and oxidation resistance is superior to cobalt bound cemented carbides [15, 14, 8]. Consequently, nickel is almost exclusively used as binder material in die and wear parts. It is important to note that the toxicity of Ni is at the same level as Co which could limit further development of pure Ni bound cemented carbides [8].

Cemented carbides with certain Fe-Ni-Co binder compositions have been shown to be of interest for the hard metal industry, especially in applications where improved fatigue strength and toughness are required [8]. However, it is very demanding to produce defect free iron bonded materials due to the narrow carbon window. Further, Fe bound cemented carbides have a tendency to form martensite and react with Fe-based workpieces during machining operations. The usage of iron based binders in cemented carbides is, however, predicted to grow due to its superiority in certain applications and its more environmentally friendly nature compared to Ni and Co [5]. A further driving forces is the superior availability of iron compared to nickel and cobalt.

Other examples of alternative binder compositions are nickel aluminides (Ni_3Al and

NiAl) and iron aluminides (Fe_3Al and FeAl). These binders are suitable in high-temperature applications and extremely corrosive environments [17, 18, 19, 20]. High entropy alloys are also considered as alternative binder phases [21, 22, 23].

As cobalt is and has been the most common binder in cemented carbides for along time, most of the research on cemented carbides have been directed towards improving and understanding WC–Co based cemented carbides. There is thus much more knowledge of the properties and production of cemented carbides with cobalt as binder compared to other binder compositions. It is the author's opinion that this acts as a lock-in mechanism that prevents the industry from moving away from cobalt as a binder, even though alternatives with comparable or sometimes superior properties exist. Research on alternative binders is, therefore, of great importance.

Similar to cobalt, tungsten is also found in areas less available to most of the industrial world, with the main deposits being located in China and Eastern Europe [16]. Consequently, there has also been development towards replacing the WC hard phase by TiC, which culminated in TiCN cermets.

2.1 Manufacturing

Cemented carbides are produced by means of powder metallurgy, where metal and carbide powders are mixed and heated to form a dense material. There are many steps in the process from raw material to finished product and all of these steps affect, to a varying degree, the microstructure of the final material [24, 25].

2.1.1 Powders

WC powder is most commonly produced by carburization of tungsten metal powder prepared by hydrogen reduction of WO_3 [26]. It is also possible to carburize and reduce WO_3 simultaneously. The primary sources of the tungsten are the minerals Scheelite ($CaWO_4$) and Wolframite (Fe,Mn)WO_4. The typical grain size of conventionally produced WC powder ranges from 0.15 to 12 μm [27]. A scanning electron microscope (SEM) micrograph of a WC powder with a grain size in the sub-micron range is seen in Fig. 2.1.

Cobalt, the most common binder, is mainly produced as the by-products of more common copper and nickel metals or from re-cycling of cemented carbide scrap due to a scarcity of cobalt ores [29]. Pure cobalt compounds are produced by hydrometallurgical processing of cobalt from the ores and scrap. These compounds are then reduced to form cobalt powders.

Most powders of carbide and binder phases are available as commercial products. Consequently, to choose the powders that will be used is the first stage in the manufacturing of cemented carbides [28]. Selection of the correct powder is critical in order

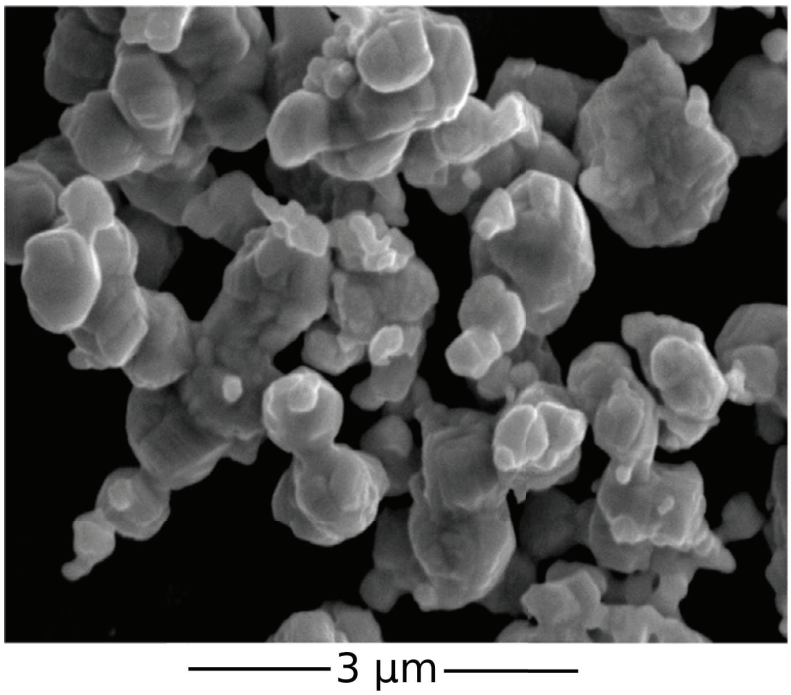

Figure 2.1: WC powder with grain size in the submicron range [28].

to achieve the required quality in the final sintered product, meet the cost targets and accommodate subsequent process requirements. The quality of the powders is determined by the composition, particle size, morphology, surface chemistry, etc.

2.1.2 Milling, drying, pressing

As the first step in consolidating the cemented carbide, the powders are mixed together and thereafter milled [28, 13, 26]. Often, small amounts of other carbides such as TiC and CrC are added to control to the grain size and grain shape to get desired properties. The purpose of the milling is to get a more uniform mixing of the powders, reduce particle size to a desired value, and to reduce agglomeration of WC particles. It is critical to get the mixing uniform since it determines reliability and repeatability of properties and performance of the final products. For example, an insufficient mixing of binder and carbide may lead to defects such as porosity and binder metal pools. The most common milling methods are rolling ball milling and attritor milling, and each of these methods has its own particular milling characteristic. For example, rolling ball milling generally gives a more narrow particle size distribution than attritor milling, but the milling time is considerably longer. Rolling ball milling is effective in reducing the particle sizes down to roughly 2 μm, while attritor milling can produce finer particle sizes. The energy involved in milling is high, and it is therefore necessary to carry out

the milling in a protective liquid to minimize temperature rise and prevent oxidation [26]. Often, an organic liquid such as acetone or alcohol is used. In order to improve the strength of the material after the forthcoming pressing, an organic binder such as paraffin wax or polyethylene glycol is also added in the milling stage [28]. Additionally, to facilitate the mixing and particle deagglomeration, and to reduce particle size by crushing and attrition, a milling media is also added to the mill. This milling media often consists of bodies of WC–Co [30].

When the slurry of carbide and binder grains obtained after milling is dried the resulting powder is very fine. The powder therefore have a low flowability and a low apparent density which is not desirable for pressing [26]. To avoid this, a process called *granulation* is adopted, where the objective is to create loose agglomerates of the fine powder. The old conventional method of granulation is to first boil off the solvent in a vacuum, then press the powder into billets. These billets are thereafter disintegrated and finally particles of the desired size are sieved in filterers. In the modern and more direct method, spray drying, the slurry is dried and granulated by spraying it into a stream of preheated inert gas. This method of granulation generates granules of uniform size and nearly spherical shape which is favourable for the pressing stage.

After the granulation the powder is ready to be pressed into a compact called a *green body*. Common methods for shaping the green body are uniaxial die pressing, cold isostatic pressing, extrusion and powder injection molding [13]. Die pressing is, however, the most widely used and economical method of shaping in the cemented carbide industry. Usually, the pressures used in pressing are in the range of 30-200 MPa. The green body can be shaped close to the desired final shape as shape is approximately maintained during sintering. However, one has to compensate for the substantial linear shrinkage of roughly 20% [27, 30]. A picture of green body and sintered material which demonstrates this shrinkage can be seen in Fig. 2.2.

2.1.3 Sintering

The purpose of the sintering stage is to strengthen the material through densification, thus eliminating pores, and by creating strong intergrain cohesion. To accomplish this, the green body is heated in a furnace where the temperature and atmosphere is well-controlled. The temperature progression of a typical sintering cycle of a WC–Co cemented carbide can be seen in Fig. 2.3. First, the temperature is slowly raised to approximately 300 °C, during which, the organic binder is removed ("de-waxing") [30]. A hydrogen atmosphere is often used in this stage. Thereafter, the furnace is evacuated and the atmosphere is kept as vacuum if no other atmosphere is needed. This is followed by a raise in temperature to approximately 1200 °C. Since the pores are still opened at this stage, oxygen reduction can take place. The temperature is kept at 1200 °C for some time and solid-state sintering occurs, which actually is responsible for more than half of the total densification during the entire sintering [26]. At this point

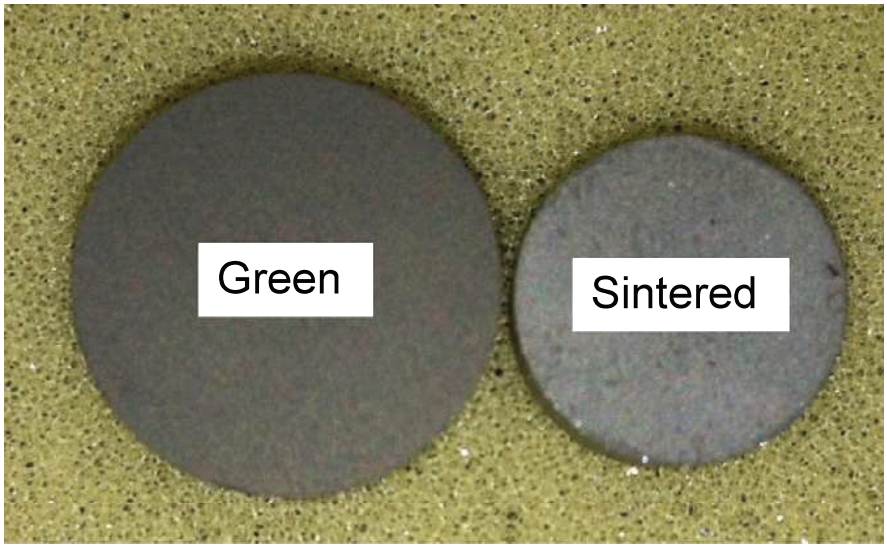

Figure 2.2: Example of shrinkage as a result of sintering [28]. Green body (left) and the corresponding sintered material (right).

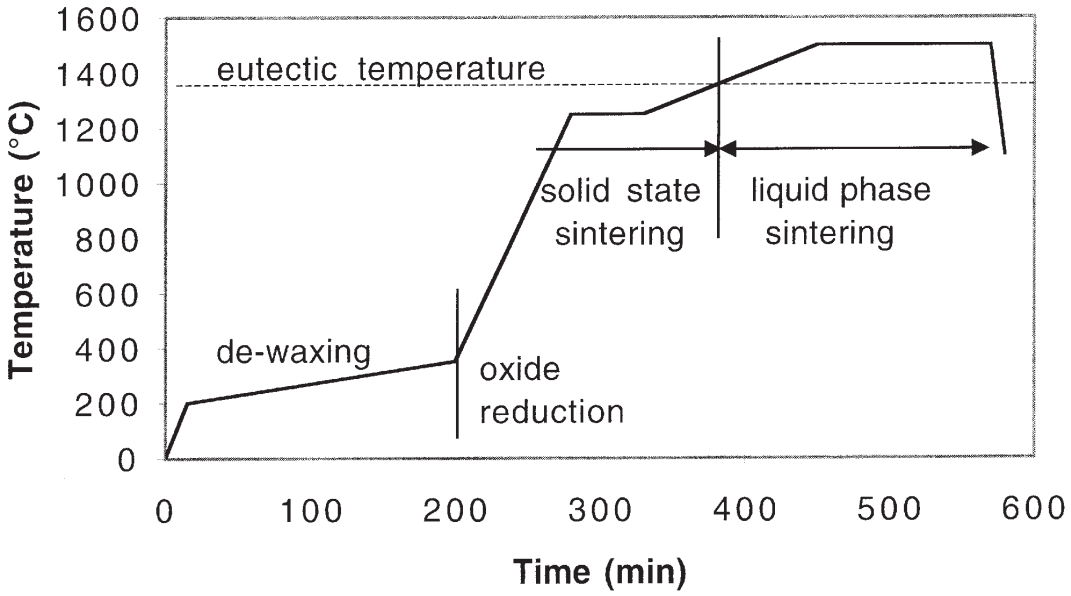

Figure 2.3: Typical sintering cycle for WC–Co [30].

the W and C also start dissolving in the binder [30]. Now, the temperature is raised to and kept at about 1400-1500 °C, which is above the eutectic temperature. Consequently, the binder melts which onsets the liquid-phase sintering. W and C dissolves further in the liquid binder and the remaining porosity is almost completely eliminated. During the liquid-phase sintering, a lot of the WC grain growth takes place through solution-reprecipitation. Finally, the material is cooled down. This vacuum sintering method works well for materials where wetting is excellent, however, if wetting is poorer, hot isostatic pressure (HIP) sintering may be used to achieve full densification.

2.1.4 Finishing and coating

Due to the shrinkage during sintering many materials often need finishing after sintering. Since the cemented carbides are very hard, diamond abrasives are often used for the machining. A majority of cutting tools made from WC–Co are coated by a thin film of ceramic material, using either physical vapor deposition (PVD) or chemical vapor deposition (CVD) [13, 31, 32, 33, 34, 35]. The coated materials have a higher wear resistance and potentially better chemical stability which prolongs the lifetime of tools considerably.

2.2 Densification process

The driving force for sintering, both in solid and liquid state, is the reduction of interface energy in the system [36]. The reduction of interface energy can be accomplished by either reducing the total interface area or equilibration of the interfaces to more favourable configurations. This induces a mass transport which leads to densification and grain growth.

Initially the mix of powders contain lots of porosities, which are reduced during solid-state sintering when the facets of WC grains are optimized and phase boundaries between WC and binder are formed as the binder wets the carbide [36]. It has been suggested that Co spreading on WC is preceded by a fast moving precursor film of submonolayer thickness, on top of which the Co front may flow easily [37]. A majority of the shrinkage occurs in during the solid state sintering [38].

Upon the subsequent melting of the binder phase WC grains become more mobile and capillary forces pull the solid grains together which further densifies the material [36]. The liquid binder also spreads and wets the carbide more effectively than in the solid state. Coarsening of WC grains occurs through solution-reprecipitation according to Ostwald ripening, where W and C atoms diffuse through the binder from smaller to larger grains to reduce total interface area. WC grain growth is also believed to take place by means of grain boundary migration [39]. The growth of the WC grains will eventually lead to the formation of a rigid three-dimensional solid skeletal structure

with liquid dispersed in the spaces between solid grains [36]. This is supported by the results of Paper I where we predict that most grain boundaries will be stable, i.e., they will resist infiltration from the binder at liquid phase sinter temperatures. After this stage the final densification occurs slowly and it is often common to apply an external pressure which aids in closing the remaining pores. During the final stage the WC grains continue to grow.

Experimental studies on the shrinkage in WC–Co cemented carbides during sintering shows that the shrinkage is faster in W-rich materials compared to C-rich materials in the early stages of sintering [40, 38]. This is illustrated in Fig. 2.4, where the shrinkage and shrinkage rate is plotted for one W-rich and one C-rich cemented carbide. The fast shrinkage rate for C-rich materials might be explained by the better wettability in C-rich materials compared with W-rich materials which have been found both in experiments by Konyashin *et al.*[41] and from computations in Paper I. Further, also in the solid state a part of the densification is achieved by Ostwald ripening, facilitated by diffusion of W and C atoms in the binder phase. The availability of W and C atoms is, therefore, a rate limiting factor. Moreover, as the diffusion of W atoms is considerably slower compared with C diffusion the availability of W atoms is likely more limiting compared with the availability of C atoms. Since the solubility of W in the binder phase decreases with an increasing C content, so does the availability of W for reprecipitation giving a lower shrinkage rate. To maintain the shrinkage rate, the lower solubility has to be compensated by a higher diffusion rate increase which accomplished by increasing the temperature. The higher shrinkage rate for C-rich materials at the later parts of the sintering could be the result of it having more pores left to shrink compared to the W-rich material.

2.3 Controlling the phase constitution

It is crucial to control the phase constitution during the sintering cycle since the formation of unwanted phases likely will deteriorate the mechanical properties of the material [13]. In Fig. 2.5, the cross sections of the W-C-Co phase diagram at 6 and 10 wt.% of Co is shown. During sintering of WC–Co it is desired to stay within the fcc Co + WC and liquid Co + WC two-phase regions [14]. It is evident from the phase diagrams that the window of carbon contents for the fcc Co + WC two-phase region is narrow especially for the cemented carbide with low Co content. If the amount of carbon is too low, complex carbides of W–Co–C, called eta phases (M_6C and $M_{12}C$), will form during sintering. Here, M_i means $W_{i-x}Co_x$, i.e., a mixture of W and Co. These phases are characterized as brittle and will thus deteriorate the material [13]. When the carbon content is too high, uncombined carbon will form a free graphite phase which is undesirable since it undermines the mechanical strength of the material. However, the graphite phase is not considered to be as detrimental as the eta phase. This demon-

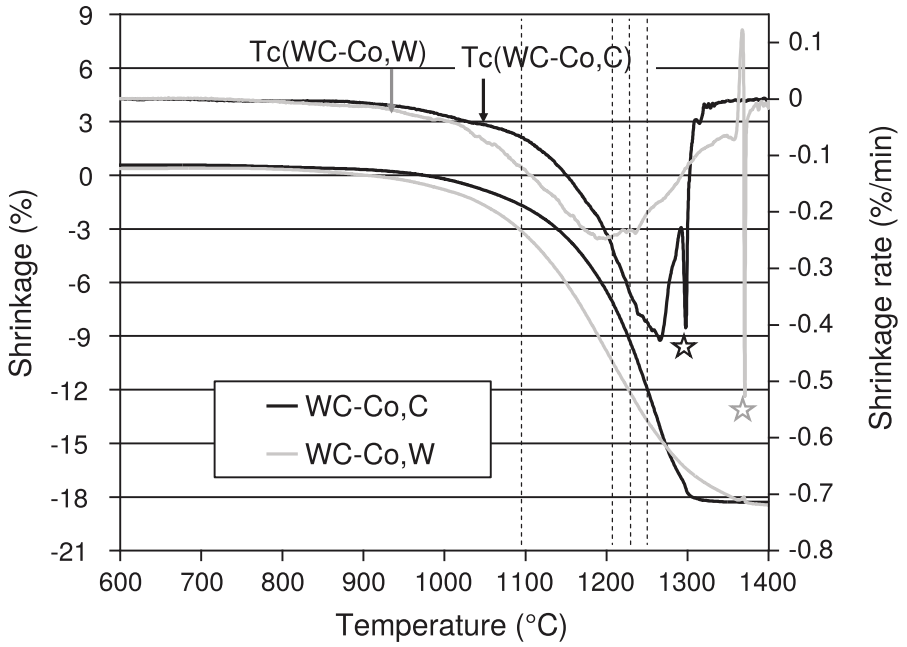

Figure 2.4: Shrinkage and shrinkage rate in W-rich (WC–Co,W) and C-rich (WC–Co,C) WC–Co cemented carbides during sintering [38]. The shrinkage is represented by the two lower curves, while the shrinkage rate is represented by the two upper curves. The stars indicate the temperatures where the binder melts for the two materials. Tc marks the Curie temperature for the two materials.

strates that controlling the carbon content is a critical parameter when manufacturing cemented carbides. From Fig. 2.5 we see that the composition with equal amounts of W and C lies within the two-phase region for both 6 and 10 wt.% of Co.

The cross sections of the W-C-Fe, W-C-Co, and W-C-Ni phase diagrams at 10 wt.% of binder is shown in Fig. 2.6. In the three cemented carbides the fcc binder + WC and liquid binder + WC two-phase regions are desired during sintering [14].
The phase diagrams of the three different systems are similar when comes to the phases that are present. We see that the carbon window of W-C-Ni is comparable to that of W-C-Co, however for W-C-Fe the carbon window is much narrower which complicates the sintering process. For both W-C-Fe and W-C-Ni the composition with equal amounts of W and C lies outside the desired two-phase region. In W-C-Fe with equal amounts of W and C eta phase will form upon cooling and carbon, therefore, has to be added to avoid formation of eta phase [14, 44]. However, in W-C-Ni with equal amounts of W and C graphite will form upon cooling which means a lower carbon content is desired [14]. Further, the higher sintering temperatures for W-C-Ni compared to Co leads to carbon pickup which may cause graphite formation [15, 44]. Additionally, the vapour pressure of is Ni high (10 times that of Co) which may lead to loss of Ni during sintering

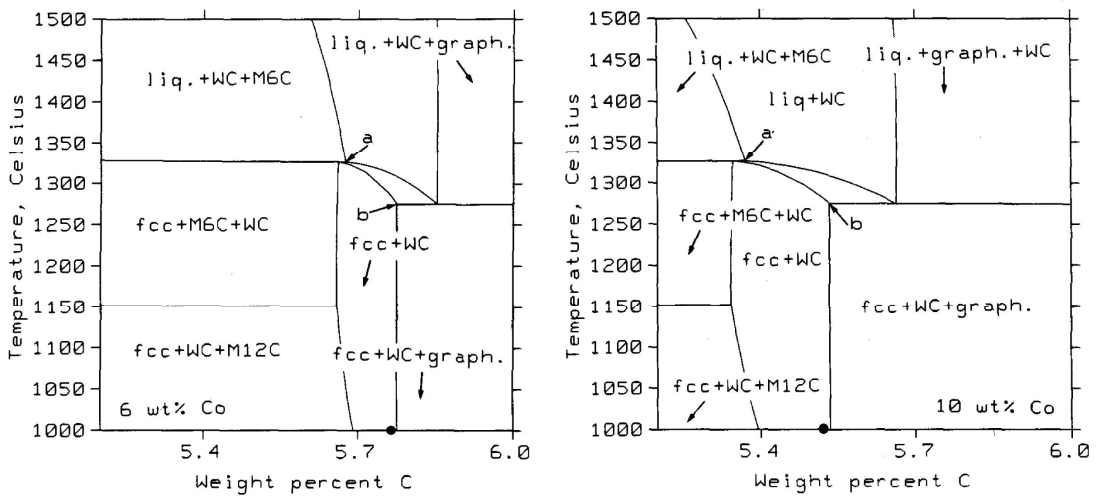

(a) 6 wt.%. (b) 10 wt.%.

Figure 2.5: Cross sections of the phase diagrams for the W–C–Co system at 6 and 10 wt.% of binder [42]. The dots on the composition axis indicates the compositions with equal amounts of W and C. The low and high carbon contents that defines the carbon window are marked with the letters a and b, respectively.

if the working pressure is not controlled properly [15].

In the DFT calculations in the appended papers we vary the chemical potential of carbon in intervals that correspond to carbon contents between the graphite and eta limits.

2.4 Tailoring the mechanical properties

There are several ways in which you can tailor the mechanical properties of the cemented carbide. Let us consider the most common cemented carbide, WC–Co. The most obvious parameter to change in a WC–Co cemented carbide is the amount of W, C, and Co in the material. Intuitively, an increased Co content will reduce the hardness and wear resistance but increase the toughness of the material. As described in Sec. 2.3 too much or too little W or C will result in η phase or graphite formation which deteriorate the material properties. However, the properties of the cemented carbide within the hexagonal WC + fcc Co carbon window, see Figs. 2.5 and 2.6, also depend on the ratio between C and W. A higher W content gives a harder and more wear resistant but also more brittle material compared with a material with lower C content [45]. The main explanation for this is that the solid solution strengthening of the binder phase is stronger from dissolution of W compared with dissolution of C. Also contributing to the dependency of the material properties on the C and W content is the increased

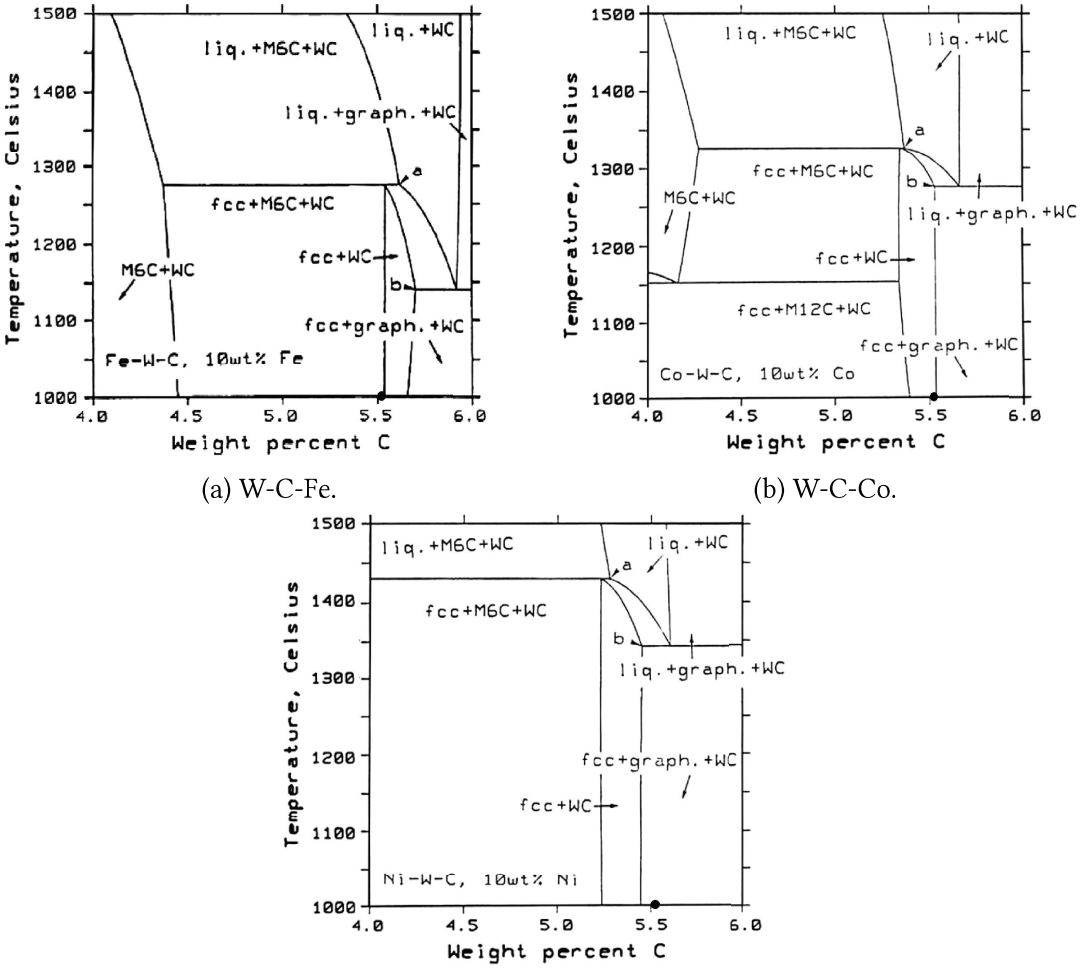

(a) W-C-Fe.

(b) W-C-Co.

(c) W-C-Ni.

Figure 2.6: Cross sections of the phase diagrams for the three different systems, W–C–Fe, W–C–Co, and W–C–Ni, at 10 wt.% of binder [43]. The dots on the composition axis indicates the compositions with equal amounts of W and C. The low and high carbon contents that defines the carbon windows for each material are marked with the letters a and b, respectively.

grain growth of WC grains during sintering with increasing C content[46, 47], where larger WC grains gives a tougher but also softer and less wear resistant material[5]. The inverse relationship between the strength and average grain size of a polycrystalline material is commonly referred to as the Hall-Petch relationship[48, 49].

There are other ways of reducing the size of WC grains to get a harder and less tough material. For example, by adding small amounts of grain growth inhibitors such as VC, TiC or Cr_3C_2 or, alternatively, by using a finer WC powder. Additionally, by introducing large enough amounts of cubic transition metal carbides such as TiC, TaC or NbC these will precipitate and form a solid solution with WC in the binder [5]. This makes the cubic skeleton harder which gives an enhanced creep and wear resistance, however, the material also becomes more brittle. CrC can also be added to the material, which then segregates to WC/WC grain boundaries and WC/Co phase boundaries where it hinders grain boundary migration and solution/re-precipitation of W and C atoms, respectively [50, 51, 52]. During compression WC grains grows perpendicular to the load axis[52] and grain boundary migration and solution/re-precipitation are likely important process to get grain growth. With the segregated Cr these processes are limited and the time needed to deform the material drastically increases which prolongs the lifetime of the tool. This addition is mainly used in rock drilling tools.

All methods stated above only change the properties of the pure and homogeneous material and they are, therefore, limited to the trade off between hardness and toughness. There are, however, other ways of changing the mechanical behaviour of a material that go beyond the overall composition and WC grain size. As already mentioned in Sec. 2.1.4 the cemented carbide may be coated by a thin film of ceramic material which increases the hardness and wear resistance without compromising on the toughness of the material. This is also illustrated in Fig. 1.1. In order to support the hard coating and preventing cracks from propagating down into the substrate several volume percent of Ti, Ta and/or Nb carbonitrides are added to the material before sintering[53]. In the cemented carbide, precipitates of these carbonitrides or other additions are referred to as gamma phase. During sintering N leaves the material near the surface and Ti, Ta and/or Nb diffuses towards regions with higher N content. A gradient of gamma phase concentration is, therefore, formed with a thin surface layer with low concentration compared to the rest of the material. This surface layer is, consequently, tougher than the gamma phase rich bulk region, and it will resist crack propagation. This type of sintering, where gradients of the phases are formed in the material under controlled conditions, is called gradient sintering.

It is also possible to get a gradient of the Co content with less Co near the surface and more in the bulk using other gradient sintering techniques [5, 54, 55, 56]. In this way the surface layers are harder and more wear resistant while the bulk material is more tough. Overall, you end up with a material that can combine a higher hardness and toughness.

3

Microstructure of cemented carbides

”We’ve gotta look a little, look a little, look a little closer.
To find out what we want to know ”

– Daniel Tiger’s Neighbourhood [57]

The microstructure of cemented carbides consists of facetted WC grains embedded in a matrix of binder phase [58, 59]. This is illustrated in Fig. 3.1, where the typical microstructure of a WC–Co cemented carbide is shown. The binder phase does not completely surround the WC grains, instead, the WC grains form contacts with other WC grains and thus build up a continuous skeleton. This microstructure ensures that the high hardness of WC and the high toughness of the binder are combined which makes this a unique material of great importance.

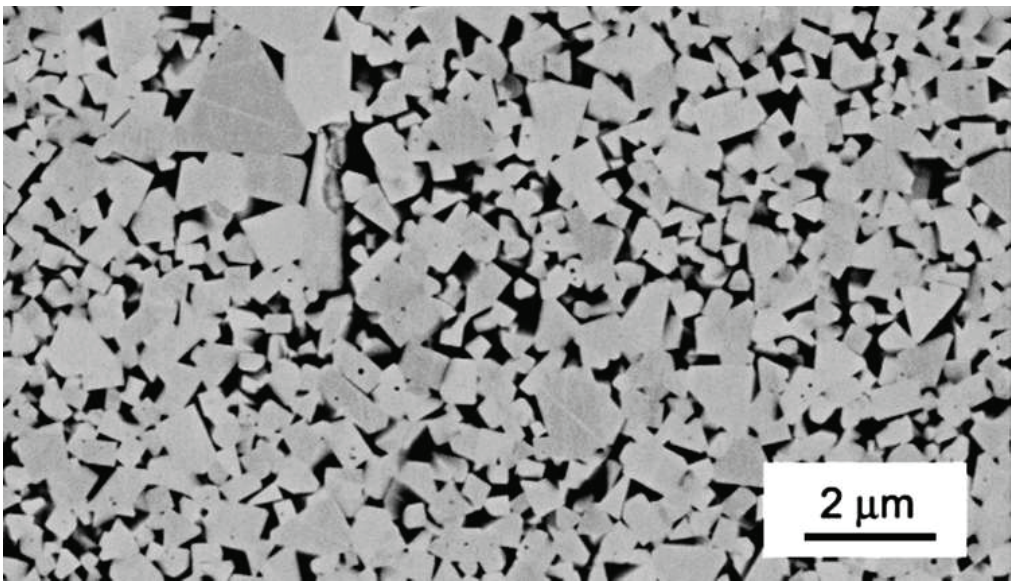

Figure 3.1: Scanning electron microscopy (SEM) micrograph of the typical microstructure of a WC–Co cemented carbide with 12 at.% Co [58]. Brigth grey indicates WC and dark grey indicates Co.

3.1 Hard phase - Tungsten carbide

In the W-C system there are three individual carbides present: W_2C, hexagonal WC, and cubic WC [26, 60]. The experimental W-C phase diagram contructed by Kurlov and Gusev [60] can be seen in Fig. 3.2. The tungsten semicarbides, W_2C, comes in three different version, where two are hexagonal and one is orthorombic. These tungsten semicarbides only exists in thermodynamic equilibrium above 1523 K. Cubic tungsten carbide, γ-WC_{1-x}, has a rocksalt (B1) structure and is thermodynamically stable in the 2789-3058 K temperature range. Further, γ-WC_{1-x} is stable in the composition range from $WC_{0.6}$ to stoichiometric WC which means that there can be a high carbon vacancy concentration. This is similar to other cubic transition metal carbides, such as VC, NbC and TiC [61, 62, 63].

The major carbide in the W-C system, and the one which is mostly relevant in cemented carbides, is hexagonal tungsten (mono)carbide (δ-WC). δ-WC has a simple hexagonal crystal structure with a two atom basis consisting of a W atom in $(0, 0, 0)$ and a C atom in either $(2/3, 1/3, 1/2)$ or $(1/3, 2/3, 1/2)$ in terms of the hexagonal lattice

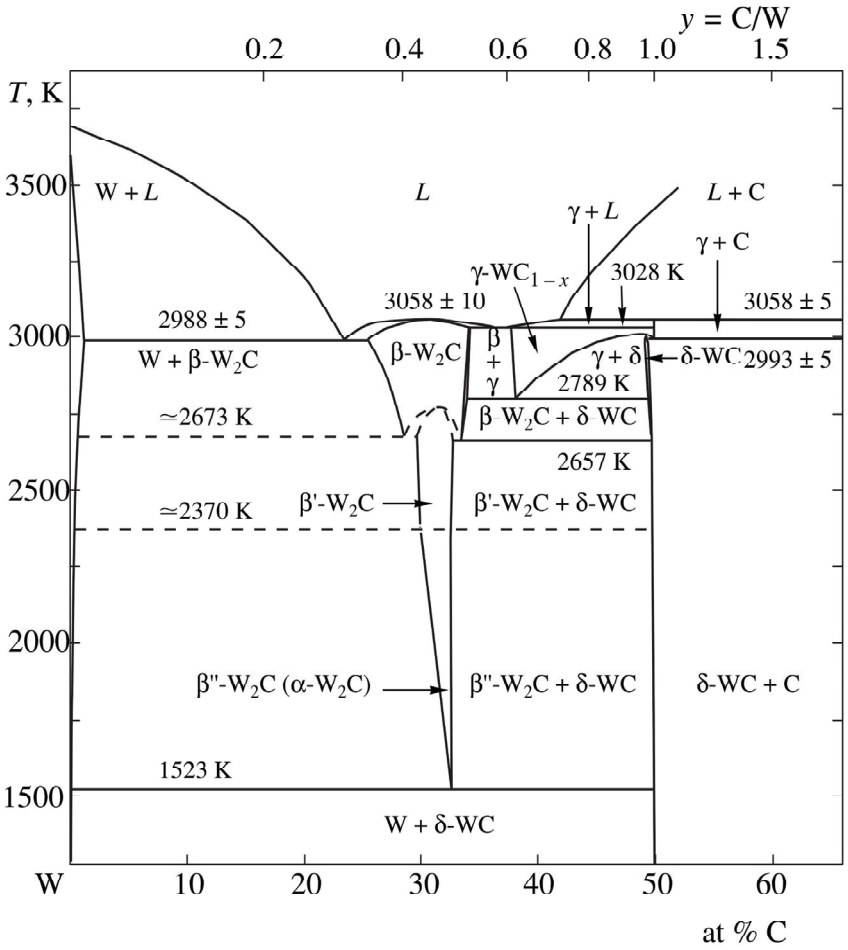

Figure 3.2: W-C phase diagram [60], where W denotes bcc W, C denotes graphite, $\beta*$-W_2C denotes various tungsten semicarbides, δ-WC deontes hexagonal WC and γ-WC denotes cubic WC.

vectors $(\mathbf{a}_1, \mathbf{a}_2, \mathbf{c})$, which are defined as

$$\mathbf{a}_1 = -\frac{a}{2}\hat{\mathbf{x}} - \frac{a\sqrt{3}}{2}\hat{\mathbf{y}} \tag{3.1}$$

$$\mathbf{a}_2 = a\hat{\mathbf{x}} \tag{3.2}$$

$$\mathbf{c} = c\hat{\mathbf{z}}. \tag{3.3}$$

In Fig. 3.3, the structure and primitive cell are shown. The lattice parameters are $a = 2.906$ Å and $c = 2.837$ Å, which implies that $c/a = 0.976$ [27]. WC exhibits no deviations from stoichiometry as it essentially contains no carbon vacancies [64, 65]. This is also evident from the phase diagram in Fig. 3.2. The melting temperature of WC is 2993 K

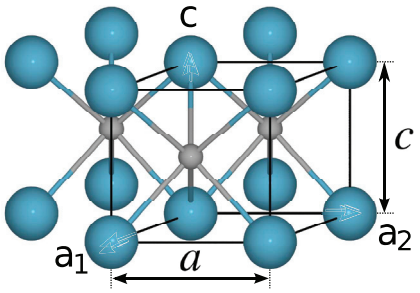

Figure 3.3: The hexagonal WC crystal structure. Large cyan coloured atoms are W and small grey atoms C. The black lines mark the primitive cell.

[29], which is well above the relevant sintering temperatures, see Sec. 2.1. In contrast to the binder phase, which dissolves appreciable amounts of WC, the WC phase dissolves very little or no amount of Co or other binder phase atoms [4]. Small amounts, below 1 at%, of additional elements such as Ta, Nb, Cr, and V can dissolve in the WC phase [66].

The chemical bonding in the WC phases is a complex mixture of covalent, ionic and metallic components[67, 68, 69, 70]. In hexagonal WC the high hardness is mainly attributed to the strong covalent W–C bond in combination with W–W bonds of metallic character[67, 68].

The equilibrium shape of WC grains in Co is a truncated prism bounded by basal (0001) planes and prismatic $(10\bar{1}0)$ planes which is illustrated in Fig. 3.4a. TEM images of real WC grains can be seen in Fig. 3.5. The truncated prism shape arises from differences in interface energies of phase boundaries with prismatic $(10\bar{1}0)$ WC planes of different types, where the two types of prismatic surface arise due to the non-centrosymmetric crystal structure of WC [71]. They are denoted S and T [72], and are illustrated in Fig. 3.4b. The type can be determined by the number of bonds between atoms in the terminating layer and the atoms in the second layer. A prismatic surface is of type S (T) if the terminating W (C) atoms are bonded to four C (W) atoms, or if the terminating C (W) atoms are bonded to two W (C) atoms. With an increasing carbon activity the grains become less truncated. An increased carbon activity also leads to a larger WC grain size after sintering which can be seen i Fig. 3.5. The typical WC grain size is around 1 μm. The growth rate and thus the final grain size of WC varies for different binder phases [46, 47]. In WC–Fe, the grain growth is inhibited and the grain size of WC is therefore smaller compared to WC–Co. In WC–Ni, on the other hand, the growth rate is larger than in WC–Co, and consequently, the final grain size is larger. This difference in WC growth rate for the three different cemented carbides is illustrated in Fig. 3.6, where microstructures of the three cemented carbides made from the same WC powder can be seen.

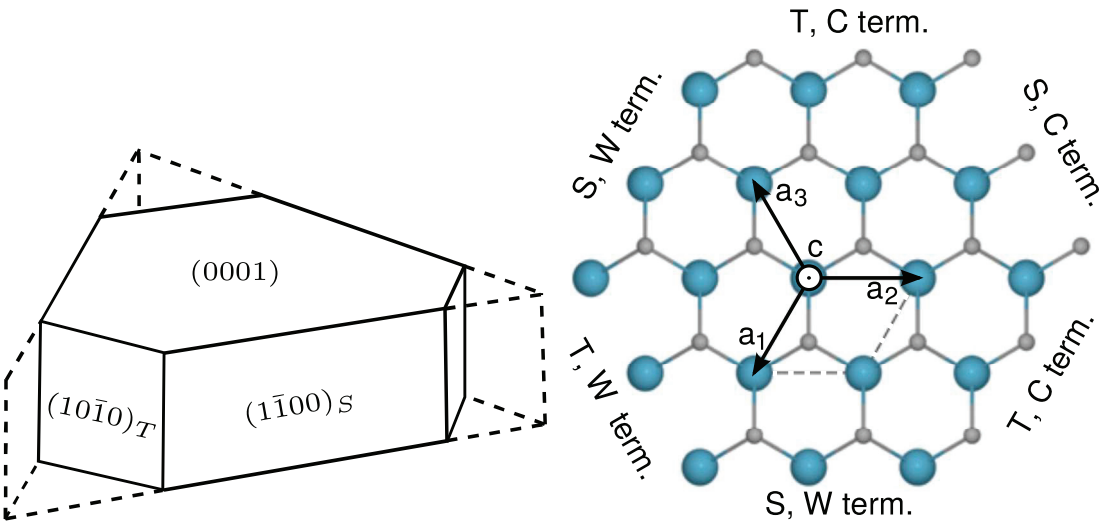

(a) Truncated prism shape of WC grains. (b) Different prismatic surfaces.

Figure 3.4: (a) Truncated prism shape of WC in cemented carbides. The prism is bounded by basal and prismatic planes. (b) Illustration of the inequivalent prismatic planes S and T seen from the [0001] direction [73]. The dashed lines show the primitive cell which is also shown in Fig.3.3. Large cyan coloured atoms are W and small grey atoms C.

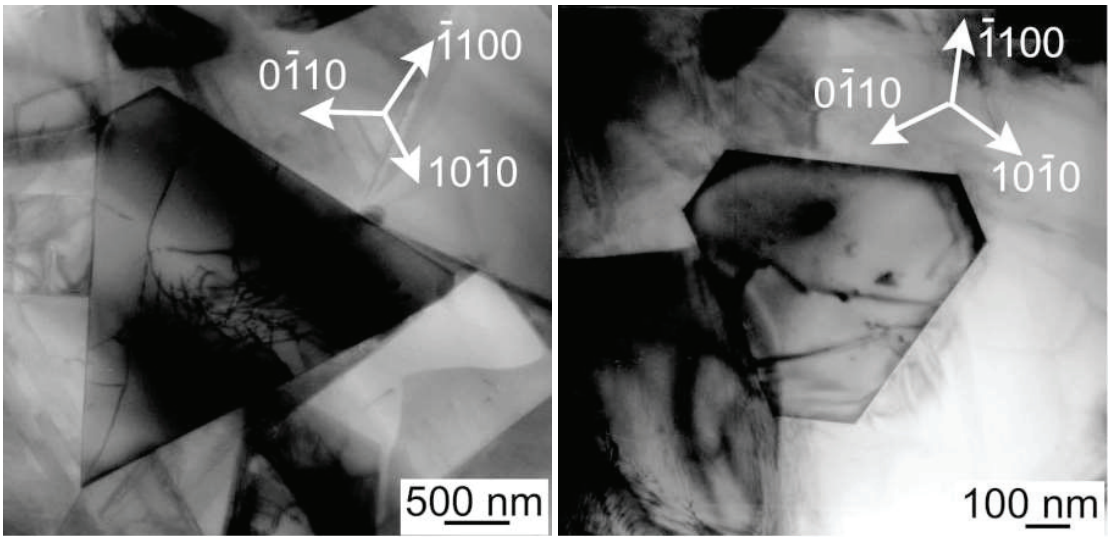

(a) C-rich (b) W-rich

Figure 3.5: TEM images of WC grains viewed along the [0001] direction showing the truncated triangular shape, where the anisotropy is larger in (a) the C-rich (graphite limit) materials than in (b) the W-rich (eta limit) materials [71].

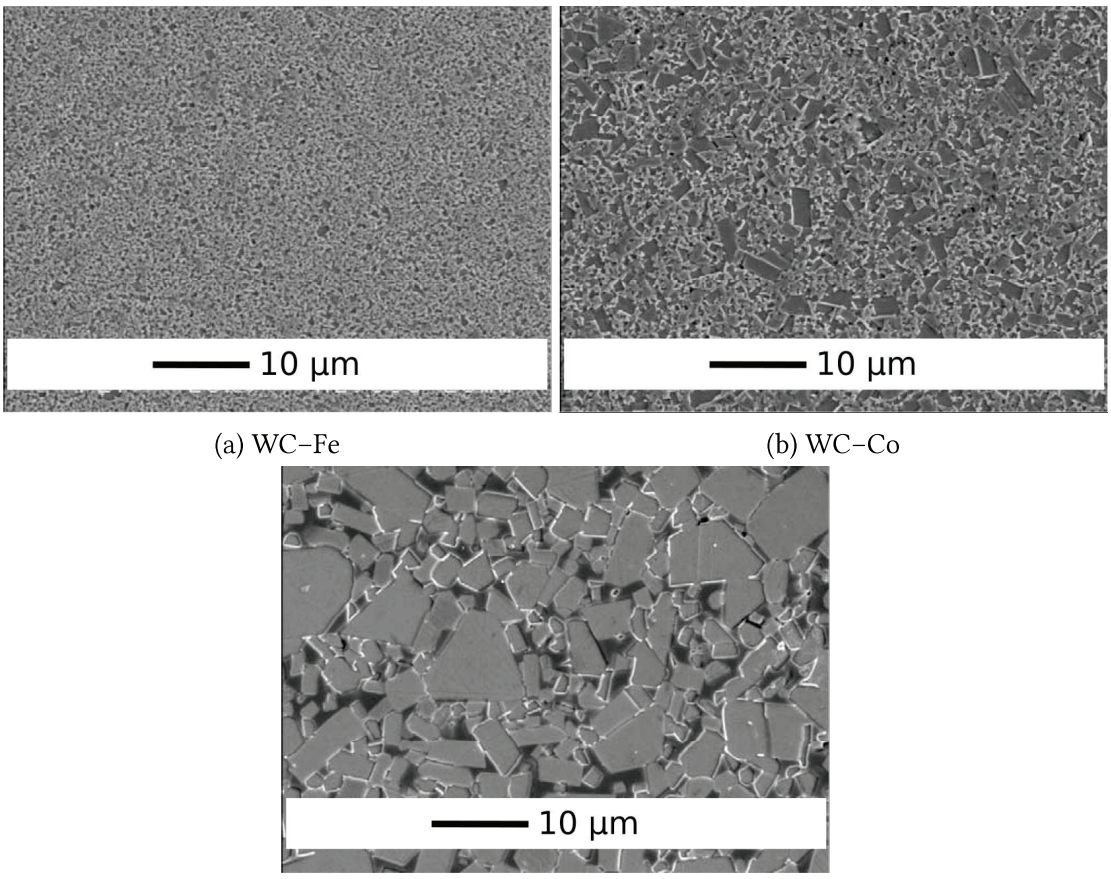

(a) WC–Fe (b) WC–Co

(c) WC–Ni

Figure 3.6: Microstructures of WC–10 wt% Co/Ni/Fe materials, based on the same submicron sized WC powder [46].

3.2 Binder phase

3.2.1 Cobalt

Pure Co appears in two different allotropic modifications: hcp and fcc [74]. The stable phase at ambient pressure for temperatures below 695 K is hcp with lattice parameters a = 2.507 Å and c = 4.070 Å [75]. This means that the structure has a near to ideal c/a ratio of 1.623. Above 695 K, the stable phase is fcc Co instead, with a lattice parameter of a = 3.545 Å. However, during cooling of Co the transformation from fcc to hcp is slow which means that both phases can coexist from 723 K down to room temperature [74]. The material is ferromagnetic up to 1394 K, its Curie temperature, where it transforms to paramagnetic [75], and the melting point of Co is 1768 K.

The Co phase dissolves a high amount of both W and C at high temperatures [58].

The solubility of W and C highly depends upon the temperature and the amount of carbon in the material. For example, at 1425 °C with a liquid Co rich binder phase, the amount of W and C in the Co binder ranges from about 9C+13W to 16C+6W (at%) when the C-content increases from the η-phase limit to the graphite limit In the solid case, at 1250 °C, the dissolution ranges between 1C + 9W and 3C + 3W (at%), instead [30]. When the material is cooled the solubility of W and C is reduced and they start to reprecipitate on WC grains in equal proportion. Due to the fast diffusion rate of C compared to W and the low carbon activity in the sintering furnace, essentially no C is found in the binder at room temperature, while the amount of W depends on the rate of cooling. For a conventionel slow cooling rate a W gradient forms with a depletion of W close WC/Co phase boundaries from the reprecipition on the WC grain [76]. Farther away from the phase boundaries, i.e., in the middle of the binder pools, the W concentration resembles that at approximately 900 °C. For fast cooling rates no W concentration gradient is formed and the concentration freezes in at around 1100 °C.

With the dissolved tungsten and carbon atoms the fcc phase is stabilized [44, 58]. Additionally, tensile residual stresses at low temperatures probably also stabilize the fcc phase. Further, since the fcc to hcp transformation is slow, the predominant phase of the Co rich binder in cemented carbides is, therefore, fcc even at low temperatures However, some hcp is usually present due to the fcc-hcp transformation [58].

The dissolved W and C also lowers the Curie temperature of the binder [38], with a more pronounced effect in W-rich conditions compared to C-rich conditions. The eutectic temperature of WC–Co is around 1550 K [43], which is well below the melting point for pure cobalt.

The grain size of the cobalt binder phase is generally much larger than WC grains with a typical size of larger than 10 μm for the binder compared to 1 μm for the carbide [58, 77]. However, the binder phase grains do not fill up the volume which they span, but they are rather interpenetrated by WC grains, which is illustrated in EBSD orientation maps of a WC–11Co (wt%) material in Fig. 3.7. Consequently, to characterize the binder phase one uses the *binder mean free path* which is a measure of the thickness of the binder pockets [58].

3.2.2 Nickel

The stable structure of pure nickel at ambient pressure is fcc with a lattice parameter of 3.524 Å [79, 80, 74, 81]. Nickel is ferromagnetic up to its Curie temperature of 631 K, where it turns paramagnetic [82]. The melting temperature of nickel is 1728 K [81], which is lower compared to cobalt. The fcc structure of Ni is also kept in the cemented carbide. Due to Co being by far the most used binder phase, less data on the microstructure of other binders are available [58]. The solubility of WC in the binder phase is less in WC–Ni compared to WC–Co. In contrast to WC–Co, where most Co grains are larger than the WC grains, Ni grains are found to be both small and large

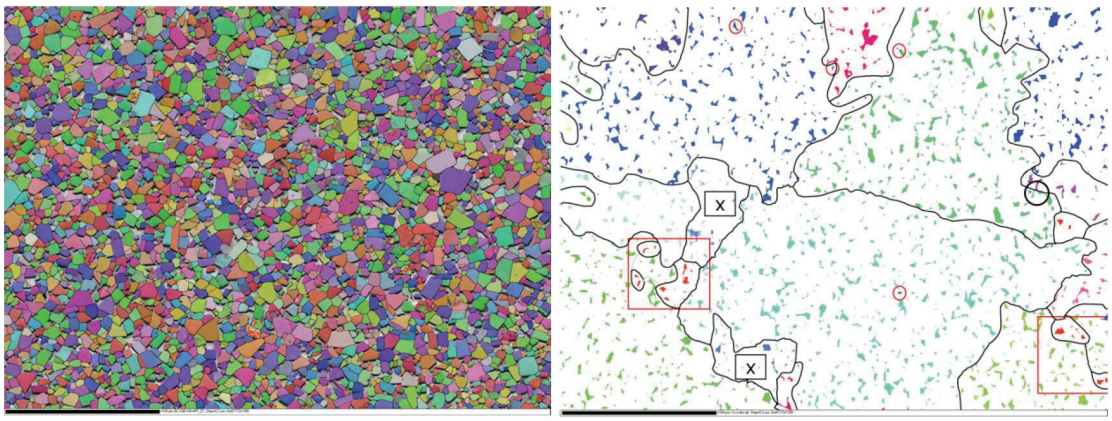

(a) WC grains (b) Co grains

Figure 3.7: EBSD orientation maps of a WC–11Co (wt%) material: (a) WC phase and (b) Co phase [78]. Black lines in (b) delineate Co regions with the same orientation. The scale marker corresponds to 100 μm.

compared to the WC grains in WC–Ni cemented carbides. The eutectic temperature of WC–Ni is around 1620 K, which is the highest among the WC–Fe, WC–Co and WC–Ni cemented carbides.

3.2.3 Iron

Iron has three stable allotropes at ambient pressure called α, γ, and δ [83, 74]. α-iron, or ferrite, has a bcc structure with lattice constant 2.866 Å and is the stable phase up to the first transition temperature of 1184 K. Between 1184 K and 1667 K iron has an fcc phase with lattice constant 3.647 Å, which is called γ-iron or austenite. At 1667 K the system transform back to bcc again with a lattice parameter of 2.932 Å. This phase is called δ-iron. The melting temperature of iron is 1811 K which is the highest of the three studied binders. The magnetic state of iron is ferromagnetic up to the Curie temperature 1043 K, above which, the material is paramagnetic [83]. Similar to cobalt the disolved W and C atoms stabilize the fcc phase of Fe which is the predominant phase in WC–Fe cemented carbides. The solubility of W and C in the binder in WC–Fe is inferior to both WC–Co and WC–Ni [4]. Although the melting temperature for Fe is higher than both Co and Ni, the eutectic temperature of WC–Fe is only around 1420 K, which is the lowest of the three corresponding cemented carbides: WC–Fe, WC–Co and WC–Ni [14].

3.3 Interfaces in cemented carbides

There is a close relationship between the microstructure and the mechanical properties of cemented carbides [58]. In particular, the phase composition, phase distribution and grain size are of special importance. The phase distribution in cemented carbides are to a large extent monitored by the relative energy of interfaces [58, 84]. In the literature, there are many studies on the morphology of interfaces in WC–Co, however, the literature is scarce on similar studies for systems with alternative binders. Hence, this section will focus on interfaces in WC–Co cemented carbides.

The distribution of WC grain facet orientations in WC/WC grain boundaries and WC/Co phase boundaries in a WC–Co cemented carbide was analyzed by Kim *et al.* [85, 86]. To create the orientation maps, they used an orientation imaging microscopy (OIM) system incorporated in a SEM, which uses the electron backscatter diffraction (EBSD) technique, in conjunction with AFM. The orientation maps for the WC/WC grain boundaries and WC/Co phase boundaries can be seen in Fig. 3.8.

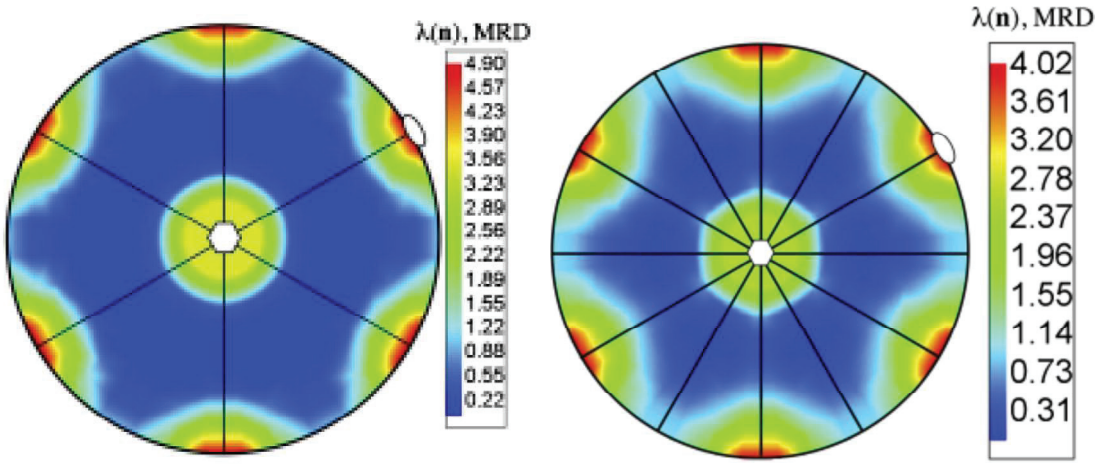

(a) WC/Co phase boundaries (b) WC/WC grain boundaries

Figure 3.8: Distribution of WC grain facet orientations in a 12 vol% of cobalt sample for phase boundaries (a) and grain boundaries (b) [85]. The basal facet orientation is marked with a prism and the prismatic facet orientation is marked with an oval.

The distributions are plotted in multiples of a random distribution (MRD) for a hexagonal crystal. This means that orientations with areas greater than expected in a random distribution have values greater than one, and orientations with areas less than expected in a random distribution have values less than one. The figures are stereograms of a 3D distribution with the basal direction in the center and the prismatic orientation on the periphery, which is marked by a prism and ovals respectively. The peaks for the basal and prismatic orientations clearly show that these are the two most common WC

planes in the WC–Co microstructure. Using a 5° tolerance angle, Kim *et al.* found that approximately 80% of the WC/Co boundaries and 60 % of the WC/WC grain boundaries can be classified as having either one basal or one prismatic WC boundary plane.

3.3.1 WC/WC grain boundaries

The WC/WC grain boundaries are important for the material strength as the WC grains build up a continuous skeleton in the cemented carbide [58]. Experiments show that a majority of crack paths in WC–Co cemented carbides consists of broken up grain boundaries [87]. Further, grain boundary sliding is thought to be the most important deformation mechanism in cemented carbides at high temperatures[88, 89, 90, 91]. This demonstrates the importance of the strength of WC/WC grain boundaries when it comes to the mechanical strength of the material. Moreover, in experiments where the Co phase was etched out from the WC–Co cemented carbide, it was found that the etched material was stronger but also more brittle compared to the cemented carbide above 1100 °C in three-point bending tests [92]. This indicates that the presence of the binder phase weakens the material at higher temperatures. It is believed that this reduction in strength is due to WC/WC grain boundaries are being infiltrated by binder phase and thus facilitating grain boundary sliding which is the dominating plastic deformation mechanism at high temperatures [93, 92, 91].

In experiments of the growth of WC grains during sintering it was observed that WC/WC grain boundaries are typically curved at lower temperatures but straighten out at higher temperatures and for longer sintering times [94]. It has also been demonstrated both experimentally and from first principles calculations that grain boundaries in WC–Co generally contain roughly 0.5 monolayer of segregated Co atoms [95, 51, 50, 96, 73]. This is demonstrated in an atom probe tomography (APT) reconstruction of a WC/WC grain boundary in a WC-TiC-Co material seen in Fig. 3.9. When additions are used in cemented carbides, such as TiC, NbC and ZrC, the metal atoms are in many cases found to segregate to WC/WC grain boundaries [50, 96]. In Paper I the segregation of binder atoms to WC/WC grain boundaries in WC–Co and WC–Ni cemented carbides are investigated.

Grain boundaries are commonly characterized by the coincidence site lattice and the misorientation of the adjoining crystals [97]. The coincidence site lattice index, Σ, is defined as follows: If the two adjoining grains are translated such that the lattices coincide, then Σ is the inverse of the fraction of coincident lattice points [98, 99]. Since the ratio $c/a = 0.976$ for WC is close to 1, it has the possibility of forming many low Σ grain boundaries in the $c/a = 1$ approximation [87]. The most studied grain boundary in literature is the $\Sigma = 2$ twist grain boundary which is formed upon a rotation of 90° around a common $[10\bar{1}0]$ axis [100], see Fig. 3.10. It has been studied experimentally in Refs [101, 102, 103, 104, 94, 105] and using first principles in Refs [106, 107]. The interface energy of the $\Sigma = 2$ twist grain boundary is low due to the preserved bulk

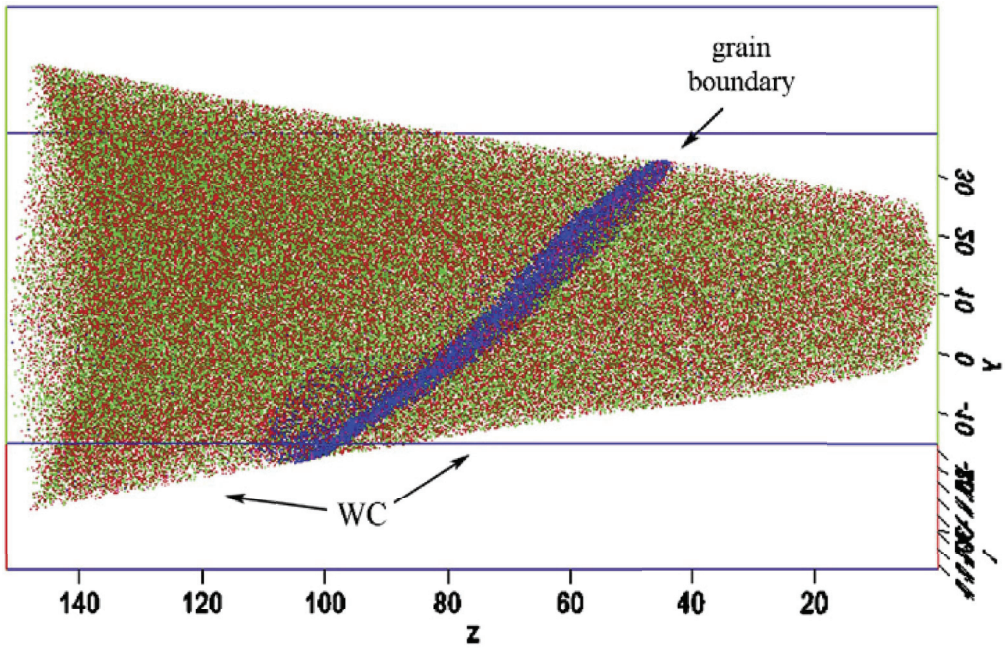

Figure 3.9: APT reconstruction of a WC/WC grain boundary in a WC–TiC–Co material [96]. Green dots = W atoms, red = C, blue = Co, pink = Ti.

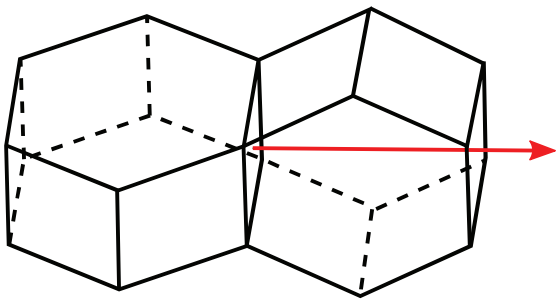

Figure 3.10: Simple sketch of the pure twist $\Sigma = 2$ grain boundary arising from a 90° rotation around a common prismatic $[10\bar{1}0]$ axis (red arrow). The interface relation is $(10\bar{1}0)||(10\bar{1}0)$, $[0001]||[1\bar{2}10]$.

like coordination across most of the interface [106, 108]. The special $\Sigma = 2$ twist grain boundary in WC–Co has been found, both from experiments and modeling, to have no segregated Co atoms [101, 106]. Further, the $\Sigma = 2$ twist grain boundaries are, due to their stability, believed to originate from the powder. This is supported by experiments where the fraction of $\Sigma = 2$ twist grain boundaries are shown to decrease during sintering when small grains dissolve and larger grow [94, 103, 104]. Also, TEM investigations on clusters in the powder and sintered material indicate that $\Sigma = 2$ twist grain boundaries arise from the powder [102].

The population of misorientations (rotations) for grain boundaries in WC–Co was measured by Kim *et al.* [85] and the results are displayed in Fig. 3.11. A clear peak at 90° is seen which was identified as the $\Sigma = 2$ twist grain boundary. There is also a clear peak at around 27°, which correspond to rotations around the [0001] axis resulting in $\Sigma = 13$ [58]. In most cases, the grain boundary is bound by two (0001) planes (twist boundary), however, grain boundaries with $(10\bar{1}0)$ and $(1\bar{2}10)$ planes (asymmetric tilt boundary) also occur. In the study they found that the 90°/$[10\bar{1}0]$ grain boundaries make up 11-14 % of the total grain boundary population, whereas the same figure for the 30°/[0001] grain boundaries was 2-3 %. Additionally, grain boundaries with a misorientation of 90° around the $[1\bar{2}10]$ axis were more common than the expected value from a random distribution. These grain boundaries are mostly bound by one basal and one prismatic WC plane and the coincidence site lattice index for this grain boundary is $\Sigma = 97$ [104]. As mentioned previously in Sec. 3.3, about 60 % of the grain boundaries in WC–Co can be classified as having either one basal or one prismatic WC boundary plane [85].

3.3.2 WC/Co phase boundaries

The interface energies of the phase boundaries in cemented carbides are important for the behaviour during sintering, especially when it comes to grain growth [58]. It is the energy of the phase boundaries that determine the morphology of the WC grains in cemented carbides [71]. Generally, WC/Co phase boundaries are planar and sharp locally [109]. In WC–Co with high carbon contents the WC grains are perfectly sharp and faceted. However, for low carbon contents, the grains have slightly rounded corners and steps are found on the WC/Co phase boundaries. To illustrate this, TEM images of WC/Co Phase boundaries in a C-rich and a W-rich WC–Co cemented carbide are shown in Fig. 3.12. Also in WC–Fe and WC–Ni cemented carbides are steps reported in the WC/binder phase boundaries in materials with low carbon content but not in materials with high carbon content[47].

During the solidification of the cobalt binder phase in WC–Co after liquid-phase sintering the Co grains are allowed to grow without any preference to orientations of the surrounding WC grains [10]. There is thus no orientation structure of general WC/Co phase boundaries similar to the one observed for WC/WC grain boundaries. However, as mentioned in Sec. 3.3, about 80 % of the phase boundaries in WC–Co can be classified

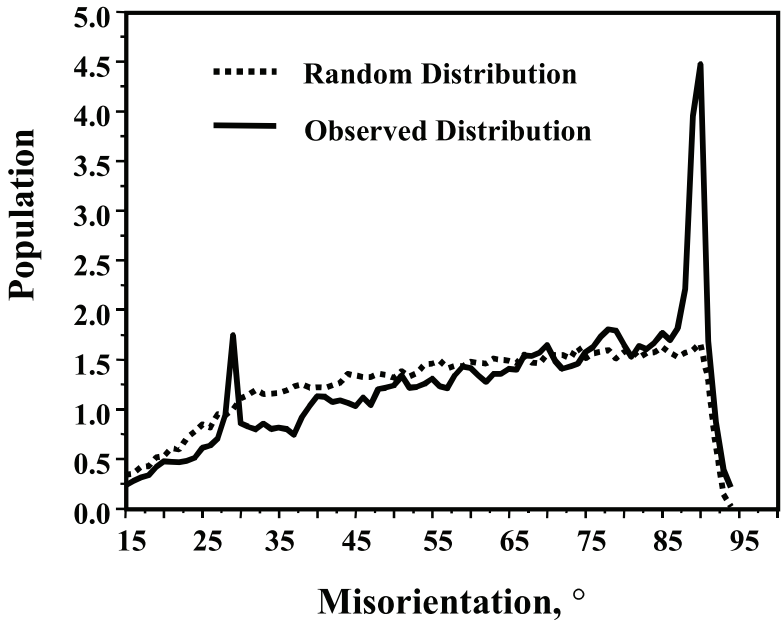

Figure 3.11: Grain boundary population of WC crystals and random objects as a function of misorientation angle [86].

as having either one basal or one prismatic WC boundary plane [85]. Further, general WC/Co phase boundaries in undoped WC–Co cemented carbides have been found to have a thin, only a few atomic planes, WC_{1-x} cubic layer at the interface [10, 11, 12]. When the material is doped with grain growth inhibitors such as VC, TiC, Cr_3C_2, TaC or NbC, these are found to segregate to WC/Co phase boundaries and form thin cubic $(M,W)C_{1-x}$ films, where M stands for either of the metal elements of the dopants [12, 110, 111, 112]. A HRTEM image of a $(Ti,W)C_{1-x}$ film in a TiC doped cemented carbide can be seen in Fig. 3.13. In the case of VC doped WC–Co cemented carbides, the formation $(V,W)C_{1-x}$ cubic layers is also supported by modeling [113, 114]. The grain growth inhibition effect of these additives have mainly been investigated empirically and the exact mechanisms behind the grain growth inhibition is still unknown. One of the proposed mechanisms is that cubic films in WC/Co interfaces hinder the WC grain growth by forming a diffusion barrier for dissolving and/or reprecipitating W atoms [115]. Understanding how and why these thin films form is, therefore, important for understanding grain growth inhibition. In Papers V and VI we study the formation of thin cubic films in WC/Co phase boundaries and derive interfacial phase diagrams for undoped and TiC doped WC–Co cemented carbides.

Experimental studies on cobalt inclusions in WC grains reported phase boundaries bounded by WC(0001) planes and Co(111) planes [116, 117]. Similarly, in small Co

pools, phase boundaries bounded by WC(0001) and Co(111) or Co(001) where reported [10]. In solid-state sintered cemented carbides these special orientations are frequently found [40].

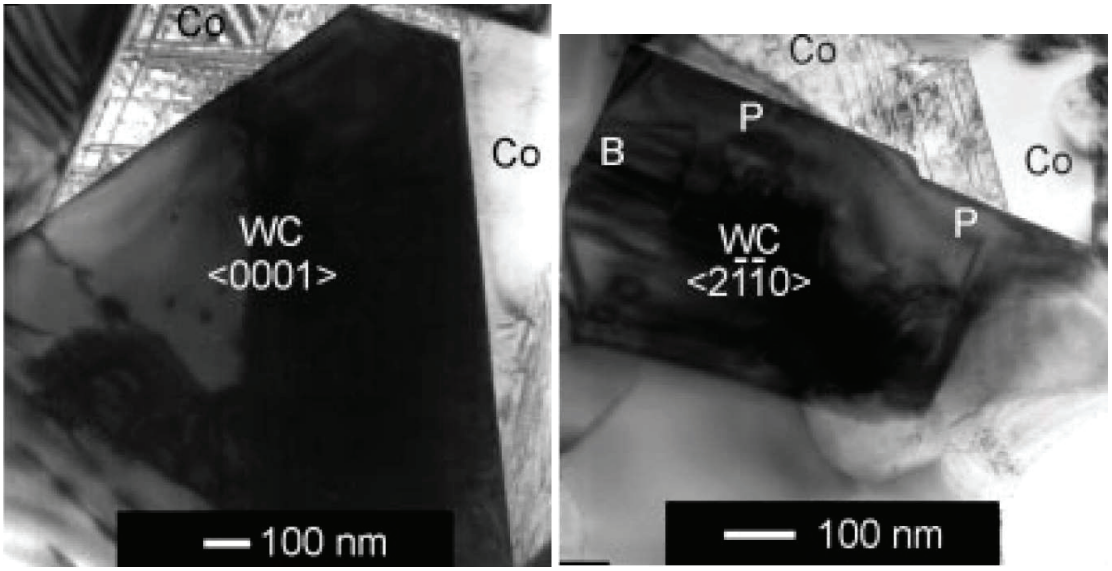

(a) C-rich (b) W-rich

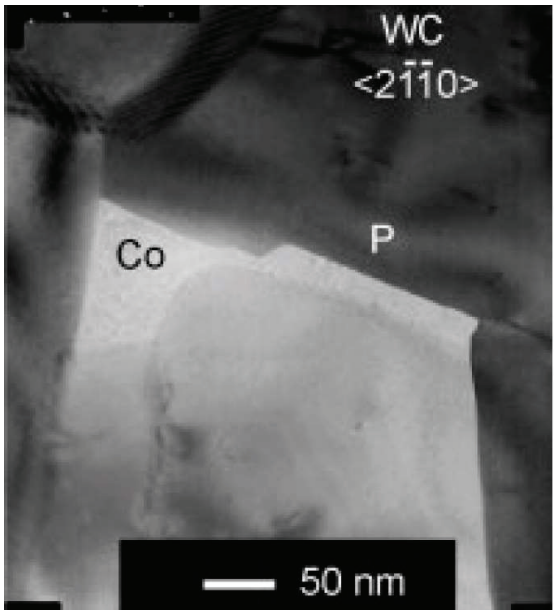

(c) W-rich

Figure 3.12: TEM images of a perfectly faceted WC grain and sharp WC/Co phase boundaries in a C-rich WC–Co cemented carbide (a), and stepped WC/Co phase boundaries in a W-rich WC–Co cemented carbide (b,c) [109].

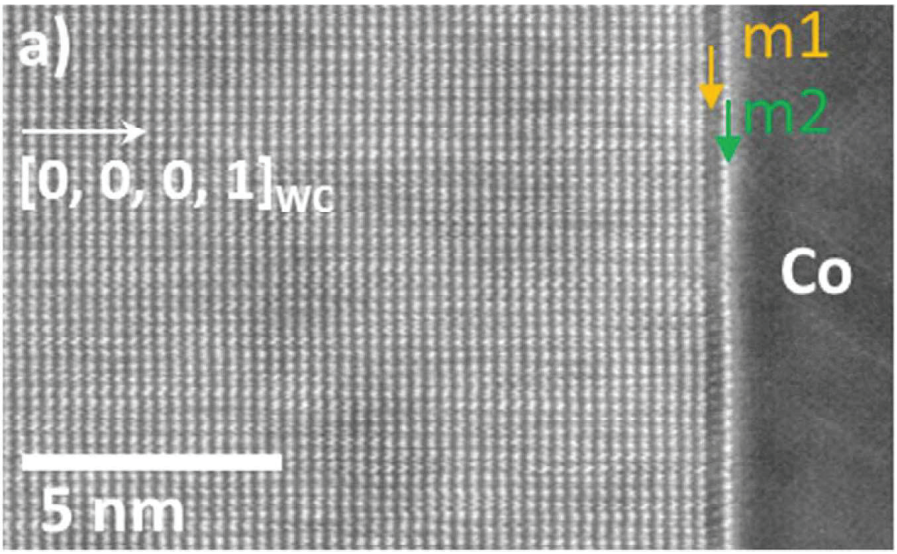

Figure 3.13: HRTEM image of a (Ti,W)C_{1-x} film in a TiC doped cemented carbide [110]. The film has a thickness of two metallic layers. Ti atoms are found to segregate to the first layer (m1) of the film, leaving one layer of W atoms (m2) towards Co.

4

Thermodynamics

”A theory is the more impressive the greater the simplicity of its premises is, the more different kinds of things it relates, and the more extended is its area of applicability. Therefore the deep impression which classical thermodynamics made upon me. It is the only physical theory of universal content concerning which I am convinced that within the framework of the applicability of its basic concepts, it will never be overthrown. ”

– Albert Einstein [118]

4.1 Phase diagrams

Phase diagrams give the occurrence of stable phases as a function of the macroscopic thermodynamic parameters temperature T, (external) pressure P and system composition X. The binary W-C phase diagram, containing bcc W, graphite, δ-WC and γ-WC is important for understanding the formation of complexions at phase boundaries between WC and Co in undoped WC–Co cemented carbides, see Sec. 4.3. Further, in the manufacturing of cemented carbides the phase constitution in the W-C-Co system at various temperatures and compositions is a crucial parameter, see Sec 2.3. In Paper IV, the phase stability between the hexagonal δ-WC and the cubic γ-WC phases is investigated and a phase diagram for bcc W, graphite, δ-WC and γ-WC is constructed based on DFT calculations.

Traditionally, phase diagrams have been decided upon experimental observations. However, if one is to calculate a phase diagram, one must first calculate, either numerically or analytically, the free energy of the different phases (or structures) at relevant

temperatures and compositions. Then, the total free energy of the system must be minimized by varying the amount of each phase given the macroscopic thermodynamic parameters.

The free energy relevant for a system of fixed T and P is Gibbs free energy, G, which is given by

$$G = U - TS + PV, \tag{4.1}$$

where U is the internal energy, S the entropy and V the volume. In Paper IV we only consider the zero pressure case, hence the PV term vanishes and Helmholtz free energy, i.e. $F = U - TS$, equals G. To find the equilibrium free energy for a phase with N number of atoms at temperature T and zero external pressure, F is minimized with respect to the system volume while keeping T and N fixed.

The free energy is commonly divided into various contributions such as configurational, vibrational, electronic and magnetic. How these contributions are treated in the thesis is presented in Chapter 6.

If we denote the structure or phase by α the free energy of structure α with chemical composition x and temperature T may be denoted $G_\alpha(x, T)$. It is often convenient to define a mixing free energy, i.e., the free energy of the system relative to the free energies in the corresponding pure phases for all constituents. In a hypothetical A-B binary system the mixing free energy for composition $x = n_\mathrm{B}/n_\mathrm{A}$, where n_i is the amount of element i, will be defined as

$$G_\alpha^{\mathrm{mix}}(x, T) = G_\alpha(x, T) - \left(\frac{\mu_\mathrm{A}(T) + x\mu_\mathrm{B}(T)}{1 + x} \right). \tag{4.2}$$

Here, $\mu_\mathrm{A}(T)$ and $\mu_\mathrm{B}(T)$ are the free energies in the pure A and pure B phases, respectively. Once $G_\alpha^{\mathrm{mix}}(x, T)$ is known, a convex hull may be generated. The convex hull is the free energy per atom in a system of composition X at temperature T. It is found by minimizing the free energy of the system with the amount of each phase α and its individual composition as free variables. A common effect of this is that you get a miscibility gap, i.e., a composition range where the system decomposes into two phases with compositions different from the that of the whole system[119]. An illustration of how the convex hull is constructed for the hypothetical binary A-B system is shown in Fig. 4.1a. Using the convex hull for various temperatures allows for construction of a temperature vs. concentration phase diagram. An illustration of the phase diagram for an imaginary two phase system is shown in Fig. 4.1b. The miscibility gap is illustrated as a two phase region.

4.2 Interface and surface free energy

Thermodynamics of interfaces and surfaces in cemented carbides determine to a large degree the microstructure after sintering, which in turn determine the mechanical

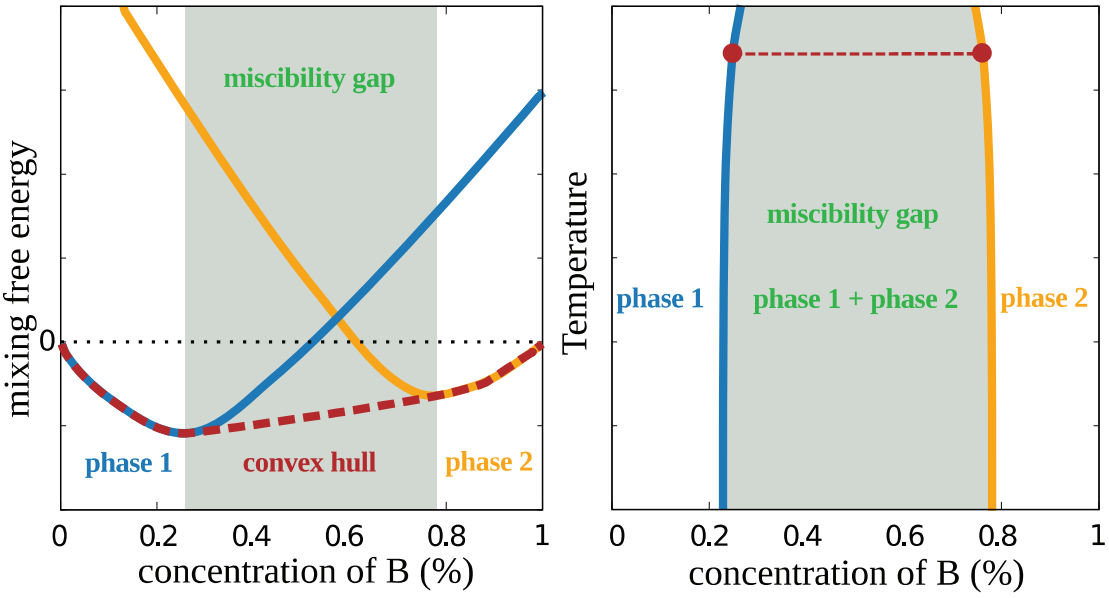

(a) Figure showing convex hull at a certain temperature for a hypothetical binary A-B system. Adapted based on Fig. 3.6b in Ref. [120]

(b) Example of how the phase diagram might look like for the a hypothetical binary A-B system. The dotted red line indicates the convex hull from (a). Adapted based on Fig. 3.6c in Ref. [120]

properties of the material [58, 84]. All appended papers but Paper IV deal with aspects of interface and surface energetics in cemented carbides. The fundamental quantity related to the creation of an interface/surface is the interface/surface free energy, γ [97]. To define γ, we must first define the interface/surface system rigorously. We may consider only the more general case of interfaces since surfaces are a special case that can be defined analogously to interfaces. Let us consider two phases which are in contact along a planar interface of area A. The interface system is in equilibrium with reservoirs which provide the system with atoms. The entire system, i.e. the two phases, the dividing interface and the reservoirs, are held at constant temperature T, pressure P and chemical potential μ_i for each of the components. Additionally, the two adjoining bulk phases are assumed to be large in comparison with the interface system. By using a combination of the first and second laws of thermodynamics, the change in total energy, U, due to a reversible change of the interface system may be written as

$$\mathrm{d}U = T\mathrm{d}S - P\mathrm{d}V + \sum_{i=1}^{C} \mu_i \mathrm{d}N_i + \gamma \mathrm{d}A, \tag{4.3}$$

where S is the entropy, V the volume of the entire interface system, C the number of components and N_i the number of atoms of component i. This is analogous to the expression for a bulk system, apart from the last term $\gamma \mathrm{d}A$, which is added to account for the change in total energy associated with a change in area of the interface. Directly form Eq. (4.3) we get

$$\gamma = \left[\frac{\partial U}{\partial A}\right]_{S,V,N_i}, \tag{4.4}$$

which means that the interface free energy is defined as the change in total energy of the interface system per unit increase in interface area, at constant S, T, and N_i. However, it turns out that relating γ to Gibbs energy G gives the most useful expressions for atomistic calculations. If we integrate Eq. (4.3), we obtain

$$U = TS - PV + \sum_{i=1}^{C} \mu_i N_i + \gamma A, \tag{4.5}$$

which can be combined with the definition for G, see Eq. (4.1) to get

$$\gamma = \frac{1}{A}\left[G - \sum_{i=1}^{C} \mu_i N_i\right]. \tag{4.6}$$

This means that γ is the excess Gibbs energy per unit interfacial area due to the presence of the interface.

4.3 Complexions and interfacial phase diagrams

Often, interfaces (or surfaces) are considered as two dimensional (planar) defects with no out-of-plane extent. However, in many cases atoms segregate to the interface, thus changing the chemistry near the interface. The structure near the interface may also differ from the structure of the adjoining phases. Both the structure and chemistry may, therefore, change continuously across the interface rather than abruptly at a dividing surface. Further, in some cases, the interfaces may be considered as quasi-two-dimensional "phases" that, similar to ordinary bulk phases, may undergo phase-like transitions in which their structure and chemistry changes abruptly at critical values of thermodynamic parameters [121]. Since these interface phases should not be confused with ordinary phases they may be referred to as complexions. Cantwell *et al.*[121] presented the following definition for complexions: "A complexion, concisely defined, is interfacial material or strata that is in thermodynamic equilibrium with the abutting phase(s) and has a stable, finite thickness that is typically on the order of 0.2–2 nm. A complexion cannot exist independently of the abutting phases and its average composition and structure need not be the same as the abutting phases."

In WC–Co cemented carbides complexions are most frequently observed in WC/Co phase boundaries [10, 12, 11, 110] and we, therefore, only consider complexions in WC/Co phase boundaries. Further, in WC/Co phase boundaries complexions are commonly referred to as thin films.

We can study the stability of the thin films by introducing a simple model in which the original phase boundary, which has no thin film, is removed and replaced by two new phase boundaries plus a thin cubic bulk MC phase[122]. Here, M may denote either dopants such as Ti and V, but also W in the case of undoped WC–Co cemented carbides. The interface free energy of the original phase boundary is denoted $\gamma_{\mathrm{WC/Co}}$ and the interface free energy, i.e, the excess free energy per unit area, of the thin film system may be written as

$$\gamma_{\mathrm{film}} = \gamma_{\mathrm{WC/MC}} + \gamma_{\mathrm{MC/Co}} + N\left(\Delta g_{\mathrm{MC}} + e_{\mathrm{MC}}\right), \tag{4.7}$$

where $\gamma_{\mathrm{WC/MC}}$ and $\gamma_{\mathrm{MC/Co}}$ are the interface free energies of the phase boundaries between hexagonal WC and cubic MC and cubic MC and Co, respectively. Further, N is the number of cubic layers and Δg_{MC} is the free energy cost for creating the MC phase per layer relative to reference states of the included elements, and e_{MC} is the strain energy introduced when matching the film with WC. For a film to be stable, $\gamma_{\mathrm{film}} < \gamma_{\mathrm{WC/Co}}$ must be fulfilled. Further, since the last two terms Eq. (4.7) can not be negative a necessary condition for stabilizing a film is

$$\gamma_{\mathrm{WC/Co}} - \left(\gamma_{\mathrm{WC/MC}} + \gamma_{\mathrm{MC/Co}}\right) > 0, \tag{4.8}$$

i.e., the total interface free energy of the thin film system, disregarding Δg_{MC} and e_{MC}, must be lower compared with the interface free energy of the original phase boundary. If this condition is fulfilled it is possible to stabilize films even if the bulk MC phase is not stable. This simple model demonstrates how stabilizing thin films is a process that is governed by interface energetics. The thickness of the film is chosen such that γ_{film} is minimized. Further, the structure, i.e. orientation and translation, of the film relative to the original phase boundary must be optimized.

Using this methodology and approximating the free energies with total energies calculated from density functional theory (DFT), thin films are predicted to form in VC doped WC–Co cemented carbides but not when the material is doped with TiC [122]. Further, this method predicts that thin films in undoped WC–Co cemented carbides should be highly unfavourable, see Paper V. However, in all these cases complexions has been observed experimentally [10, 12, 11, 110]. To predict stable films in TiC doped and undoped WC–Co cemented carbides it is necessary to use free energies rather than total energies from VASP. This includes modeling configurational, vibrational, and electronic free energies. The composition of film must also be optimized. Further, for ultrathin films with only a few atomic layers of MC phase it may not suitable to assume that the two interfaces surrounding the film are non-interacting. Therefore, it is necessary to treat the film as one entity and compute the excess free energy of the entire film.

If we use the definition of interface free energy from Eq. (4.6) the interface free energy for the interface/thin film in a closed system with only one interface/thin film with n_i atoms of each kind and structure α is given by

$$\gamma(T, n_\mathrm{i}, \alpha) = \frac{1}{A}\Big(G(T, n_\mathrm{i}, \alpha) - \sum_i n_\mathrm{i}\mu_i(T)\Big),$$

where $G(T, n_\mathrm{i}, \alpha)$ is the total free energy of the interface system, A the total interface area and $\mu_i(T)$ the chemical potential of species i for a given temperature. $\mu_i(T)$ are related to the actual composition of the entire cemented carbide, X. Since the composition of the thin film is negligible when considering the composition of the whole cemented carbide, both n_i and α are optimized to give the interface free energy for the interface/thin film system, $\gamma(T)$. An interfacial phase diagram will give the optimal structure α given some thermodynamic parameters such T and X or T and μ_i.

In Papers V and VI we optimize the interface structure and chemistry of WC/Co interfaces by calculating the change in interface free energy, $\Delta\gamma$, relative to an ideal WC/Co interface structure, α_ideal, according to

$$\Delta\gamma(T, n_\mathrm{i}, \alpha) = \gamma(T, n_\mathrm{i}, \alpha) - \gamma(T, n_\mathrm{i,ideal}, \alpha_\mathrm{ideal}) \tag{4.9}$$

for various structures, chemical potentials and temperatures. The model structures of Papers V and VI are presented in Sec. 5.4.2. By calculating the relative free energy to α_ideal, the absolute free energy is not needed for any state, which allows for a lot of simplifications and cancellations. Further, the optimal interface structure and composition can be found by minimizing $\Delta\gamma$. This modeling uses the thermodynamic paramters: T and μ_i, which are most suitable for atomistic calculations. However, the chemical potentials may be linked to the overall composition using other thermodynamic data, e.g., from the Thermo-Calc software [123]. In this way, interfacial phase diagrams given T and X or T and μ_i may be constructed.

4.4 Interface and surface stress

Another important quantity, which is related to the interface/surface free energy, is the interface/surface stress τ_{ij} [97]. The stress arises due to the different environment at the interface/surface compared to the bulk. For example, at the surface of a metal the atomic bonds are usually stronger than in the bulk since there are fewer bonds at the surface in which the valence electrons reside. As a consequence, the atoms at the surface would like to contract to get closer spacings. However, if the surface layer does not reconstruct and if no defects are introduced near the surface, the atomic spacing in the surface plane are equal to the ones in the bulk, i.e. it is completely coherent. Maintaining this coherency requires internal stresses parallel to the surface plane. The

bulk thus exerts a tensile stress on the surface while the surface exerts a compressive stress on the bulk.

Since the stress exerted by the bulk and interface/surface are parallel to the interface/surface plane, the interface/surface stress, τ_{ij}, is a rank 2 tensor where the perpendicular directional dependence of the regular bulk stress has been removed by means of integration along the perpendicular direction. Its dimension is therefore the same as that for interface/surface free energy, γ, and not to that of excess stress per area. The terms *interface stress* and *surface stress* are therefore a bit unfortunate. It is possible to obtain a relation between τ_{ij} and γ if a small strain $\mathrm{d}\epsilon_{ij} = \mathrm{d}\epsilon = \frac{\mathrm{d}A}{A}$ is applied parallel to the interface or surface plane. For simplicity we assume that the interface/surface stress is independent on direction, i.e. $\tau_{ij} = \tau$. The change in G from the interface/surface is $\mathrm{d}(\gamma A)$ and since the bulk is balancing the stress from the interface/surface, the work done in stretching the bulk must be $-\tau \mathrm{d}A$. Additionally, since the whole system is relaxed, i.e., there is no net stress on the system, the work involved in stretching, and thus the change in G, is zero. We therefore end up with

$$\mathrm{d}G = \mathrm{d}(\gamma A) - \tau \mathrm{d}A = 0, \tag{4.10}$$

which may be simplified to

$$\tau = \gamma + A\frac{\mathrm{d}\gamma}{\mathrm{d}A}, \tag{4.11}$$

which is known as the Shuttleworth equation [124].

For a liquid surface, the last term of Eq. (4.11) is zero since the atoms are free to move to or away from the surface when it is strained [97]. The surface stress, which in this case is commonly called surface tension, is then equal to the surface free energy. This equality is used to calculate liquid surface free energies in Paper II. In solids, however, the magnitude of $A\frac{\mathrm{d}\gamma}{\mathrm{d}A}$ may be comparable to γ.

4.5 Wetting

4.5.1 Wetting of surfaces

Wetting is an important technological parameter for many material processes including joining, solidifcation, and composite processing [3]. In the sintering of cemented carbides the wettability of the binder phase on the carbide is important to achieve desired densifiaction. Wetting is a measure of the interfacial energies in a system, and is therefore a parameter associated with equilibrium thermodynamics. A concept related to wetting and of equal importance for technological processes is spreading, which is the rate by which a liquid spreads in contact area with a solid. However, this is a non-equilibrium process which can not be investigated using equilibrium interfacial energies. Wetting is fundamentally governed by the chemical content and atomic structure

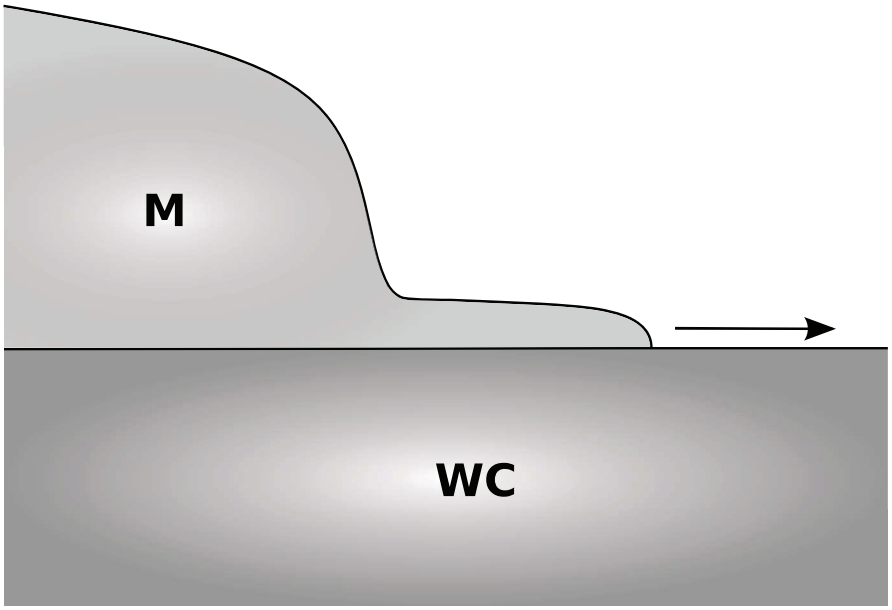

Figure 4.2: Figure showing spreading of binder phase (M) on a WC surface.

of the interfaces as well as bulk phases. In Paper I, the wetting of WC surfaces by the binder phase in WC–Co and WC–Ni cemented carbides is investigated.

The degree by which the binder phase wets a WC surface is determined by the balance between the energies of the three different interfaces that are formed during the wetting; the WC surface energy σ_{WC}, the WC/M phase-boundary energy $\gamma_{\mathrm{WC/M}}$, and the binder surface energy σ_{M}. A common measure of the degree of wetting is the spreading parameter S, which is defined as the difference in interface energy between the dry and wet case, i.e.

$$S = \sigma_{\mathrm{WC}} - (\gamma_{\mathrm{WC/M}} + \sigma_{\mathrm{M}}). \tag{4.12}$$

This parameter gives the driving force for a spreading similar to the one shown in Fig. 4.2, where the WC surface area is replaced with equal areas of phase boundary and binder surface. However, it does not give any direct input on the kinetics of the spreading process. With the above definition of the spreading parameter, the binder phase is assumed to be taken from a reservoir, large enough in order to omit the change of reservoir surface area, which implies that the total surface area of the binder increases during the spreading process.

From Eq. (4.12) it follows that it is energetically favourable for the binder to spread on the carbide, i.e. $S > 0$, if the total interface energy is smaller in the wet case compared to the dry case. This situation is referred to as perfect wetting. Otherwise, if spreading is unfavourable and $S < 0$, the wetting is only partial. The situation of partial wetting may be described by the contact angle θ between the binder and the carbide that forms

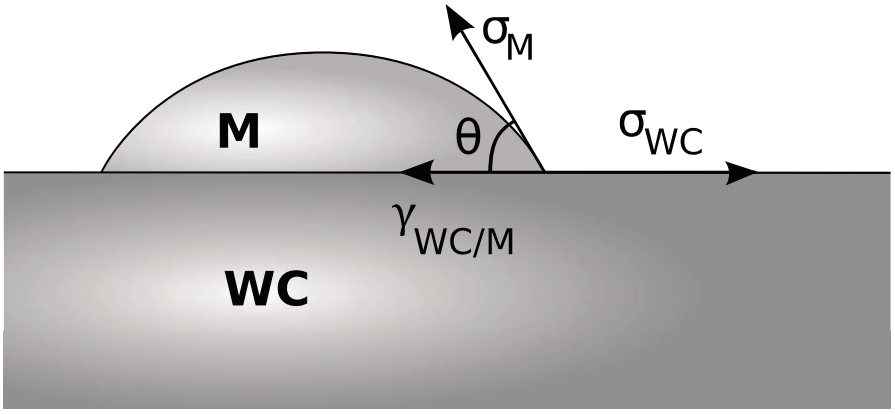

Figure 4.3: A binder (M) droplet on a WC surface with the contact angle θ.

when a drop of binder is placed on a WC surface, see Fig. 4.3. Traditionally the angle is said to be determined by considering the force balance from the surface stresses (surface tensions) in the WC interface plane between the three interface energies, which yields the Young equation

$$\cos\theta = \frac{\sigma_{\mathrm{WC}} - \gamma_{\mathrm{WC/M}}}{\sigma_{\mathrm{M}}}. \tag{4.13}$$

Combining the Young equation with the definition for S in Eq. (4.12) yields the Young-Dupré equation

$$\cos\theta = 1 + S/\sigma_{\mathrm{Co}} \quad (S \leq 0). \tag{4.14}$$

If $\theta = 180^\circ$, the system is non-wetting, i.e. the droplet will not form any phase boundary with the substrate, and if $\theta = 0^\circ$, there is perfect wetting. The relations in Eqs (4.13) and (4.14) can be conveniently used for studying changes in wetting experimentally [125].

The approach of force balancing for relating θ to the interface energies is not quite correct since there is no balance of forces perpendicular to the WC interface plane [125]. Further, as shown in Sec. 4.4, the interface stress is generally different form the interface free energy. There is another approach for relating θ to the interface energy that will yield the same set of equations, but which only considers the interface energies: If the shape of the droplet is assumed to be a spherical cap, then the contact angle and volume (area in the 2D representation in Fig. 4.3) of the drop can be related. Further, knowing the shape and volume of the cap, allows for determination of interface areas. Then, minimizing the total interface energy in the system under the constraint of preserving the volume of the drop then yields the relation in Eq. (4.13) [126]. This derivation only holds for droplets with the shape of a spherical cap, while in the presence of gravity the drop will deform. It is, however, possible to derive the Young equation, Eq. (4.13), for more general shapes of droplets that includes the presence of gravity [127, 128].

During sintering of WC-Co cemented carbides, a significant part of the densification occurs already during heating when the binder is still in the solid state [84]. This indicates that Co wets WC already before it melts while still in the solid state, and the same behaviour is expected for the other binders. When dealing with wetting with solid phases, the anisotropy of the interface energies and thus the crystal shapes should be taken into account [3]. Further, the concept of contact angle is not meaningful in a situation where a crystal wets a substrate since the apparent angle is highly sensitive to the anisotropic crystal shape. In Paper I, we therefore focus on the driving force for wetting, i.e. the spreading parameter.

In 1965, Ramqvist [125] performed wetting experiments of pure liquid Co and Ni on WC which indicated perfect wettability with $\theta \approx 0$. The pure formats of Co and Ni are, however, not representative for the binder alloys in a cemented carbide. In a more recent study, Konyashin *et al.* investigated the wettability of liquid Co rich binder alloys on WC with a varying carbon content [41]. In the experiments four different binder alloys was used: one W-rich containing eta phase (alloy 1), one W-rich but without eta phase (alloy 2), one C-rich without graphite formation (alloy 3), and one C-rich with graphite formation (alloy 4). Cylinders of these four alloys was placed on top of WC substrates an subsequently heated under controlled conditions to melt the binder alloy. The alloys were then kept in the liquid state for 35 s before cooling. The resulting appearance of the alloys after melting and cooling can be seen in Fig. 4.4. It is apparent that the wettability decreases with increasing carbon content. The low carbon alloys show a perfect wetting of the WC substrate, but for the high carbon alloys the wetting is only partial. The wetting angles of alloy 3 and alloy 4 where measured to 7 and 15 degrees, respectively, see Fig. 4.5. This increasing wettability with decreasing carbon content is in agreement with the increased shrinkage rate with decreasing carbon content during sintering observed by Bounhoure *et al.* in Refs [40, 38], see Sec. 2.2.

4.5.2 Wetting of grain boundaries

The binder phase in cemented carbides can also wet WC/WC grain boundaries by infiltrating them and thus replacing the grain boundary for phase boundaries, see Fig. 4.6. The excellent mechanical properties of cemented carbides are highly dependent on the existence of a continuous network of WC grains [4]. Therefore, the ability for WC/WC grain boundaries to resist infiltration by the binder phase is an important property and it is investigated in Paper I.

To avoid confusion with the wetting of WC surfaces we refer to the wetting of WC/WC grain boundaries as WC/WC grain boundary infiltration. The driving force for infiltration can be assessed by calculating an infiltration parameter W_{inf} equal to

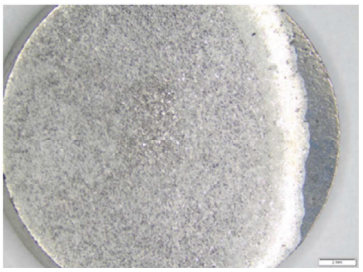

(a) Alloy 1 (W-rich with eta phase)

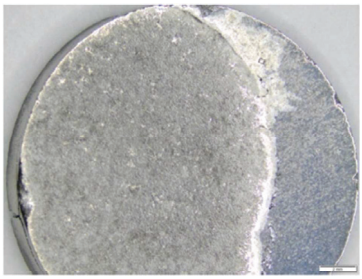

(b) Alloy 2 (W-rich)

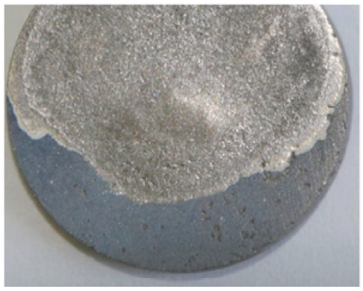

(c) (Alloy 3 (C-rich)

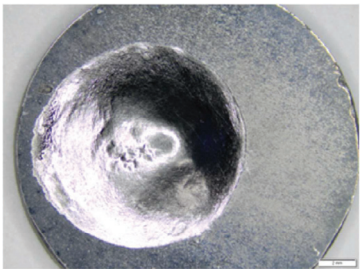

(d) Alloy 4 (C-rich with graphite)

Figure 4.4: Appearance of binder alloys on WC substrates after melting and cooling, (a)-(d) [41].

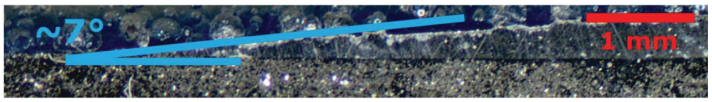

(a) Alloy 3 (C-rich)

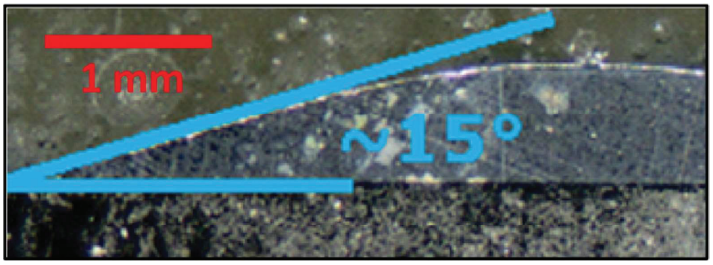

(b) Alloy 4 (C-rich with graphite)

Figure 4.5: Cross sections and contact angles of alloy 3 and alloy 4 on WC substrate [41]

the difference in interface energy between the dry and wet case:

$$W_{\text{inf}} = \gamma_{\text{WC/WC}} - (\gamma_{\text{WC/M,1}} + \gamma_{\text{WC/M,2}}). \tag{4.15}$$

It is thus favorable to replace a WC/WC grain boundary with two WC/M phase boundaries, i.e there is a thermodynamic driving force for grain boundary infiltration, if $W_{\text{inf}} > 0$. Otherwise, if $W_{\text{inf}} < 0$, the grain boundary will resist being infiltrated by binder phase.

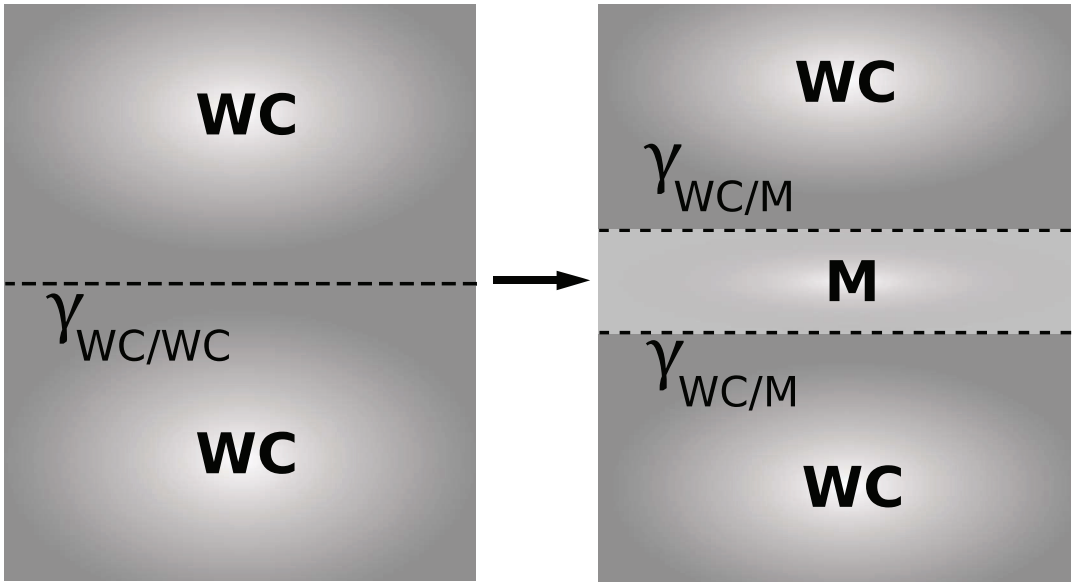

Figure 4.6: A schematic picture showing the energies involved in infiltrating a WC/WC grain boundary with binder phase (M).

4.5.3 Effect from changes in local chemistry and structure

Both the wetting of WC surfaces and WC/WC grain boundaries are sensitive to the local chemistry of interfaces and surfaces. Since the local chemistry effects the stoichiometry of the interfaces the dependence of the carbon content (carbon chemical potential) is also affected. If, for example, the stoichiometry of the equilibrated WC surface is different from that of the equilibrated WC/M phase boundary, the spreading parameter (Eq. (4.12)) will be sensitive to the carbon content in the material. This type of effect is investigated in Paper I for WC surfaces and WC/WC grain boundaries.

In the case of WC surfaces, adsorption of Co may affect wetting and spreading differently as wetting is governed by the balance of equilibrated interface energies, while spreading is a kinetic process where equilibration of interfaces may or may not occur

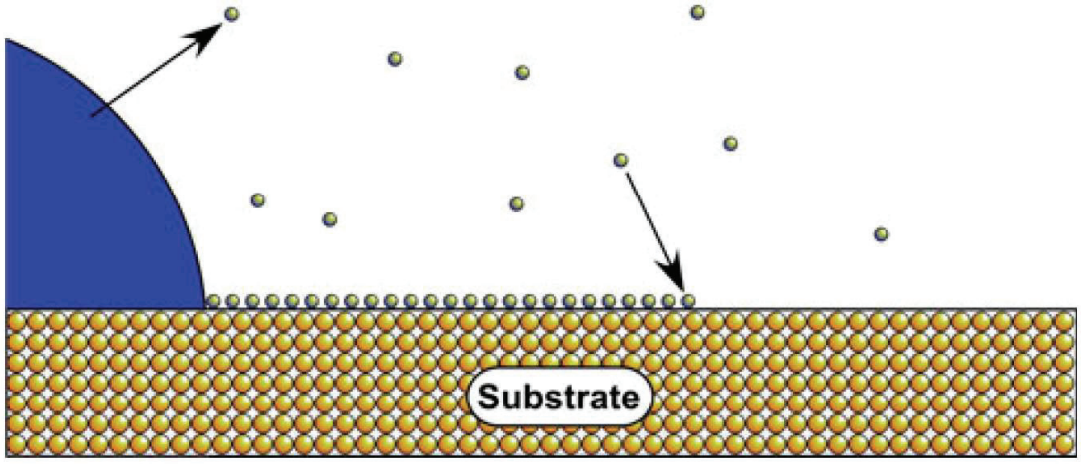

Figure 4.7: A schematic picture of the spreading of a liquid on a substrate, where the substrate surface can equilibrate by adsorbing atoms from the liquid phase either through the vapour phase or through diffusion along the substrate surface [3].

depending on the speed of the processes involved [3]. This is illustrated in Fig. 4.7, where a drop of liquid is spreading on a substrate where a precursor adsorbate of liquid phase atoms is present which either diffuse over the substrate or evaporate from the vapour and adsorb to the substrate surface. However, if the spreading is fast enough, the substrate will not equilibrate, and it is thus the clean substrate surface energy which is relevant for the driving force.

Changes in the local structure of interfaces and surfaces, i.e. the formation of complexions, will also have an effect on the wetting of WC surfaces and WC/WC grain boundaries since the interface and surface free energies are lowered. In cemented carbides complexions are most frequently observed at the phase boundaries between WC and Co. The wettability will, therefore, increase once these complexions can be formed. It is, however, not certain that the kinetic process of Co spreading on WC will be facilitated by complexions since the phase boundary may not be able to equilibrate and form the complexion at the same rate as the spreading.

4.6 WC/WC grain boundary strength

The excellent mechanical properties of cemented carbides are highly dependent on the strength of their interfaces [93, 92, 129, 130]. In Paper I we investigate the stability of the continuous WC skeleton by considering infiltration of Co binder phase using the infiltration parameter defined in Eq. (4.15). It is a parameter designed to match the spreading parameter for surfaces. Its value is the negative of the work required to

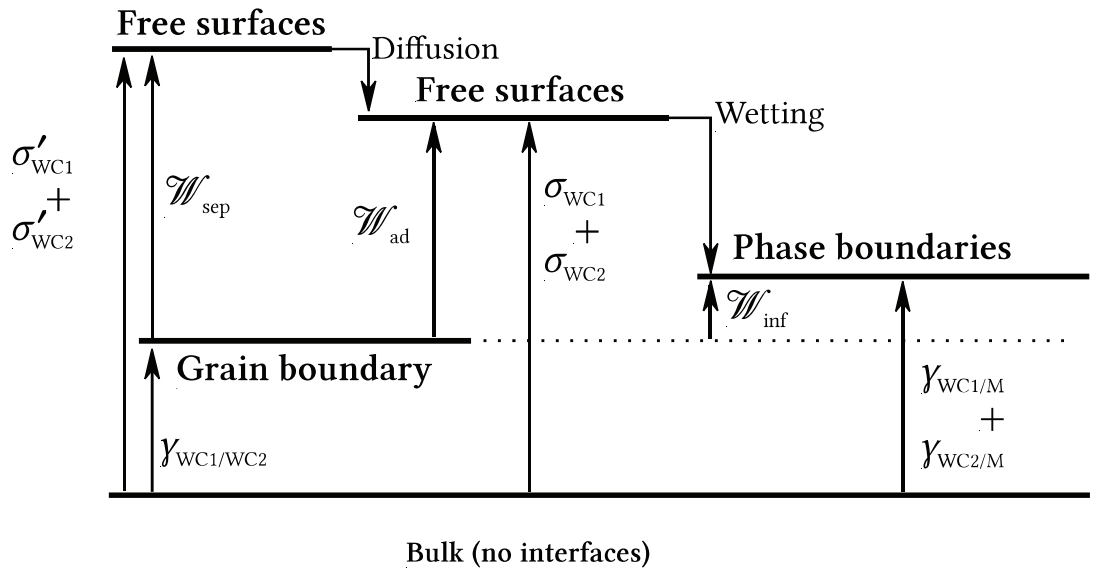

Figure 4.8: A diagram showing the energies involved in cleaving or infiltrating a WC/WC grain boundary, excluding plastic processes. This demonstrates the relation between $\mathscr{W}_{sep}$, $\mathscr{W}_{ad}$, and $\mathscr{W}_{inf}$. This diagram has been adapted from an original diagram relating $\mathscr{W}_{sep}$ and $\mathscr{W}_{ad}$ presented in Ref. [131].

infiltrate the grain boundary with Co, i.e. the work of infiltration $\mathscr{W}_{inf}$. The strength of a grain boundary, or a more general interface, can also be measured in terms of the work of adhesion $\mathscr{W}_{ad}$ and the work of separation $\mathscr{W}_{sep}$. A diagram of how these quantities are related for WC/WC grain boundaries is seen in Fig. 4.8. Here follows descriptions and derivations of the different work terms.

4.6.1 Work of adhesion

The work of adhesion $\mathscr{W}_{ad}$ is the reversible free energy change associated with transforming an interface into two free surfaces while keeping the system in equilibrium with its environment [131]. Hence, this corresponds to slow decohesion. An explicit expression for the work of adhesion can be derived by consider a closed, isothermal system where two phases are in contact along an interface of area A_0. An external device work $\mathscr{W}$ is required to separate the interface to two free surfaces under constant pressure P while keeping the chemical potentials μ_i uniform among all parts of the system, which in turn are allowed to exchange mass with one another. In order to quantify $\mathscr{W}$ we return to Eqs. (4.3), (4.5), and (4.1), where U and G were defined. If multiple

interfaces are included in the reversible change of the system, Eq. (4.3) becomes

$$\mathrm{d}U = T\mathrm{d}S - P\mathrm{d}V + \sum_{i=1}^{C} \mu_i \mathrm{d}N_i + \sum_{j=1}^{D} \gamma_j \mathrm{d}A_j, \tag{4.16}$$

where D is the number of interfaces with interface free energy γ_j and area A_j. By using Eq. (4.1) the change in Gibbs energy dG becomes

$$\mathrm{d}G = -S\mathrm{d}T + V\mathrm{d}P + \sum_{i=1}^{C} \mu_i \mathrm{d}N_i + \sum_{j=1}^{D} \gamma_j \mathrm{d}A_j. \tag{4.17}$$

From the definition of the process, the whole change in G, and hence the work done by the device, is covered by the interface term in Eq. (4.17), and we obtain

$$\mathrm{d}\mathscr{W} = \mathrm{d}G = \sum_{j=1}^{D} \gamma_j \mathrm{d}A_j. \tag{4.18}$$

In the case of a WC/WC grain boundary this can be written as

$$\mathrm{d}\mathscr{W} = \gamma_{\mathrm{WC/WC}} \mathrm{d}A_{\mathrm{WC/WC}} + \sigma_{\mathrm{WC1}} \mathrm{d}A_{\mathrm{WC1}} + \sigma_{\mathrm{WC2}} \mathrm{d}A_{\mathrm{WC2}}, \tag{4.19}$$

where $\sigma_{WC1,WC2}$ are the equilibrated surface energies, $\gamma_{\mathrm{WC/WC}}$ is the grain boundary energy and dA_i represents the change in their respective area. Here, the more common notation of σ for surface energies has replaced γ. From the definition of the process the surface areas should grow at the same rate $\mathrm{d}A = \mathrm{d}A_{\mathrm{WC1}} = \mathrm{d}A_{\mathrm{WC2}}$, and this should in turn be the negative of the change in grain boundary area, i.e. $\mathrm{d}A = -\mathrm{d}A_{\mathrm{WC/WC}}$. Consequently, Eq. (4.19) becomes

$$\mathrm{d}\mathscr{W} = \Big[\sigma_{\mathrm{WC1}} + \sigma_{\mathrm{WC2}} - \gamma_{\mathrm{WC/WC}}\Big]\mathrm{d}A. \tag{4.20}$$

The total work in the defined process is then

$$\mathscr{W} = \Big[\sigma_{\mathrm{WC1}} + \sigma_{\mathrm{WC2}} - \gamma_{\mathrm{WC/WC}}\Big]A_0. \tag{4.21}$$

The work of adhesion $\mathscr{W}_{\mathrm{ad}}$ should be expressed as work per area, and consequently

$$\mathscr{W}_{\mathrm{ad}} = \sigma_{\mathrm{WC1}} + \sigma_{\mathrm{WC2}} - \gamma_{\mathrm{WC/WC}}. \tag{4.22}$$

In an actual cleavage experiment, plastic processes require energy, and $\mathscr{W}_{\mathrm{ad}}$ is, therefore, a lower limit to the actual work required in a cleavage experiment.

The work of adhesion for a general solid/liquid phase boundary may be written as

$$\mathscr{W}_{\mathrm{ad}} = \sigma_{\mathrm{solid}} + \sigma_{\mathrm{liquid}} - \gamma_{\mathrm{solid/liquid}}. \tag{4.23}$$

If the liquid wets the solid partially, see Sec. 4.5, $\mathscr{W}_{\mathrm{ad}}$ may be expressed in terms of the contact angle θ and the liquid surface free energy σ_{liquid} according to

$$\mathscr{W}_{\mathrm{ad}} = \sigma_{\mathrm{liquid}} (1 + \cos\theta). \tag{4.24}$$

This equation is useful when doing experimental measurements of the adhesion strength of solid/liquid interfaces when the wetting is partial. By measuring the contact angle and the liquid surface energy the adhesion strength can be calculated.

4.6.2 Work of separation

The work of separation $\mathscr{W}_{\mathrm{sep}}$ is the reversible work associated with cleaving the interface, neglecting plastic work and equilibration of the resulting surfaces through diffusion processes [131]. This, therefore, corresponds to a fast decohesion. In the case of a WC/WC grain boundary it is defined as

$$\mathscr{W}_{\mathrm{sep}} = \sigma'_{\mathrm{WC1}} + \sigma'_{\mathrm{WC2}} - \gamma_{\mathrm{WC/WC}}, \tag{4.25}$$

where $\gamma_{\mathrm{WC/WC}}$ and $\sigma'_{WC1,WC2}$ is the grain boundary energy and the resulting unequilibrated surface energies, respectively. Since the equilibrated surface energies are lower than the unequilibrated ones, it follows that $\mathscr{W}_{\mathrm{ad}} \leq \mathscr{W}_{\mathrm{sep}}$. This is illustrated in Fig. 4.8.

4.6.3 Work of infiltration by the binder phase

The work of infiltration $\mathscr{W}_{\mathrm{inf}}$ is the work required to infiltrate a WC/WC grain boundary with binder phase and thereby replacing it with two phase boundaries, see Fig. 4.6. It is therefore defined as

$$\mathscr{W}_{\mathrm{inf}} = \gamma_{\mathrm{WC/M,1}} + \gamma_{\mathrm{WC/M,2}} - \gamma_{\mathrm{WC/WC}}, \tag{4.26}$$

where $\gamma_{\mathrm{WC/M,1}}$ and $\gamma_{\mathrm{WC/M,2}}$ are interface energies of the resulting phase boundaries. Since the phase boundary energies generally are much lower than the WC surface energies, $\mathscr{W}_{\mathrm{inf}} << \mathscr{W}_{\mathrm{ad}}$, which is illustrated in Fig. 4.8. The work of infiltration is the negative of the driving force for infiltration as defined in Sec. 4.5.2. With this definition of $\mathscr{W}_{\mathrm{inf}}$, infiltration is favourable if $\mathscr{W}_{\mathrm{inf}} < 0$ and unfavourable if $\mathscr{W}_{\mathrm{inf}} > 0$. However, one can argue that in order to infiltrate the grain boundary it first has to be cleaved and then infiltrated (wetted) by binder phase. Consequently, even if infiltration is energetically favourable, the barrier for infiltration is still roughly given by $\mathscr{W}_{\mathrm{sep}}$. Alternatively, if the infiltration occurs through a diffusional process where atoms in the grain boundary are interchanged, the barrier is more related to the activation energy for diffusion.

5

Model geometries of interfaces and surfaces in cemented carbides

As stated in Sec. 4.2, the fundamental quantity related to the formation of an interface (surface) is the interface (surface) free energy γ [97]. The value of γ will depend on the thermodynamic parameters for the reservoir: e.g. temperature and composition [132]. The pressure contribution is here assumed to be negligible. If γ is minimized given these parameters an interfacial phase diagram may be created. However, a few geometrical parameters must be set to specify which interface or surface γ refers to.

Consider the general case of an interface between two solid grains. The first geometrical parameter to be set is the relative rotation between the grains[132]. Secondly, the interface normal for each grain needs to be specified. These macroscopic degrees of freedom are enough to specify the interface. For a solid/liquid interface or solid surface only the interface normal of the solid needs to be specified. Further, for a liquid surface there are no degrees of freedom.

There are additional microscopic degrees of freedom which need to be optimized in order to find the equilibrium interface geometry and γ. These include the relative translation displacement between the two grains and the translational displacement of the grain boundary plane along its normal direction relative to the two crystal lattices. Further, the local structure and composition in the interface must be optimized. This is where formation of complexions and segregation is included. All of these microscopic parameters must be optimized simultaneously as, for example, changes in the local structure might effect the optimal translation displacement between the grains.

In Sec. 3.3, experimental findings from the literature regarding the morphology of WC/Co phase boundaries and WC/WC grain boundaries in WC–Co cemented carbides were presented. The most important finding was that 80% of WC/Co phase boundaries and 60% of WC/WC grain boundaries can be classified as having a boundary plane that

is either basal or prismatic. We use this information to construct model WC/WC grain boundaries, WC/binder phase boundaries, WC surfaces, and binder surfaces which are appropriate for atomistic calculations. The binder/binder grain boundaries are omitted since, in WC–Co cemented carbides, Co grains generally are much larger than WC grains [77, 58] and the Co/Co grain boundaries therefore do not contribute as much to the properties of the final material as do the other interfaces. Moreover, in Ti doped cemented carbides, which are studied in Paper VI, or other doped cemented carbides, the gamma phase (Ti rich cubic carbide) will precipitate if the concentration of dopant is large enough. These precipitates will effect the microscopic properties of the material. However, in Paper VI we are only interested in the formation of TiC films/complexions at WC/Co phase boundaries for concentrations below the solubility limit of Ti in the binder. Hence, general interfaces with gamma phase are disregarded.

Since DFT calculations are quite computationally heavy, rather small repeating unit cells (only up to hundreds of atoms) are required. However, using a faster computational method, like an inter-atomic potential, the system sizes can be increased significantly. The model WC/binder phase boundaries, WC surfaces, and binder surfaces are constructed based on WC planes in the model grain boundaries. Further, all atomic structures are generated using the Atomic Simulation Environment (ASE) [1].

5.1 WC/WC grain boundaries

When searching for model grain boundaries we use the $c/a = 1$ approximation. In order to get small repeating unit cells for the model grain boundaries, a small coincidence site lattice index Σ (defined in Sec. 3.3) is required. As stated in Sec. 3.3.1, the $\Sigma = 2$ twist grain boundary is the most common grain boundary and it associated with very low interfacial energy. However, as the $\Sigma = 2$ twist grain boundaries originate already from the powder [102] they do not play an essential role in the formation of the final continuous skeleton of hard WC grains. They are, therefore, not an appropriate choice as model for a more general grain boundary relevant for studying the stability of the WC skeleton. The second most common grain boundary is the $30^\circ/[0001]$ grain boundary, most frequently bound by two basal planes, which has a coincidence site lattice index of $\Sigma = 13$ [85, 58]. Due, to its rather high Σ-value it requires quite large repeating unit cells which makes it inappropriate for DFT calculations. The third most common grain boundary was found to be $90^\circ/[1\bar{2}10]$ which were mostly bound by one basal and one prismatic WC plane. However, since the coincidence site lattice index for this grain boundary is very high, $\Sigma = 97$, it is not appropriate for DFT calculations. We therefore have to look for other grain misorientations that give rise to low Σ-values.

The two lowest possible Σ-values are $\Sigma = 2$ and $\Sigma = 4$ which are the results of $90^\circ/[10\bar{1}0]$ and $60^\circ/[1\bar{2}10]$, respectively. Instead of the pure twist $\Sigma = 2$ grain boundary we therefore choose the $\Sigma = 2$ tilt grain boundary, bound by one basal and one $(1\bar{2}10)$

plane, as a model grain boundary. The basal boundary planes can be seen in Figs 5.1a and 5.2a, and the and $(1\bar{2}10)$ boundary planes can be seen in Figs 5.1c and 5.2c. This type of grain boundary has been observed experimentally in Ref. [133]. We also choose the $60^{\circ}/[1\bar{2}10]$ $\Sigma = 4$ tilt grain boundary bound by one prismatic and one $(10\bar{1}2)$ plane as a model grain boundary. The prismatic boundary planes can be seen in Figs 5.1b and 5.2b, and the $(10\bar{1}2)$ boundary planes is seen in Figs 5.1d and 5.2d. Experimental findings indicating the presence of this $\Sigma = 4$ grain boundary in cemented carbides is found in Ref. [134]. This choice of model grain boundaries ensures that we end up with small repeating unit cells as well as having grain boundaries bound by at least one basal or one prismatic WC plane.

We use the $c/a = 1$ approximation to choose our model grain boundaries. However, in the DFT calculations in Paper I we fix the simulation cells in the interface plane but use vacuum regions at the two remaining WC planes not in the grain boundary. This means that the systems are allowed to relax in the direction perpendicular to the interfaces. Since the orientation of the grains in a grain boundary are different they will relax differently. To solve this, we vary the value of $a = c$ and choose the value where the two grains relax, perpendicular to the grain boundary planes, such that the energy of a WC unit is equal in both grains. The two grains are thus in equilibrium with each other and we use the strained WC phase as reservoir for the grain boundary system. In the temperature dependency calculations in Paper II the atoms in the bulk of the model systems are not allowed to relax, but only those near interfaces, consequently, the value for $a = c$ can be kept the same for both adjoining WC phases. The value for $a = c$ is found from thermal expansion calculation of bulk WC with the constraint of $a = c$.

5.1.1 $\Sigma = 2$ model grain boundaries

Due to the lack of mirror symmetry of the prismatic planes, see Sec. 3.1, it is possible to construct two different $\Sigma = 2$ tilt grain boundaries that are not related by an interface translation. By rotating one of the grains 180° around an axis perpendicular to the prismatic axis (e.g. the basal or $[1\bar{2}10]$ axes), the lattice is equivalent, however, the positions of the C atoms has changed. This means that prismatic axis of the rotated grain has changed form type S (T) to type T (S). See Sec. 3.1 for more details regarding S and T type. The interface relations for the two $\Sigma = 2$ tilt grain boundaries are

$$\Sigma = 2_1 : \quad (0001) \parallel (1\bar{2}10), \quad [10\bar{1}0] \parallel [10\bar{1}0], \tag{5.1}$$

$$\Sigma = 2_2 : \quad (0001) \parallel (1\bar{2}10), \quad [\bar{1}010] \parallel [10\bar{1}0]. \tag{5.2}$$

The basal plane can be either W or C terminated, while the mixed $(1\bar{2}10)$ is invariant, up to a translation, under the addition or removal of atomic layers. The fully relaxed $\Sigma = 2_1$ grain boundary can be seen in Fig.5.3a.

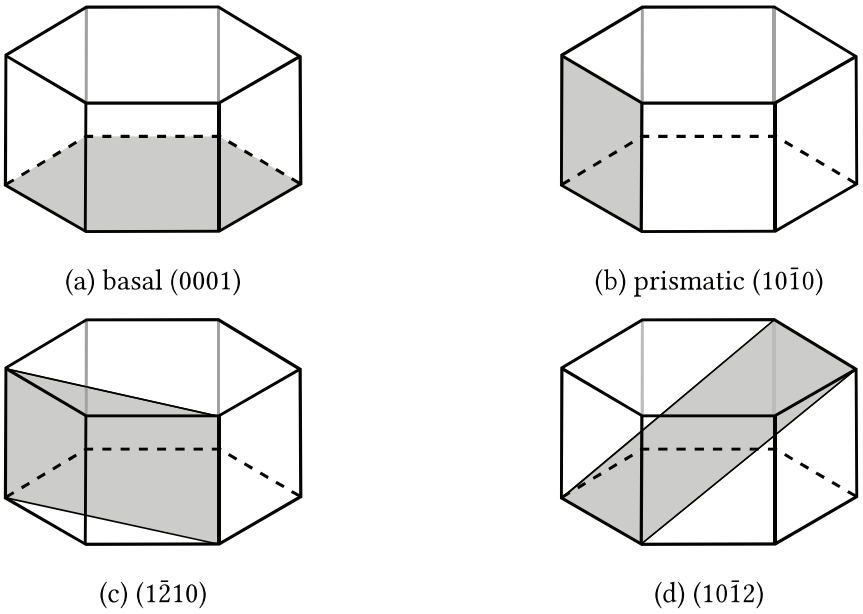

(a) basal (0001) (b) prismatic $(10\bar{1}0)$

(c) $(1\bar{2}10)$ (d) $(10\bar{1}2)$

Figure 5.1: Low index WC planes used in the two $\Sigma = 2$ and four $\Sigma = 4$ grain boundaries. The hexagonal prism correspond to the structure in Fig. 3.3

5.1.2 $\Sigma = 4$ model grain boundaries

Both the $(10\bar{1}0)$ and $(10\bar{1}2)$ planes lack mirror symmetry and should therefore be marked with the subscript S or T denoting their type. By changing the types of the WC planes it is possible to construct four different $\Sigma = 4$ tilt grain boundaries that are not related by an interface translation. The type is changed upon a rotation of 180° around an axis perpendicular to the prismatic axis. The interface relations for the four $\Sigma = 4$ tilt grain boundaries are

$$\Sigma = 4_1 : \quad (\bar{1}010)_T \parallel (\bar{1}012)_S, \qquad [0001] \parallel [10\bar{1}1], \tag{5.3}$$

$$\Sigma = 4_2 : \quad (\bar{1}010)_T \parallel (\bar{1}012)_T, \qquad [0001] \parallel [\bar{1}01\bar{1}], \tag{5.4}$$

$$\Sigma = 4_3 : \quad (\bar{1}010)_S \parallel (\bar{1}012)_S, \qquad [000\bar{1}] \parallel [10\bar{1}1], \tag{5.5}$$

$$\Sigma = 4_4 : \quad (\bar{1}010)_S \parallel (\bar{1}012)_T, \qquad [000\bar{1}] \parallel [\bar{1}01\bar{1}]. \tag{5.6}$$

In this way the $\Sigma = 4_1$ and $\Sigma = 4_4$ boundaries are $60°/[1\bar{2}10]$ tilt grain boundaries [100, 102], while the $\Sigma = 4_2$ and $\Sigma = 4_3$ boundaries correspond to $240°/[1\bar{2}10]$ grain boundaries. Both the $(10\bar{1}0)$ and $(10\bar{1}2)$ planes can be either W or C terminated which means that there are four different termination possibilities for each $\Sigma = 4$ tilt grain boundary. We denote the termination of a WC plane by an additional subscript such that $(10\bar{1}0)_{S,W}$ is a W terminated prismatic plane of type S. The fully relaxed $\Sigma = 4_1$ grain boundary can be seen in Fig. 5.3b.

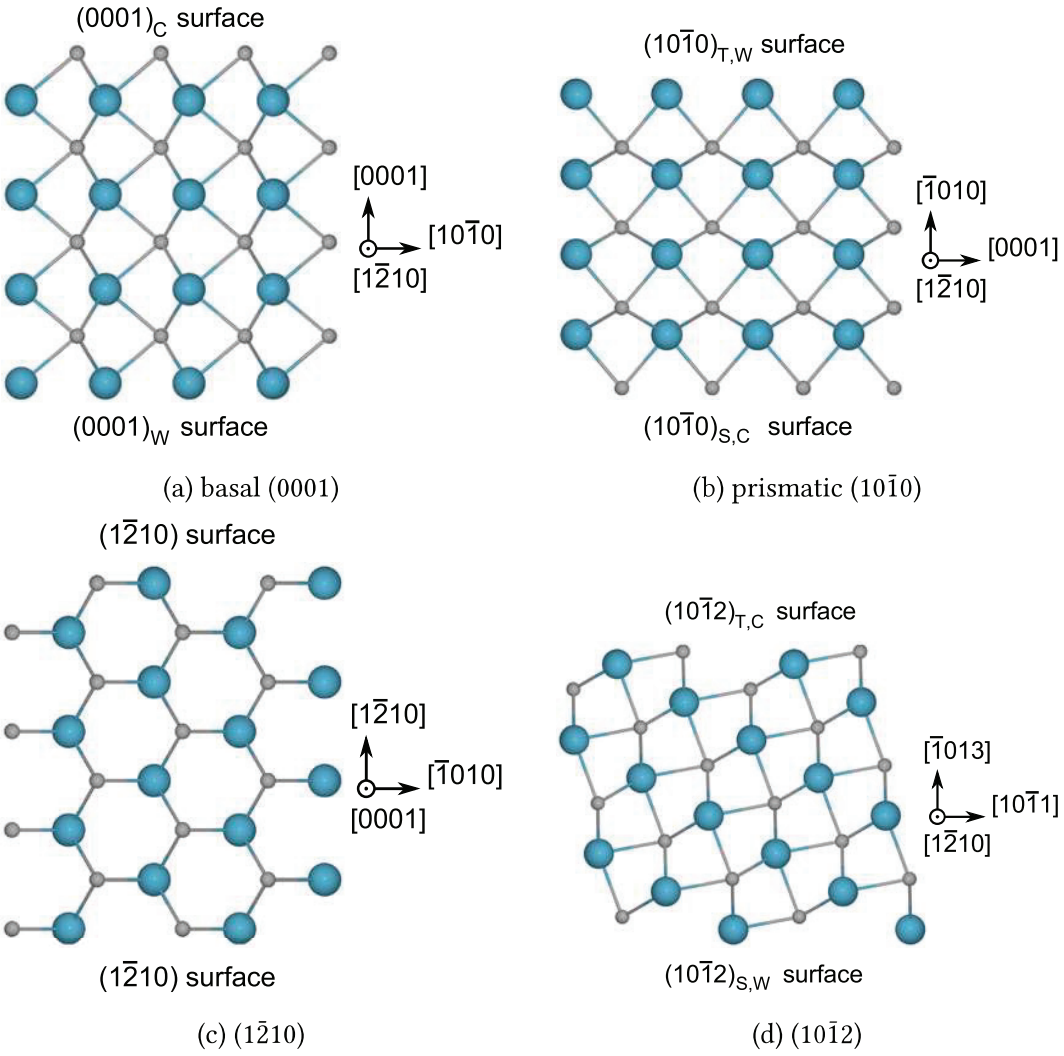

(a) basal (0001)

(b) prismatic (10$\bar{1}$0)

(c) (1$\bar{2}$10)

(d) (10$\bar{1}$2)

Figure 5.2: Unrelaxed atomic structures of the low-index WC surfaces which are shown schematically in figure Fig. 5.1 [73]. Large cyan coloured atoms are W and small grey atoms are C.

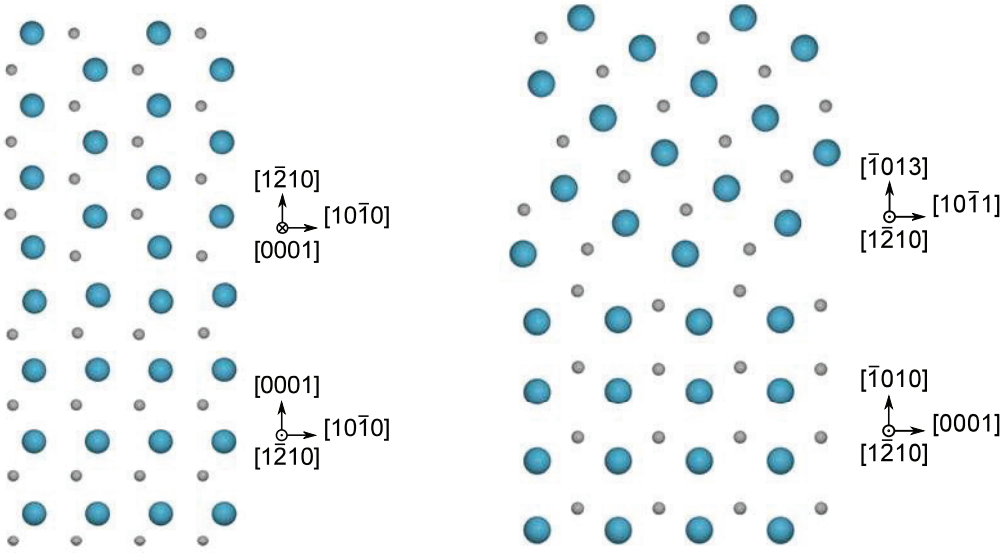

(a) $\Sigma = 2_1$ (b) $\Sigma = 4_1$

Figure 5.3: Geometries of the $\Sigma = 2_1$ and $\Sigma = 4_1$ grain boundaries [73]. Large cyan coloured atoms are W and small grey atoms are C. The figure shows the actual positions of the atoms in the fully relaxed minimum energy structures. The relaxation was done using DFT with the PBE exchange-correlation functional.

5.1.3 Incoherent grain boundaries

The DFT calculations in Paper I are all done on coherent grain boundaries with the c/a ratio fixed to unity. In Paper II and III an analytical bond order potential (ABOP) was used instead of DFT and the simulation cells could, therefore, be much larger. In Paper II, the same model grain boundary geometries are used but the unitcells are repeated in the grain boundary plane to get larger supercells. The same model grain boundary geometries are also used in Paper III, but now without $a = c$. Instead, the grain boundaries are generated to match the c/a ratio of 0.964 from the ABOP. Further, since various amounts of Co is added in between the two WC planes, the number of repeating unit cell in each direction is adapted to give a good match with bulk Co. As an example, the resulting $\Sigma = 2_1$ grain boundary has 31 units along the [0001] direction in the top grain (grain with (1$\bar{2}$10) boundary plane) and 30 units along the [1$\bar{2}$10] direction in the bottom grain (grain with (0001) boundary plane). The coherent $\Sigma = 2_1$ grain boundary can be seen in Fig. 5.3a. This construction generates incoherent grain boundaries with one dislocation plane per repeating unit cell.

5.2 WC/Binder phase boundaries

The model phase boundaries are created by matching the WC planes in the model $\Sigma = 2$ and $\Sigma = 4$ grain boundaries with fcc binder. In order for DFT calculations in Paper I to be feasible, the phase boundaries need to have a small repeating unit cells. However, this comes at the expense of straining the binder phases. The (0001) and $(1\bar{2}10)$ planes have matching repeating unit cells and are both matched with the fcc(111) plane to achieve minimal strain according to

$$(0001) \parallel (111), \quad [2\bar{1}\bar{1}0] \parallel [\bar{1}\bar{1}2], \tag{5.7}$$
$$(1\bar{2}10) \parallel (111), \quad [000\bar{1}] \parallel [\bar{1}\bar{1}2]. \tag{5.8}$$

The $(10\bar{1}0)$ and $(10\bar{1}2)$ plane are matched with the fcc(001) plane instead, and the interface relations are

$$(10\bar{1}0) \parallel (001), \quad [0001] \parallel [3\bar{1}0], \tag{5.9}$$
$$(10\bar{1}\bar{2}) \parallel (001), \quad [\bar{1}011] \parallel [3\bar{1}0]. \tag{5.10}$$

In the case of the (0001), $(10\bar{1}0)$ and $(10\bar{1}2)$ planes the termination can be either W and C, and the $(10\bar{1}0)$ and $(10\bar{1}2)$ planes have either type S or T. We end up with six unique model phase boundaries if we include the types S and T. The strain in the binder phases are on the order of 5% and it is the strained energy that is used as reservoir energy for the binder phase when the interface energy is calculated. The same model phase boundary geometries are calculated using an ABOP in Paper II, but similar to the model grain boundaries the phase boundary unitcells are repeated in the grain boundary plane to get larger supercells.

5.3 Surfaces

Similar to the phase boundaries we take the WC planes from six model grain boundaries and make model WC surface systems. If the type of the $(10\bar{1}0)$ and $(10\bar{1}2)$ planes are included we end up with 6 unique model WC surfaces: (0001), $(1\bar{2}10)$, $(10\bar{1}0)_{\mathrm{S}}$, $(10\bar{1}0)_{\mathrm{T}}$, $(10\bar{1}2)_{\mathrm{S}}$, and $(10\bar{1}2)_{\mathrm{T}}$. These are shown in Fig. 5.2. The planes of the binder phase in the phase boundaries are also used as model binder surfaces: fcc(111) and fcc(001). Again, small model surface supercells are used in Paper I for the DFT calculation, and larger supercells are used for ABOP calculations in Paper II.

5.4 Local chemical composition and local structure

5.4.1 Adsorption and segregation

The local chemistry of interfaces are important for thermodynamic properties such as the wettability [3]. In order to investigate effects from changes in the local chemistry of the interfaces, we model segregation of binder phase atoms to WC/WC grain boundaries and WC/binder phase boundaries, and adsorption of binder phase atoms to WC surfaces. This is done by systematically replacing W and C atoms in the vicinity of the interface for binder phase atoms. In the (0001), $(1\bar{2}10)$, and $(10\bar{1}0)$ planes the topmost layer is considered for substitution, while for the more corrugated $(10\bar{1}2)$ plane, the two topmost layers are considered. The substitutional sites for one WC surface, two WC/WC grain boundaries and one WC/M phase boundary is seen in Fig. 5.4.

In a previous study in Ref. [73], all possible terminations of the WC planes were tested for all model interfaces in WC–Co in order to minimize the interface energy. Additionally, all substitutions that corresponded to 0.5 or 1 monolayer (ML) proportion, was investigated. The minimization also included the effect from the chemical potential of carbon μ_C (carbon activity), which in some cases resulted in different optimal configurations depending on the value of μ_C. In Paper I, the same exhaustive search for the optimal configurations for the WC–Ni cemented carbides was not performed. Instead, the configurations in WC–Co which gave minimum energies for 0 (clean), 0.5 and 1 ML of substituted Co, respectively, are used. This is motivated by the similarity of the three binders.

5.4.2 Complexions

In Papers V and VI the formation of thin cubic films in WC/Co phase boundaries in both undoped and Ti doped WC–Co cemented carbides is investigated. Based on experimental observations in HRTEM [10, 12, 110] thin cubic films at the phase boundary between the δ-WC basal plane (0001) and the Co (111) plane are considered. The cubic films are oriented as to align the [111] direction with the basal plane, i.e.

$$\delta\text{-WC}(0001) \parallel \gamma\text{-MC}(111) \parallel \text{Co}(111),$$

where γ-MC denotes a general cubic carbide phase. In the undoped cemented carbide this will simply be the γ-WC phase while in a Ti doped cemented carbide M will be a mixture of W and Ti, i.e., (Ti,W)C.

In the [0001] direction of the δ-WC phase, W and C layers are alternating in an $ABABAB\ldots$ stacking sequence. Further, in the [111] direction of the γ-MC phase, M and C layers are alternating in an $ABCABC\ldots$ stacking sequence. Consequently, by altering the stacking sequence of a δ-WC structure, it can be converted into a γ-WC structure, and in this way multiple different δ-WC (0001) / γ-WC (111) interfaces can

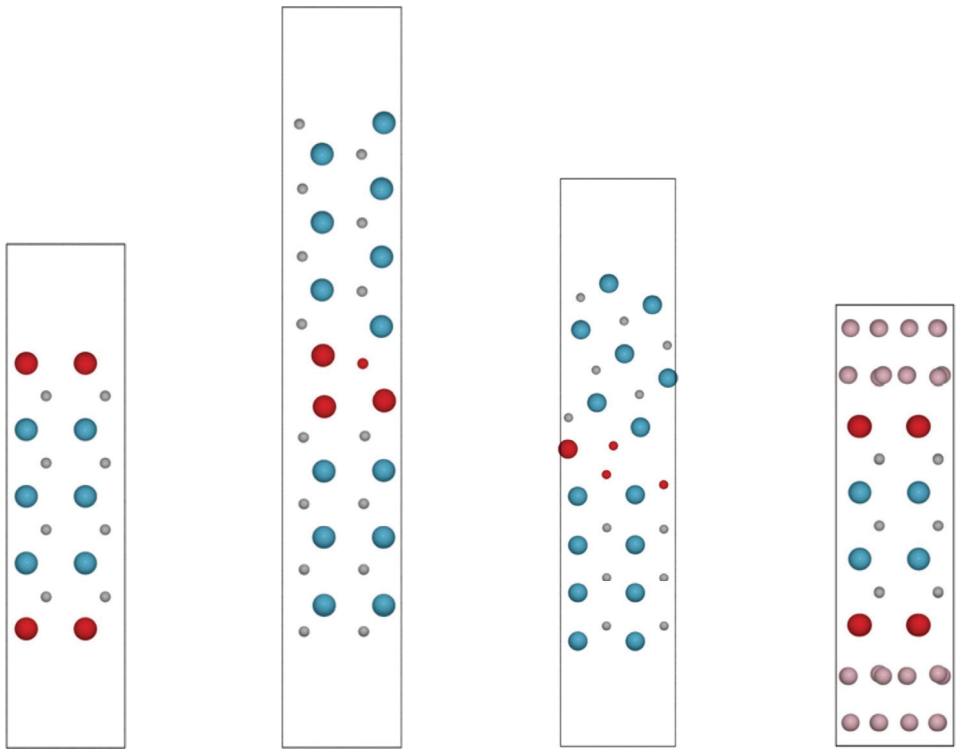

Figure 5.4: Substitutional sites at a (0001) WC surface (a), in a $\Sigma = 2_1$ grain boundary (b), in a $\Sigma = 4_1$ grain boundary (c), and in a (0001)||(111) phase boundary (d) [73]. Large cyan coloured atoms are W, small grey atoms are C, medium sized pink atoms are binder phase atoms, and the red atoms mark the substitutional sites. These are the actual simulation cells used in Paper I.

also be constructed. Further, W atoms can be switched to other metal atoms, such as Ti, to get a general γ-MC film structure. Using this construction, the γ-MC phase will generally be strained in the (111) plane such that the M and C layers along [111] matches the corresponding layers in δ-WC. Further, the thickness of the slab may be varied, however, since the films consist of thermodynamically unstable phases, only the formation of very thin films are possible. Further, for the calculations to be feasible small repeating unit cells are required. Therefore, the Co slab is oriented such that there is a 30° angle between δ-WC $[2\bar{1}\bar{1}0]$ and Co $[\bar{1}10]$. This gives a unit cell with 4 Co atoms and 3 W or C atoms in each atomic layer along the [111] and [0001] directions, respectively. Furthermore, this also gives a low strain in the Co phase when it is matched with WC.

In Papers V and VI we follow the procedure outlined in Ref. [135], but instead of the first three we allow the first four layers (two C and two W) to deviate from the hexagonal stacking sequence. This results in eight unique thin film stacking sequences which

are illustrated in Fig. 5.5 together with atomistic configuration for the k_1 stacking. In the figure, ml_i and cl_i denote the i:th metal and carbon layer counting from the Cobalt, respectively. The k_0 stacking is simply the δ-WC(0001) in contact with Co(111).

From Fig. 5.5 we note that the transition from hexagonal to cubic stacking are the same for some different stackings, e.g. the k_8 stacking is the same as the k_1 stacking with two added cubic atomic layers at the interface towards Co. Similarly extending k_2 yields k_4. Additionally, we note that for stackings k_1, k_2, k_4 and k_8 the hexagnoal and cubic regions overlap, while for the others the two regions connect at the interface or are separated by one atomic layer. In the later four there is always an additional hexagonal stacking different from $ABABAB\ldots$ that extend into both the hexagonal and cubic regions, giving rise to an additional hexagonal/hexagonal interface. The results of Papers V and VI indicate that these stackings are unfavourable compared to k_1, k_2, k_4 and k_8.

The stoichoimetry of γ-WC, stable only above 2800 K, is ranging from stoichiometric down to a C/W ratio of around 0.5 [60]. Further, in undoped WC–Co cemented carbides thin cubic WC films are observed more frequently in W-rich conditions compared with C-rich conditions. This suggest that the films also contain vacancies which are more favourable in W-rich conditions compared with C-rich conditions. Carbon vacancies will, therefore, be consider in the first two carbon layers (counted from the Co interface) for the model thin film systems. Since it is strongly unfavourable to introduce vacancies in the hexagonal structure, no vacancies will be considered in the purely hexagonal stacking, k_0. For more information regarding these stackings the reader is referred to Papers V and VI.

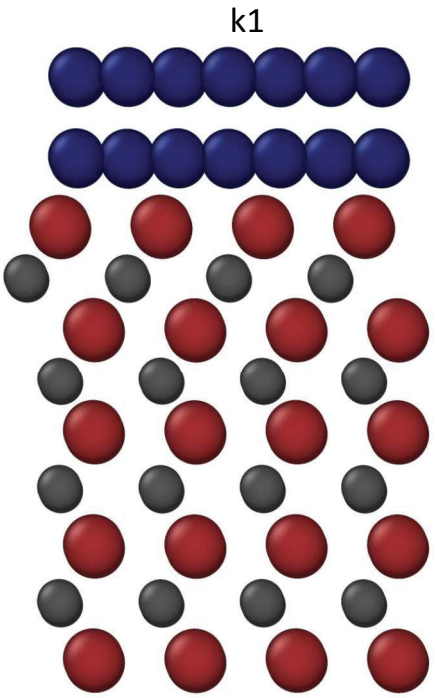

	k0	k1	k2	k3	k4	k5	k6	k7	k8
	Co	Co	Co	Co	Co	Co	Co	Co	Co
ml_1	A	B	C	A	B	B	C	A	C
cl_1	B	C	B	B	A	C	B	C	A
ml_2	A	A	A	C	C	A	A	B	B
cl_2	B	B	B	B	B	C	C	C	C
ml_3	A	A	A	A	A	A	A	A	A
	B	B	B	B	B	B	B	B	B
	A	A	A	A	A	A	A	A	A
	B	B	B	B	B	B	B	B	B
	A	A	A	A	A	A	A	A	A

Cubic stacking Hexagonal stacking

Figure 5.5: Graphical illustration of the nine different stackings from Paper V. In the left figure the atomic configuration of the k_1 stacking is illustrated and in the right table the stacking sequences for the various ks and as well as which layers follows the hexagonal stacking (red) and the cubic stacking (blue) are indicated. The i:th metal layer is denoted ml_i (counting from the top) and similarly the carbon layers are denoted cl_i.

6

Computational methods

”Atoms are very special: they like certain particular partners, certain particular directions, and so on. It is the job of physics to analyze why each one wants what it wants.”

– Richard P. Feynman [136]

In this chapter the computational methods used in this thesis are reviewed. This includes atomistic descriptions such as DFT and inter-atomic potentials, simulation techniques such as MD and free energy methods.

6.1 Atomic interactions

The core of all computations at the atomic level is the description of the atomic interactions in the system. In a system of interacting, non-relativistic particles, all properties are in principle determined by its many-body state $|\Phi(t)\rangle$, which is obtained as a solution to the time-dependent Schrödinger equation

$$i\hbar\frac{\partial}{\partial t}|\Phi(t)\rangle = H|\Phi(t)\rangle, \tag{6.1}$$

where H is the Hamilton operator of the system. The allowed energies, E, in the system are defined by the time-independent Schrödinger equation

$$H|\Psi\rangle = E|\Psi\rangle, \tag{6.2}$$

where the eigenstates, $|\Psi\rangle$, forms an orthogonal basis from which any arbitrary many-body state may be expressed. However, for many applications, including the work in

this thesis, knowing the ground state of the system, i.e., the lowest eigenvalue E^0 of H and its associated eigenstate $|\Psi^0\rangle$, is sufficient.

In this thesis we will use the electronic structure description where the systems consist of interacting electrons and nuclei. For such a system the Hamiltonian operator, H, is the sum of the kinetic energy and potential energy due to Coulomb interaction[137]

$$H = T_e(\{\boldsymbol{r}\}) + T_N(\{\boldsymbol{R}\}) + V_{ee}(\{\boldsymbol{r}\}) + V_{eN}(\{\boldsymbol{r}\},\{\boldsymbol{R}\}) + V_{NN}(\{\boldsymbol{R}\}), \tag{6.3}$$

where, T_e and T_N are the kinetic energy operators for the electrons and nuclei respectively, and V_{ee}, V_{eN}, and V_{NN} represent potential energies from electron-electron, electron-nucleus, and nucleus-nucleus interactions, respectively. Here, $\{\boldsymbol{r}\}$ denotes the set of electron positions, including spin degrees of freedom and $\{\boldsymbol{R}\}$ denotes the set of all ionic coordinates.

It turns out that an exact analytical solution of the Schrödinger equation for the electronic structure Hamiltonian is essentially only possible for very simple systems, such as a the hydrogen atom. However, for more complex systems, even the helium atom, we rely on approximations and numerical solutions. Those approximation methods that result in equations free from adjustable physical parameters are referred to as ab-initio or first-principles methods.

6.1.1 The Born-Oppenheimer approximation

The first approximation that usually is made when solving Eq. (6.2) for the Hamiltonian in Eq. (6.3) is the so-called Born-Oppenheimer approximation [138], which uses the fact that the nuclei are much heavier than the electrons. For the electrons, this difference in mass means that they see the nuclei as charges frozen in their instantaneous location, and hence, the nuclear kinetic energy term, T_N, can be dropped and the ion-ion repulsion, V_{NN}, regarded as a constant shift in energy, E_{NN}. On the other hand, the nuclei can be regarded as moving in a mean-field generated by the electrons. Hence, the problem has now been separated into two problems: an electronic structure problem where the nuclei are considered to be fixed, and a nuclear problem, which generally can be treated classically.

The Hamiltonian for the electron problem may be written as

$$H_e = T_e(\{\boldsymbol{r}\}) + V_{ee}(\{\boldsymbol{r}\}) + V_{ext}(\{\boldsymbol{r}\},\{\boldsymbol{R}\}), \tag{6.4}$$

where $V_{ext}(\{\boldsymbol{r}\},\{\boldsymbol{R}\}) = V_{eN}(\{\boldsymbol{r}\},\{\boldsymbol{R}\})$ is the external potential from the fixed nuclei. Further, the time-independent Schrödinger equation for the electrons becomes

$$E_e(\{\boldsymbol{R}\})|\Psi_e(\{\boldsymbol{r}\},\{\boldsymbol{R}\})\rangle = H_e|\Psi_e(\{\boldsymbol{r}\},\{\boldsymbol{R}\})\rangle, \tag{6.5}$$

hence, the ground state energy $E_0(\{\boldsymbol{R}\}) = E_{0,e}(\{\boldsymbol{R}\}) + E_{NN}(\{\boldsymbol{R}\})$ will depend parametrically on the positions of the ions. $E_0(\{\boldsymbol{R}\})$ is known as the Born–Oppenheimer potential energy surface and, in many cases, it is an excellent approximation[137].

Now, if we treat the nuclei as classical particles moving in the electronic mean-field, i.e. the Born–Oppenheimer potential energy surface, the force on each nucleus is given as $\boldsymbol{F}_I = \partial E_0(\{\boldsymbol{R}\})/\partial \boldsymbol{R}_I$. Further, using the Hellmann-Feynman theorem, this can be rewritten as

$$\boldsymbol{F}_I = -\frac{\partial E_0(\{\boldsymbol{R}\})}{\partial \boldsymbol{R}_I} = -\left\langle \Psi_\mathrm{e} \left| \frac{\partial H_\mathrm{e}}{\partial \boldsymbol{R}_I} \right| \Psi_\mathrm{e} \right\rangle. \tag{6.6}$$

This equality requires that $|\Psi_\mathrm{e}\rangle$ is a complete basis. Differentiating H_e, Eq. (6.5), with respect to $\boldsymbol{R}_I$ shows that the forces on the ions are simply the electrostatic forces from the electronic charge distribution (or density), $n(\boldsymbol{r})$, defined in Eq. (6.7).

The original quantum mechanical electron structure problem has now been greatly simplified. In principle, the ground state of a system could be found by starting from an initial set of ionic positions and then find ground the state electron wave function, and hence also the ground state electron density, for the given set of ionic positions. Thereafter, the ions can be moved according to their forces using e.g. the conjugate gradient method. Then, the new ground the state electron wave function and ionic forces may be found. This process is repeated until forces are below some reasonably small value. However, to numerically solve the electron problem, Eq. (6.5), further theoretical development is required.

6.1.2 Density functional theory (DFT)

The density functional theory (DFT) method is one of the most efficient and popular first-principles tools to solve the electron structure problem. It makes calculations of systems involving several hundreds of atoms tractable on modern supercomputers. Formally, DFT is an exact theory, however, it does use the many-body electron wavefunction $\Psi_\mathrm{e}(\{\boldsymbol{r}\}, \{\boldsymbol{R}\})$, which has $3N$ variables for a system of N atoms, as the basic variable. Instead, as the name suggest, it uses the much simpler electron density $n(\boldsymbol{r})$, which has only 3 variables, as the basic variable. The electron density is defined from $\Psi_\mathrm{e}(\{\boldsymbol{r}\}, \{\boldsymbol{R}\})$ according to

$$n(\boldsymbol{r}) = \int \mathrm{d}\boldsymbol{r}_2 \ldots \mathrm{d}\boldsymbol{r}_N \, |\Psi_\mathrm{e}(\boldsymbol{r}, \boldsymbol{r}_2, \ldots, \boldsymbol{r}_N)|^2, \tag{6.7}$$

where the parametric dependence on the nuclear ionic positions has been dropped

The exactness of the DFT was proven by Hohenberg and Kohn[139] using two theorems:

1. The ground state electron density, $n_0(\boldsymbol{r})$, uniquely determines the external potential, thus fixing the electronic Hamiltonian in Eq.(6.4). Consequently, $n(\boldsymbol{r})$ is sufficient to, in principle, determine all properties of the system.

2. There exist a universal energy functional of the electron density, $E[n(\boldsymbol{r})]$, such that the density that gives a minimum, $n_0(\boldsymbol{r})$, is the exact ground state density and the ground state energy is given by $E_0 = E[n_0(\boldsymbol{r})]$.

However, no way of finding this universal energy functional was presented.

In 1965, Kohn and Sham[140] developed a practical way of approaching DFT by replacing the problem of interacting electrons in an external potential with an auxiliary problem of fictitious non-interacting electrons in an effective potential with the same ground state energy and density. Although, the existence of this auxiliary system, commonly known as the Kohn-Sham auxiliary system, has not been proven for the general case, Kohn-Sham theory has had remarkable success in predicting many material properties, which justifies the theory[137].

Since the electrons in the Kohn-Sham system are non-interacting the many-body wave-function can be replaced by single particle Kohn-Sham orbitals, $\psi_i(\boldsymbol{r})$, which are the solutions to Schrödinger-like equations with the Kohn-Sham Hamiltonian, H_{KS}, given by

$$\underbrace{\left[-\frac{1}{2}\nabla^2 + V_{\mathrm{KS}}(\boldsymbol{r})\right]}_{H_{\mathrm{KS}}}\psi_i(\boldsymbol{r}) = \epsilon_i\psi_i(\boldsymbol{r}), \tag{6.8}$$

where $V_{\mathrm{KS}}(\boldsymbol{r})$ is the effective Kohn-Sham potential and ϵ_i are the energy eigenvalues of the Kohn-Sham orbitals. The subscript "e" indicating electron wave-functions has here been dropped from ψ for convenience. The density will be given as the sum over the density from each orbital, i.e. $n(\boldsymbol{r}) = \sum_i f_i |\psi_i|^2$, where f_i are the occupations of orbital i.

The Kohn-Sham energy functional, $E_{\mathrm{KS}}[n]$, is written as[140]

$$E_{\mathrm{KS}}[n] = T_{\mathrm{s}} + E_{\mathrm{H}}[n] + \int \mathrm{d}\boldsymbol{r} V_{\mathrm{ext}}(\boldsymbol{r}) + E_{\mathrm{xc}}[n], \tag{6.9}$$

where T_{s} is the kinetic energy of the non-interacting fictitious particles given by

$$T_{\mathrm{s}} = \frac{1}{2}\sum_i |\nabla\Psi_i(\boldsymbol{r})|^2. \tag{6.10}$$

Further, $E_{\mathrm{H}}[n]$ is the Hartree energy which represents the mean-field electron-electron interaction, hence, given by

$$E_{\mathrm{H}}[n] = \frac{1}{2}\int \mathrm{d}\boldsymbol{r}\mathrm{d}\boldsymbol{r}' \frac{n(\boldsymbol{r})n(\boldsymbol{r}')}{|\boldsymbol{r}-\boldsymbol{r}'|}. \tag{6.11}$$

$V_{\mathrm{ext}}(\boldsymbol{r})$, is the single particle version of $V_{\mathrm{ext}}(\{\boldsymbol{r}\},\{\boldsymbol{R}\})$ as defined in Eq.(6.4). Moreover, $E_{\mathrm{xc}}[n]$ is an additional term containing the remaining many-body effects, such that

the ground state density of the Kohn-Sham system will be equal to that of the original interacting system, hence strictly defined as $E_{\mathrm{xc}}[n] = T_{\mathrm{e}} + V_{\mathrm{ee}} - [T_{\mathrm{s}} + E_{\mathrm{H}}[n]]$. These many-body effects includes exchange and correlation effects as well as possible errors in the kinetic energy of the electrons. $E_{\mathrm{xc}}[n]$ is, therefore, called the exchange-correlation functional.

A variation of Eq. (6.9) with respect to the single particle wave-functions, $\psi_i(\boldsymbol{r})$, subject to the constraint of constant number of electrons N, i.e., $N = \int \mathrm{d}\boldsymbol{r} n(\boldsymbol{r})$, gives Eq. (6.8) with

$$V_{\mathrm{KS}}(\boldsymbol{r}) = \int \mathrm{d}\boldsymbol{r}' \frac{n(\boldsymbol{r}')}{|\boldsymbol{r} - \boldsymbol{r}'|} + V_{\mathrm{ext}}(\boldsymbol{r}) + \frac{\delta E_{\mathrm{xc}}[n]}{\delta n}. \tag{6.12}$$

Further, the energy total energy of the system is given by

$$E = \sum_i f_i \epsilon_i - V_{\mathrm{H}}[n] + E_{\mathrm{xc}}[n] - \int \mathrm{d}\boldsymbol{r} \frac{\delta E_{\mathrm{xc}}[n(\boldsymbol{r})]}{\delta n(\boldsymbol{r})} n(\boldsymbol{r}) \tag{6.13}$$

Now, the Kohn-Sham Hamiltonian, H_{KS}, depends on the electron density from the single particle wave-functions, $n(\boldsymbol{r}) = \sum f_i |\psi_i|^2$, which are the solutions to Eq. (6.8). Hence, it is nonlinear, and Eq. (6.8) may be solved numerically in a self-consistent manner, where an initial guess for the density is made and then the solution is iterated until convergence is reached.

6.1.2.1 Exchange-correlation functionals

If exact expression for all terms in Eq. (6.12) are known, then the ground state energy from Eq. (6.13) is exact. This is, however, not the case for $\frac{\delta E_{\mathrm{xc}}[n]}{\delta n}$ since this term includes many-body effects. Hence, this term must be approximated. One of the strengths of DFT is that even with very simple approximations of the exchange-correlation functional the calculations can be very accurate.

The simplest approach of approximating $E_{\mathrm{xc}}[n]$ is to let it depend locally on the electron density

$$E_{\mathrm{xc}}[n] = \int \mathrm{d}\boldsymbol{r} n(\boldsymbol{r}) \epsilon_{\mathrm{xc}}\left(n(\boldsymbol{r})\right), \tag{6.14}$$

where $\epsilon_{\mathrm{xc}}\left(n(\boldsymbol{r})\right)$ is the exchange-correlation energy of a homogeneous electron gas. This approach was introduced already by Kohn and Sham[140] and is known as the *local density approximation* or LDA.

LDA may be improved by taking into account the inhomogeneous electron density found in real material. In the *generalized gradient approximation* (GGA) not only the local density but also semi-local gradients of the density is included in ϵ_{xc}. However, there is no known systematic way of improving LDA by including higher order terms and development often relies heavily on physical intuition where one tries to satisfy

certain properties and trial and error. Hence, many different flavours of GGA exchange-correlation functionals exists [141, 142, 143, 144, 145]. The the most popular GGA functional in materials science was developed by Perdew, Burke and Ernzerhof[143] and, hence, referred to as PBE. The PBE functional has been used extensively in this thesis.

A major shortcoming of these local or semi-local exchange-correlation functionals is that they do not account for dispersive interactions, which are inherently non-local and connect the electron density at different points in space. One method to account for the dispersive interactions, known as the van der Waals density functional (vdW-DF) framework, is to expand the exchange-correlation of previous functionals by a non-local correlation functional that couples the density at different points in space through a kernel that contains information about how strongly two density regions interact depending on their spatial separation and the asymmetry of their response. Again, there are many different flavours of vdW-DF functionals [146, 147, 148]. In this thesis some calculations have been done using the vdW-DF-cx functional[148].

6.1.2.2 Implementing DFT numerically

So far, we have simplified the original quantum mechanical electron structure problem significantly, however, there are still a few more obstacles to address in order to make a practical numerical implementation of DFT.

For instance, a basis for the Kohn-Sham orbitals (or wave-functions), $\psi_i(\boldsymbol{r})$, is needed. When studying solids, periodic boundary conditions are often a demand, and in that case, a plane wave basis set is convenient. For a periodic simulation cell the potential is also periodic, hence Bloch's theorem[149] holds and if we drop the orbital index "i" a Kohn-Sham wave-function may be written as

$$\psi_{\boldsymbol{k}}(\boldsymbol{r}) = u_{\boldsymbol{k}}(\boldsymbol{r})e^{i\boldsymbol{k}\cdot\boldsymbol{r}} \tag{6.15}$$

where $\boldsymbol{k}$ is the wave vector. Further, the function $u_{\boldsymbol{k}}$ is periodic with the same periodicity as the simulation cell. Therefore, $u_{\boldsymbol{k}}$ can be expanded in a Fourier series of reciprocal lattice vectors $\boldsymbol{G}_j$ as

$$u_{\boldsymbol{k}}(\boldsymbol{r}) = \sum_j C_{\boldsymbol{k},j}(\boldsymbol{r})e^{i\boldsymbol{G}_j\cdot\boldsymbol{r}}. \tag{6.16}$$

Hence,

$$\psi_{\boldsymbol{k}}(\boldsymbol{r}) = \sum_j C_{\boldsymbol{k},j}(\boldsymbol{r})e^{i(\boldsymbol{k}+\boldsymbol{G}_j)\cdot\boldsymbol{r}}. \tag{6.17}$$

Moreover, the basis set may be truncated below a certain cut-off energy, E_{cutoff}, such that $\frac{1}{2}\left|\boldsymbol{k}+\boldsymbol{G}_j\right|^2 < E_{\text{cutoff}}$. Further, since the size of the basis set only depends on E_{cutoff} it is straightforward to do convergence of quantities with respect to the basis set by changing E_{cutoff}.

The major issue with plane wave expansions is that in the atomic core region the kinetic energy of the electrons is high and the wave function varies rapidly. Further, since the plane waves are delocalized, an extremely high number of plane waves would be required to accurately represent the electronic density in this core region. However, since only the outer valence electrons participate in the binding leaving the core states mostly unchanged, the core region need not be described as accurately as the rest of the system. The actual potential may, therefore, be replaced with a pseudopotential which yields the same wave function outside some core radius but has a much smoother variations within the core region. Then, the number of plane waves needed is significantly reduced. However, the pseudopotential is more complex compared with the original potential and it needs to be explicitly constructed for all atomic species involved and the size of the core region needs to be chosen appropriately. In all DFT calculations in this thesis, the projector-augmented wave (PAW)[150] method has been employed. In the PAW method the conversion between the valence and all-electron description is done using a linear transformation which allows for different levels of treatment with regards to the core electrons.

Introducing a periodic simulations cell generates an additional problem: many properties, such as the total energy of the system or the electron density, are now given as integrals over the first Brillouin zone (1BZ) of the system. This integral must be evaluated numerically which is most commonly done by replacing the integral with a sum over discrete points in the 1BZ. The simplest way to sample the 1BZ is to use a uniform grid and use symmetries that makes some k-points equivalent thus reducing the number of k -points needed. This method was introduced by Monkhorst and Pack[151] and has been used extensively throughout the thesis. Moreover, to calculate the properties, such as the ground state energy, a heaviside step function is used for the occupation of each band which includes only states up to the Fermi level. However, for conductors, such as metals, there is a finite electronic density of states (EDOS) at the Fermi level. Hence, the integral, which contains a product of the EDOS and the heaviside step function, is difficult to evaluate numerically and a very dense k-point grid is needed. The solution to this is to replace the heaviside step function with a smoother smearing function, i.e., introducing partial occupancies, which allows for a much coarser k-point grid. The integrals can then be extrapolated down to zero smearing. In this thesis the smearing method of Methfessel and Paxton[152] has been employed.

The integral over the 1BZ can also be done using the linear tetrahedron method in which the 1BZ is divided into tetrahedra. In these tetrahedra the function to be integrated is then interpolated linearly and the errors arising from the linear interpolation can be corrected for using Blöchl corrections[153]. This generates a much smoother EDOS compared with the Monkhorst-Pack[151] method. This method is, therefore, used when an accurate EDOS is needed, such as for the electronic free energy calculations in Paper IV.

In this thesis all DFT calculations have been done using the Vienna ab-initio simu-

lation package (VASP)[154, 155].

6.1.3 Inter-atomic potentials

As the size of the atomic system increases first principles calculations become unfeasible. It is, therefore, neccessary to introduce simplified interactions between atoms. A popular method is to develop analytical inter-atomic potentials to model the potential energy surface $E(\{\boldsymbol{r}\})$ semiemperically. Here, we use $\{\boldsymbol{r}\}$ to represent the set of atomic positions. The total potential energy of a system of N atoms can be divided into terms depending on the coordinates of individual atoms, pairs, triplets etc. [156] according to

$$E(\{\boldsymbol{r}\}) = \sum_{i}^{N} V_1(\boldsymbol{r}_i) + \sum_{i<j}^{N} V_2(\boldsymbol{r}_i, \boldsymbol{r}_j) + \sum_{i<j<k}^{N} V_3(\boldsymbol{r}_i, \boldsymbol{r}_j, \boldsymbol{r}_k) + \cdots . \tag{6.18}$$

Here, the first term is only meaningful if the system interacts with an external potential such as an electric field. If only the second term is used in the expansion one obtains the simplest type of analytical potential: the pair potential. The applicability of the pair potential is rather limited and it is most suitable for simple liquids such as liquid argon [157]. A popular example of a pair potential is the Lennard-Jones potential which was proposed already in 1924[158].

By introducing a functional of an intermediate quantity depending only on pairs the pair potential formalism can be significantly improved. These models are called pair functionals and the most common example is the embeddad atom model (EAM) where an embeddig energy representing the energy cost of placing an atom in the electron density from the other atoms was added to the pair energies [159, 160]. EAM has been used widely to describe metallic systems, however, it does not treat covalency and directional bonding, two important properties in hexagonal WC.

If functionals of higher order terms from (6.18) are included you end up with a cluster functional. A popular type of cluster functional is the analytical bond order potential (ABOP) [161, 162, 163, 164]. In the ABOP the potential energy of the system is written as:

$$E = \frac{1}{2} \sum_{i \neq j} f_C(r_{ij}) \left[V_R(r_{ij}) + \bar{b}_{ij} V_A(r_{ij}) \right], \tag{6.19}$$

where $f_C(r_{ij})$ is a continuous cut-off function that vanishes outside a certain cut-off radius and $V_R(r_{ij})$ and $V_A(r_{ij})$ are repulsive and attractive pair potentials of generalized Morse type, respectively. The highest order term is placed in $\bar{b}_{ij}$ which is a functional of a three body term, the bond order. This functional adjusts the strength of a bond depending on the number of neighbouring bonds and the corresponding bond angles. The ABOP is, therefore, suitable for modeling both Co and hexagonal WC. In Paper III an ABOP is fitted for the WC–Co system.

In this thesis all sampling with inter-atomic potentials is done using the Large-scale Atomic/Molecular Massively Parallel Simulator (LAMMPS)[165, 166].

6.1.4 Alloy cluster expansions

Alloy cluster expansion (CE) is a computationally efficient method to accurately calculate the energy for different microstates of an alloy system. Generally, DFT calculations are too expensive to be used directly to calculate the energy of all microstates need to find ground states and the configurational free energy of an alloy system. Therefore, alloy cluster expansion (CE) fitted to DFT data serves as a very useful complement to pure DFT calculations. It is, therefore, employed in Papers IV-VI.

Alloy CE are based on a fixed atomic lattice where a cluster is defined as a set of lattice points. Moreover, the number of lattice points in the cluster gives the order of the cluster. Further, a cluster of order 1, 2, 3 or 4 are referred to as a singlet, pair, triplet or quadruplet, respectively. In an A-B system, a cluster could be the nearest A-B neighbour pair, nearest neighbour A-A pair or some A-A-B triplet uniquely defined by its inter-atomic distances and angles. Moreover, the type of site, i.e. the Wyckoff position, for each atom in the cluster is also a discriminator. Hence, even if two A-A pairs have the same distance, their individual surroundings may make them belong to different clusters. Generally, the number of equivalent clusters increase with the cluster order since there, for example, are more possible combinations for a triplet compared to a pair.

To be able to enumerate the clusters it is convenient to define the radius or size of the cluster as the average distance of all the lattice points from the geometric center of the cluster. Further, a cut-off size or radius and a maximum order can be set to limit the number of clusters. Usually, cluster interactions become less important as the radius or order increases.

The energy of a CE is expressed as,

$$E(\boldsymbol{\sigma}) = J_0 + \sum_{\xi} \left\langle \Pi_{\xi'}(\boldsymbol{\sigma}) \right\rangle_{\xi} J_{\xi}, \tag{6.20}$$

where $\boldsymbol{\sigma}$ is the occupation vector, $\sum_{\xi}$ is a sum over all clusters, $\langle ... \rangle_{\xi}$ is an average over all clusters ξ' equivalent to cluster ξ and J_{ξ} are the effective cluster interactions (ECIs) of the model that needs to be found. In this thesis the ECIs are fitted to total energies from DFT using the program ICET[167].

Even though the cluster expansion acts on a perfect lattice it can still capture the contribution of relaxations of the atoms by mapping relaxed structures onto the perfect lattice. Lattice relaxations is an important contribution in systems with impurities such as vacancies.

Further, with the right choice of ECIs, a CE is able to represent any function of the configuration [168]. This means that it is possible to model free energy contributions such as vibrational free energy using a cluster expansion.

6.1.5 Force constant models

Force constant force constant (FC) models describes the vibrational motion of a system for a fixed occupation of the lattice. It is based on the Taylor expansion of the the potential energy, E, as a function of displacements, u, around some static positions r_0 with potential energy E_0:

$$E = E_0 + \Phi_i^{\alpha} u_i^{\alpha} + \Phi_{ij}^{\alpha\beta} u_i^{\alpha} u_j^{\beta} + \Phi_{ijk}^{\alpha\beta\gamma} u_i^{\alpha} u_j^{\beta} u_k^{\gamma} + \cdots . \tag{6.21}$$

Here, Φ are force constants and Latin and Greek indices enumerate atoms and Cartesian coordinates, respectively. Further, Einstein summation convention is implied. Conventionally, r_0 is chosen to be the ideal relaxed lattice which means that the first order term in the expansion is zero.

In the Taylor expansion above the force constants are the unknowns that need to be found. They are defined as derivatives of the potential energy with respect to the displacements, i.e., the second order force constants are defined as

$$\Phi_{ij}^{\alpha\beta} = \frac{\partial^2 E}{\partial u_i^{\alpha} \partial u_j^{\beta}} \tag{6.22}$$

and other orders defined analogously. Conventionally, force constants are obtained by a direct approach[169], where the derivatives are numerically computed by calculating forces for configurations with a single atom displaced from its ideal lattice position. The most common software to use for calculation of second-order force constants using the direct approach is Phonopy[169]. Furthermore, the direct approach works very well for high symmetry systems where the number of configurations for which forces are required is low. However, for low symmetry systems, e.g. systems with defects such as vacancies or interfaces, the number of configurations needed to be calculated quickly increases and becomes expensive with DFT. Another approach to extract accurate force constants is by regression which has the advantage of not requiring as many calculations as the direct approach[170, 171, 172, 173, 174, 175, 176]. The regression approach is implemented in the hiPhive software[177]. In the direct method the derivatives are calculated exactly, hence, only one atom is displaced in each configuration, meaning that the information in each configuration is small. However, in the regression method the whole problem is treated as an optimization problem where all atoms may be displaced, meaning more information in each configuration, hence the reduced number of configurations required.

Moreover, using the direct approach gives a FC model that represents the system at 0 K, however, with the regression approach it is possible to fit FC models from MD simulations (see Sec. 6.2) and thus effectively introducing a temperature dependence on the FC model. This is advantageous for studying systems that are dynamically unstable at low temperatures.

In Papers II and IV-VI FC models are constructed using either Phonopy[169] or hiPhive[177].

6.2 Molecular dynamics

Molecular dynamics is a simulations technique where a system is evolved in time according to the forces acting in the system to obtain a phase space trajectory, from which time averages can be obtained. It was first introduced by Alder in 1959 [178]. The force on atom i, $\boldsymbol{F}_i$, is obtained from the potential energy surface $E(\{\boldsymbol{r}\})$ as

$$\boldsymbol{F}_i = -\frac{\partial E(\{\boldsymbol{r}\})}{\partial \boldsymbol{r}_i}, \tag{6.23}$$

where $E(\{\boldsymbol{r}\})$ can be computed from a classical inter-atomic potential or an ab initio method such as DFT. The latter case is often referred to as ab-initio molecular dynamics (AIMD). It is a classical technique, i.e., it follows the laws of classical mechanics. The system can, therefore, be evolved in time by solving Newton's equations of motion. The classical mechanics approximation of the motion of the atoms and molecules is most cases accurate [179]. Only for light atoms or molecules, or for vibrational and rotational motion with high frequency is quantum mechanical effects relevant. The procedure of an MD simulation is similar to real experiments [180]. First, a sample is prepared, i.e. a model system is chosen. Then, the system is equilibrated, i.e, evolved until the properties of the system no longer change with time. When the system is equilibrated the actual measurement of the desired property can be performed.

There are a lot of different methods for integrating Newton's equations of motions giving rise to errors of different orders [179]. One of the simplest, but also usually the best, is the so-called velocity Verlet algorithm[181, 182]. It is time-reversible and preserves the area in phase-space and, as a result, has good energy conservation properties, without being more computationally expensive than the simple Euler method. In the velocity Verlet algorithm the positions, $\boldsymbol{r}_i$, and velocities, $\boldsymbol{v}_i$, are evolved from time t to time $t + \Delta t$, where Δt is the time step, according to the following scheme [183, 182]:

1. $\boldsymbol{r}_i(t + \Delta t) = \boldsymbol{r}_i(t) + \boldsymbol{v}_i(t)\Delta t + \frac{1}{2}\frac{\boldsymbol{F}_i(t)}{m_i}\Delta t^2$
2. Calculate new forces $\boldsymbol{F}_i(t + \Delta t)$ from the interaction potential using $\boldsymbol{r}_i(t + \Delta t)$
3. $\boldsymbol{v}(t + \Delta t) = \boldsymbol{v}(t) + \frac{1}{2}\left(\frac{\boldsymbol{F}_i(t)}{m_i} + \frac{\boldsymbol{F}_i(t+\Delta t)}{m_i}\right)$

Here, m_i is the mass of particle i. The error of the velocity Verlet algorithm is $\mathcal{O}(\Delta t^4)$ for the positions and $\mathcal{O}(\Delta t^2)$ for the velocities. Moreover, the size of the time step, Δt, has to be determined for each system, where the optimum value is a compromise as it should be large to sample as much of phase space as possible, but it has to be small enough to generate trajectories that produce accurate predictions.

As stated above, MD generates trajectories from which time averages may be calculated, while conventional statistical mechanics is not based on time averaging, but rather ensemble averages where one considers many realizations of the same system. An ensemble can be considered as a collection of systems (states) which are described by the same macroscopic interactions and share a set of macroscopic thermodynamic parameters. Ensemble averages can be simulated directly with the MC technique [184, 179]. However, unlike MD, MC gives no information on the dynamics of the system. The most fundamental ensemble is the microcanonical (NVE) ensemble, which represents an isolated N-particle system with constant energy, E, and constant volume, V. Now, if a system that is evolved under the same constraints and given an infinite amount of time, is able to visit all possible states it is said to be ergodic. Consequently, for ergodic systems the ensemble and time averages are equal. This is referred to as the *ergodic hypothesis*. The ergodic hypothesis is generally believed to be true for most systems, although in practice it may be problematic to access sufficiently many states during the simulation time.

6.2.1 Temperature, pressure and stress

In MD simulations the system is equilibrated given certain constraints on thermodynamic parameters which defines the type of ensemble that is being simulated. The NVE ensemble is achieved by just running the velocity Verlet algorithm as described above. Other common ensembles include the NVT and NPT ensembles, where the temperature, T, and pressure, P, are constant. In order to equilibrate to a certain pressure and temperature these thermodynamic parameters must first be measured.

6.2.1.1 Measurement

In an MD simulation the thermodynamic parameters must be expressed using properties, such as the positions $\boldsymbol{r}_i$, momenta $\boldsymbol{p}_i$, and forces $\boldsymbol{f}_i$ of the particles in the system. We first start by defining the Hamiltonian H of the system as

$$H = \sum_i \frac{\boldsymbol{p}_i^2}{2m_i} + U(\boldsymbol{r}_1, ..., \boldsymbol{r}_N), \tag{6.24}$$

where the first term is the kinetic energy, E_{kin}, and U is the potential energy of the system from the interaction potential.

Now, to measure the temperature it is convenient to use the equipartition of energy over all degrees of freedom that enter quadratically in the Hamiltonian of the system [185]. The equipartition of the kinetic energy is derived from the expectation value of the kinetic energy

$$\langle E_{\text{kin}} \rangle = \left\langle \sum_i \frac{\boldsymbol{p}_i^2}{2m_i} \right\rangle = \frac{\int \sum_i \frac{\boldsymbol{p}_i^2}{2m_i} \exp\left[-\frac{\sum_i \frac{\boldsymbol{p}_i^2}{2m_i} + U(\boldsymbol{r}_1, \ldots, \boldsymbol{r}_N)}{k_B T} \right] \mathrm{d}^{3N}\boldsymbol{p} \mathrm{d}^{3N}\boldsymbol{r}}{\int \exp\left[-\frac{\sum_i \frac{\boldsymbol{p}_i^2}{2m_i} + U(\boldsymbol{r}_1, \ldots, \boldsymbol{r}_N)}{k_B T} \right] \mathrm{d}^{3N}\boldsymbol{p} \mathrm{d}^{3N}\boldsymbol{r}}, \tag{6.25}$$

where i is taken over all particles and the integrals are taken over all positions and momenta. The integrals over the positions cancel and the integral over each of the three momentum dimensions will be equal. Moreover, the integrals over the particles are also identical. The expectation of the kinetic energy can, therefore, be simplified and expressed as

$$\langle E_{\text{kin}} \rangle = 3N \frac{\int \frac{p^2}{2m} \exp\left[-\frac{p^2}{2mk_B T} \right] \mathrm{d}p}{\int \exp\left[-\frac{p^2}{2mk_B T} \right] \mathrm{d}p} = \frac{3Nk_B T}{2}. \tag{6.26}$$

Hence, the kinetic energy of each degree of freedom is $\frac{k_B T}{2}$ and the temperature may be expressed as

$$T = \frac{2\langle E_{\text{kin}} \rangle}{3Nk_B}. \tag{6.27}$$

In MD simulations the total momentum is often set to zero to avoid drift which means that there are 3 less degrees of freedom. The temperature is then given by

$$T = \frac{2\langle E_{\text{kin}} \rangle}{3(N-1)k_B}. \tag{6.28}$$

The most common way to meassure pressure is based on the virial equation for the pressure [185]. The pressure at constant temperature and constant number of particles can be expressed from the partition function using the following thermodynamic relation

$$P = k_B T \frac{1}{Q_{NVT}^{ex}} \frac{\partial Q_{NVT}^{ex}}{\partial V}, \tag{6.29}$$

where Q^{ex}_{NVT} is the excess part of the partition function in the canonical (NVT) ensemble for identical particles, Q_{NVT} [156]. Further, Q_{NVT} is defined as

$$\begin{aligned} Q_{NVT} &= \frac{1}{N!}\int \frac{\mathrm{d}^{3N}\boldsymbol{r}\mathrm{d}^{3N}\boldsymbol{p}}{h^{3N}} \exp\left[-\frac{H}{k_B T}\right] = \\ &= \underbrace{\frac{1}{N!}\int \frac{\mathrm{d}^{3N}\boldsymbol{p}}{h^{3N}} \exp\left[-\frac{\sum_i \frac{\boldsymbol{p}_i^2}{2m_i}}{k_B T}\right]}_{Q^{\mathrm{id}}_{NVT}} \underbrace{\int \mathrm{d}^{3N}\boldsymbol{r} \exp\left[-\frac{U(\boldsymbol{r}_1,...,\boldsymbol{r}_N)}{k_B T}\right]}_{Q^{\mathrm{ex}}_{NVT}}, \end{aligned} \tag{6.30}$$

where, Q^{id}_{NVT} is the kinetic (ideal gas) part of Q_{NVT}.

Moreover, to calculate the volume dependence of Q^{ex}_{NVT} it is convenient to work in dimensionless coordinates

$$\mathbf{r}_i = V^{\frac{1}{3}}\mathbf{s}_i. \tag{6.31}$$

Then, Q^{ex}_{NVT} may be written as

$$Q^{ex}_{NVT} = V^N \int \exp\left[-\frac{U\left(V^{\frac{1}{3}}\mathbf{s}_1,...,V^{\frac{1}{3}}\mathbf{s}_N\right)}{k_B T}\right] \mathrm{d}^{3N}s. \tag{6.32}$$

Now, derivation with respect to V gives

$$\frac{\partial Q^{ex}_{NVT}}{\partial V} = \frac{N Q^{ex}_{NVT}}{V} - \frac{V^{N-\frac{2}{3}}}{3k_B T}\int \sum_i \mathbf{s}_i \nabla_i U \exp\left[-\frac{U\left(V^{\frac{1}{3}}\mathbf{s}_1,...,V^{\frac{1}{3}}\mathbf{s}_N\right)}{k_B T}\right] \mathrm{d}^{3N}s. \tag{6.33}$$

Finally, combining this with equation (6.29) and using the definition of expectation values gives

$$P = \frac{N k_B T}{V} - \frac{1}{3V}\left\langle \sum_i \mathbf{r}_i \frac{\partial U}{\partial \mathbf{r}_i}\right\rangle. \tag{6.34}$$

This is the virial theorem for pressure.

The expression for pressure can also be generalized to give the expression for the stress tensor $\sigma_{\alpha\beta}$ as

$$\sigma_{\alpha\beta} = -\frac{1}{V}\sum_i \left\langle \frac{p_i^\alpha p_i^\beta}{m_i} - \frac{\partial U}{\partial r_i^\alpha} r_i^\beta \right\rangle, \tag{6.35}$$

where α and β refer to the cartesian directions x, y, or z [186]. From this follows that

$$P = -\frac{\sigma_{xx} + \sigma_{yy} + \sigma_{zz}}{3}, \tag{6.36}$$

i.e. one third of the trace of the stress is equal to the negative pressure.

6.2.1.2 Thermostat and barostat

Methods of controlling the values of temperature and pressure are referred to as thermostats and barostats, respectively. From Eqs (6.28) and (6.34) it is straightforward to see that controlling the velocities of the particles and simulation cell (volume) will have the effect of controlling the temperature and pressure of the system, respectively. The simplest thermostat and barostat is to simply rescale the velocities and simulation cell in each time-step with a factor that restores the systems towards equilibrium values T_{eq} and P_{eq}. For example, to equilibrate temperature the velocities may be scaled with the factor $\alpha(t)$ according to

$$\alpha(t) = 1 + \frac{\Delta t}{\tau_T} \frac{T_{\text{eq}} - T(t)}{T(t)} \tag{6.37}$$

where $T(t)$ is the instantaneous temperature and τ_T a relaxation time that controls the how fast the system will equilibrate. This is method was introduced by Berendsen *et al.*[187].

Rescaling the velocities and simulation cell will only give ensembles that have the correct averages for properties that only depend on the positions of the particles. Better methods are generally needed to sample properties in the NVT and NPT ensembles. One very popular method was presented by Nosé[188] and Hoover[189], commonly referred to as Nosé-Hoover thermostat or barostat. The main idea is to add additional coordinates to the Lagrangian of the system which will act as fictive particles which interacts with the other particles. To control the temperature these additional coordinates are coupled to the particles velocities, while to control the pressure the additional parameters are coupled to the positions of the particles of the system.

In this thesis both the Berendsen and Nosé-Hoover mehods are used for equilibration. The former is used only in Paper III, while the latter is used in Papers II-IV.

6.3 Free energy methods

In this section several different numerical methods for calculating either absolute free energies or changes in free energies of atomic systems will be presented. These methods can also be used to calculate interface and surface free energies by using Eq. (4.6). Moreover, there is a special case with the liquid surface free energy, σ, which numerically equals the surface tension, τ[124], as was presented in Sec. 4.4. Further, since τ fluctuates heavily for atomic systems, σ must be calculated as an time average of the τ.

First, thermodynamic integration, a method to compute the full free energy, will be presented. Then, methods to compute partial contributions, such as configurational or vibrational, to the free energy will be presented.

6.3.1 Thermodynamic integration

In both experiments and simulations free energies can, generally, not be calculated directly since they are not simply averages of functions of the phase space of the system[179]. For example, Helmholtz free energy is directly related to the canonical partition function, i.e., $F = -k_{\mathrm{B}}T \ln(Q_{\mathrm{NVT}})$. Hence, free energies are related to the area in phase space that is accessible to the system. However, derivatives of the free energy can be measured in both experiments and simulations. This could for example be the pressure which is the derivative with respect to volume,

$$P = -\left(\frac{\partial F}{\partial V}\right)\Big|_{N,T}, \tag{6.38}$$

or the temperature which is the derivative with respect to entropy, S

$$T = \left(\frac{\partial F}{\partial S}\right)\Big|_{N,V}, \tag{6.39}$$

or the chemical potential, μ, given by

$$\mu = -\left(\frac{\partial G}{\partial N}\right)\Big|_{P,T}, \tag{6.40}$$

or the total internal energy U given by

$$U = -\left(\frac{\partial F/T}{\partial 1/T}\right)\Big|_{N,V}. \tag{6.41}$$

Further, changes in free energies can be calculated by integrating the free energy derivatives along reversible paths, i.e., thermodynamic integration.

By integrating Eq. (6.41) the free energy difference of a system at two temperatures,T_1 and T_2, may be found from the following relation[190]

$$\frac{F(T_2)}{T_2} - \frac{F(T_1)}{T_1} = -\int_{T_1}^{T_2} \frac{\mathrm{d}T}{T^2} \langle U \rangle, \tag{6.42}$$

where $\langle ... \rangle$ indicates an ensemble average. However, because of the ergodicity hypothesis (see Sec. 6.2), the average can also be a time average which can be achieved from MD simulations. This technique is commonly known as temperature integration.

In simulations we are not limited to physical thermodynamic integration paths that also can be followed in experiments[179]. Instead, we may use any parameter in the Hamiltonian of the system. Now, suppose we want to find the free energy difference between the two systems A and B described by Hamiltonians H_A and H_B, respectively. First, let us introduce a new Hamiltonian, H, according to

$$H(\lambda) = g_A(\lambda)H_A + g_B(\lambda)H_B, \tag{6.43}$$

where λ is an external switching (or coupling) parameter and $g_A(\lambda)$ and $g_B(\lambda)$ are switching functions. The switching functions must only satisfy the following conditions: $g_A(0) = g_B(1) = 1$ and $g_A(1) = g_B(0) = 0$, so that $H(0) = H_A$ and $H(1) = H_B$. Now, the free energy difference, i.e. $\Delta F_{A\to B} = F_B - F_A$, can be found by integrating H from $\lambda = 0$ to $\lambda = 1$ according to

$$\Delta F_{A\to B} = \int_A^B \left\langle \frac{\partial H}{\partial \lambda} \right\rangle. \tag{6.44}$$

This coupling parameter method was introduced by Kirkwood already in 1935[191] and is commonly refereed to as λ-integration. To find the absolute free energy of the system one of the endpoints of the integration need to be a state of known free energy, such as the ideal gas at high temperatures or an harmonic crystal at low temperatures.

Since there is a lot of freedom in the choice of switching functions we may not only switch between different atomistic descriptions but also calculate the work done by external forces on the system. In this case λ-integration is equivalent to integrating the mean force. For example, in Paper II we spatially join and separate two WC and Co crystals to calculate the work of adhesion for WC/Co phase boundaries.

6.3.2 Partial Free energy methods

In this section we focus on the calculation of partial contributions to Helmholtz free energies, $F = U - TS$, where U is the internal energy and S the entropy. On the atomic scale the free energy has several different contributions such as atomic vibrations or atomic configurations. It is often convenient to assume that the contributions are independent which allows for decomposition of F. In this thesis we primarily use the following decomposition of the free energy for solid phases:

$$F(T) = E_0 + F_{\text{el}}(T) + F_{\text{vib}}(T) + F_{\text{conf}}(T), \tag{6.45}$$

where E_0 is the relaxed total energy from an electronic structure calculation and $F_{\text{el}}(T)$, $F_{\text{vib}}(T)$ and $F_{\text{conf}}(T)$ are the temperature dependent free energy contributions from excitations of electrons, motion of atoms, and changing atomic configurations, respectively. Further, for a system described by an inter-atomic potential, E_0 is just the potential energy and $F_{\text{el}}(T) = 0$ since electrons are not included in the model. Here, follows computational methods to calculate the various free energy contributions in Eq. (6.45).

6.3.2.1 Electronic free energy

As stated above, the electronic contribution to the free energy, $F_{\text{el}}(T)$, arises from electrons being excited from their ground states. At not too high temperatures and assuming the free-electron gas model the free energy can be approximated by the Sommerfeld

expression[192]

$$F^{\mathrm{el}}(T) = -\frac{\pi^2}{6} n_{\mathrm{el}}(\varepsilon_{\mathrm{F}}) k_{\mathrm{B}}^2 T^2, \tag{6.46}$$

where $n_{\mathrm{el}}(\varepsilon_{\mathrm{F}})$ is the electronic density of states (EDOS) at the Fermi-energy, i.e., the electron chemical potential, μ_{el}, at T=0. For more accurate and reliable electronic free energies at higher temperatures we consider the electronic entropy $S_{\mathrm{el}}(T)$, which can be computed from the EDOS as[193]

$$S^{\mathrm{el}}(T) = -k_{\mathrm{B}} \int n_{\mathrm{el}}(\epsilon)\{f(\epsilon)\ln[f(\epsilon)]+[1-f(\epsilon)]\ln[1-f(\epsilon)]\}\mathrm{d}\epsilon, \tag{6.47}$$

where $f(\epsilon)$ is the Fermi distribution given by

$$f(\epsilon) = \frac{1}{e^{\beta(\epsilon-\mu^{\mathrm{el}}(T))}+1}, \tag{6.48}$$

where $\beta = (k_{\mathrm{B}}T)^{-1}$. Further, $\mu^{\mathrm{el}}(T)$ is computed from the condition of conserved number of valence electrons $N_{\mathrm{val}}^{\mathrm{el}}$

$$N_{\mathrm{val}}^{\mathrm{el}} = \int \mathrm{d}\epsilon\, n_{\mathrm{el}}(\epsilon) f(\epsilon). \tag{6.49}$$

Finally, by using the thermodynamic relation

$$\left(\frac{\partial U^{\mathrm{el}}}{\partial T}\right)_{\mathrm{V}} = T\left(\frac{\partial S^{\mathrm{el}}}{\partial T}\right)_{\mathrm{V}} \tag{6.50}$$

the free energy $F^{\mathrm{el}}(T) = U^{\mathrm{el}}(T) - TS^{\mathrm{el}}(T)$ can be written as

$$F^{\mathrm{el}}(T) = \int_0^T T' \frac{\partial S^{\mathrm{el}}(T')}{\partial T'}\mathrm{d}T' - TS^{\mathrm{el}}(T). \tag{6.51}$$

6.3.2.2 Vibrational free energy

The vibrational contribution to the free energy $F_{\mathrm{vib}}(T)$ arises from the atoms vibrating around a set of fixed lattice points. Further, at low temperatures many materials has highly harmonic lattice vibrations. It is, therefore, reasonable to start by investigating the vibrational free energy of a harmonic system.

In an harmonic system the potential energy is completely determined by a second-order FC model as described in Sec. 6.1.5, i.e., the system obeys Eq. (6.21) truncated after the second-order terms:

$$E = E_0 + \Phi_{ij}^{\alpha\beta} u_i^{\alpha} u_j^{\beta} \tag{6.52}$$

Further, the vibrational frequencies ω can be calculated from the force constants $\Phi_{ij}^{\alpha\beta}$. In a harmonic system all free energy is associated to vibrations (or phonons) and the free energy is described by the following relation

$$F^{\text{vib}}(T) = \int_0^\infty n_{\text{ph}}(w) f_{\text{vib}}(\omega, T)\, \mathrm{d}\omega, \tag{6.53}$$

where $n_{\text{ph}}(\omega)$ is the vibrational density of states (VDOS) [194, 195] and

$$f_{\text{vib}}(\omega, T) = \frac{1}{2}\hbar\omega + k_B T \ln\left(1 - e^{-\frac{\hbar\omega}{k_B T}}\right) \tag{6.54}$$

is the free energy in a mode with frequency ω at temperature T. Hence, at high temperatures, lower frequencies contribute the most to the free energy. The free energy in Eq. (6.54) includes quantum mechanical effects that are important at low temperatures.

Now, if a second-order (harmonic) force constant model is constructed from a general interaction potential using either the direct or regression approach with small displacements, as described in Sec. 6.1.5, at the relax 0 K volume (disregarding zero-point motion effects), V_0, it is referred to as the harmonic approximation (HA). Free energies according to Eq. (6.53) from a HA is a good approximation for many systems at low temperatures. However, the HA is inadequate to explain thermal expansion, an important effect at higher temperatures, since the equilibrium lattice parameter is the same for all T.

A popular method to account for thermal expansion is quasi-harmonic approximation (QHA), where the HA is applied to several volumes and the minimum of $F(V, T) = E_0(V) + F_{\text{vib}}(T, V)$ with respect to the volume is found for each T. It is also possible to consider a system at pressure P and then minimize $G = F + PV$. In the general case, the vibrational frequencies are lowered with increasing volume. Hence, from Eqs (6.53) and (6.54) F_{vib} generally decreases with increasing volume. Further, E_0 has its minimum at V_0 and will, therefore, increase if the volume is increased from V_0. Consequently, the balance of $F_{\text{vib}}(V, T)$ and $E_0(V)$ is what generates the thermal expansion in the QHA model. As the temperature increases in a system, so do the displacements, and generally, the motion starts to deviate from the harmonic behaviour for large displacements. Consequently, the frequencies in the system start to deviate from the 0 K values. This effect is not handled by the QHA, since HA is used for all volumes. To handle this effect, the frequencies and, hence, the force constants need to be temperature dependent. This can be done by generating effective harmonic models (EHMs) using the regression approach at different volumes and temperatures from MD simulations [196, 197, 198]. Moreover, since the EHM can be sampled at high temperatures, dynamical instabilities, i.e. imaginary phonon modes, can be stabilized. Hence, using EHM free energies for systems which are dynamically unstable at low temperatures can be computed, something not attainable by the traditional HA and QHA approaches.

Another method to calculate full anharmonic vibrational free energies is to do λ-integration, as described in Sec. 6.3.1, between the system of interest and an Einstein crystal, i.e. a system of uncoupled harmonic oscillators, for which we know the free energy[199, 200].

6.3.2.3 Configurational free energy

For solids the configurational contribution to the free energy $F_{\text{conf}}(T)$ arises from changes in the occupation of the atomic lattice sites. In this thesis we will consider configurational free energy from C vacancies and W to Ti substitutions in WC. However, to present this method in simple way we will consider a general system of two species, A and B, on a lattice of size N. The number of atoms of each species is denoted N_{A} and N_{B}, where $N_{\text{A}} + N_{\text{B}} = N$. Hence, the composition can be uniquely defined by A_{1-x}B_x, where $x = N_{\text{B}}/N$.

In the semi-grand canonical (SGC) ensemble the T and chemical potentials, μ_{A} and μ_{B}, are fixed and the probability of being in each microstate (or configuration) σ is given by

$$P(\sigma, T) \propto e^{-[E(\sigma) - N_{\text{A}}\mu_{\text{A}} - N_{\text{B}}\mu_{\text{B}}]/k_{\text{B}}T}. \tag{6.55}$$

Further, since $N_{\text{A}} + N_{\text{B}} = N$ and N is fixed we get

$$P(\sigma, T) \propto e^{-[E(\sigma) - N_{\text{B}}(\mu_{\text{B}} - \mu_{\text{A}})]/k_{\text{B}}T}. \tag{6.56}$$

Configurations according to $P(\sigma)$ can be obtained using MC simulations, e.g. the standard Metrolpolis MC technique[184], where A atoms are flipped to B atoms and vice versa. This allows averages such as $\langle E(\sigma)\rangle$ and $\langle N_{\text{B}}\rangle$, and hence also $x = \langle N_{\text{B}}\rangle/N$ to be calculated. Moreover, for a fixed T, $\Delta\mu = \mu_{\text{B}} - \mu_{\text{A}}$ as a function of x, i.e., $\Delta\mu = \Delta\mu(x, T)$, can be obtain.

Once $\Delta\mu(x, T)$ is known, we can perform thermodynamic integration, which is described in Sec. 6.3.1, between two compositions at constant P and T using the thermodynamic relation in Eq. (6.40) to find the Gibbs free energy difference between the two compositions according to

$$G(x_2, T) - G(x_1, T) = N \int_{x_1}^{x_2} \Delta\mu(x, T)\mathrm{d}x. \tag{6.57}$$

However, since $F = G$ at $P = 0$, the Helmholtz free energy difference at zero pressure may be found by switching G for F in Eq. (6.57). Further, in the MC simulation we disregard F_{el} and F_{vib}, hence, $F = E_0 - F_{\text{conf}}$. From this follows that the configurational free energy at composition x, $F_{\text{conf}}(x, T)$, can be found from the following relation:

$$E_0(x) + F_{\text{conf}}(x, T) = E_0(0) + N \int_0^x \Delta\mu(x', T)\mathrm{d}x'.$$

Here, x=0 corresponds to a pure A system, hence, $F_{\text{conf}}(x = 0, T) = 0$.

Now, if we return to the WC system, A and B could represent W and Ti, respectively. Further, A and B could also represent C and C vacancy, respectively. In this case, B is not an atomic species and, hence, the total number of atoms changes during the MC simulation, i.e. $N = N_{\text{A}}$. This ensemble is referred to as the grand canonical (GC) ensemble. However, the methodology described above still holds if we let $\mu_{\text{B}} = 0$ and, hence, $\Delta\mu = \mu_{\text{C}}$. In WC there are two sublattices: W and C. Then, the configurational free energy of any composition may be found by first integrating along the composition of the first sublattice while keeping the second fixed, and then integrating the composition of the second sublattice while keeping the first fixed.

The configurational free energy can also be calculated using thermodynamic integration from MC simulations in the canonical (NVT) ensemble. Now, consider again the same A-B system as above, then, in the canonical ensemble N_{A}, N_{B}, V and T are kept fixed and the probability of observing a configuration is given by

$$P(\sigma, T) \propto e^{-[E(\sigma)]/k_{\text{B}}T}. \tag{6.58}$$

Now, since we have a fixed composition the MC simulations involves swapping the positions of an A atom and a B atom to generate configurations in the canonical ensemble. From the MC simulation ensemble average of the potential energy for a fixed x and T, i.e. $\langle E(\sigma)\rangle_{x,T}$, may be found. Further, since $F(x, T) = E(x, T) - TS(x, T)$ and $E(x, T) = \langle E(\sigma)\rangle_{x,T}$, finding the entropy $S(x, T)$ will give us $F(x, S)$. If we use the thermodynamic relation in Eq. (6.39) and $[\partial E/\partial S]_{N,T} = [\partial U/\partial S]_{N,T}$ we get

$$dS = \frac{1}{T} dU.$$

Hence, from a thermodynamic integration we may find the entropy difference between two temperatures according to

$$S(x, T_2) - S(x, T_1) = \int_{T_1}^{T_2} \frac{\mathrm{d}S(x, T)}{\mathrm{d}T} \mathrm{d}T.$$

With the definition of constant volume heat capacity $C_V = T\mathrm{d}S/\mathrm{d}T$ we get

$$S(x, T_2) - S(x, T_1) = \int_{T_1}^{T_2} \frac{1}{T} C_v(x, T) \mathrm{d}T,$$

Now, since $S(x, \infty)$ is known from ideal mixing, we may find the entropy for each temperature according to

$$S(x, T) = S(x, \infty) + \int_{\infty}^{T} \frac{1}{T'} C_v(x, T') \mathrm{d}T'. \tag{6.59}$$

Consequently, by computing the heat capacity for a series of temperatures allows for extraction of the configurational entropy via (6.59). C_V is related to the variance of the potential energy and can be calculated as[156, 179]

$$C_v(x,T) = \frac{\langle E(\sigma)^2 \rangle_{x,T} - \langle E(\sigma) \rangle_{x,T}^2}{k_B T^2}.$$

As stated above we disregard F_{el} and F_{vib} in the MC simulations, and hence $F(x,T) = E_0(x) + F_{\text{conf}}(x,T)$, where $F(x,T) = \langle E(\sigma) \rangle_{x,T} - TS(x,T)$.

In Paper IV and Paper V, MC in the GC ensemble is used for the configurational free energy of C vacancies in bulk γ-WC and in γ-WC thin films at δ-WC/Co phase boundaries in undoped cemented carbides, respectively. In Paper VI, MC in the canonical ensemble is used for the configurational free energy of W-Ti substitutions and C vacancies in γ-(Ti,W)C thin films at δ-WC/Co phase boundaries in Ti doped cemented carbides.

7 Conclusions

Using atomic-scale methods based on first-principles calculations, this thesis provides several new insights to the thermodynamics of interfaces and surfaces in cemented carbides. This includes insights to both properties associated with equilibrium thermodynamics, such as interfacial phase diagrams and wettability, and non-equilibrium properties such as grain boundary sliding resistance. Many of these properties are hard to investigate experimentally, especially on the atomic scale. Hence, insight from first-principles are highly valued. Here follows an account of the main conclusions from the appended papers.

7.1 Wettability and alternative binders

As a composite material, the unique macroscopic mechanical properties, i.e., simultaneous high hardness and good toughness, of cemented carbides rely heavily on the microstructure of the material. For instance, to get satisfactory densification during liquid phase sintering the binder phase must wet the carbide phase sufficiently. Further, the high hardness is dependent on the existence of a continuous skeleton of carbide grains, while the high toughness is dependent on a continuous skeleton of binder grains. Hence, to maintain a high hardness the binder must not wet carbide/carbide grain boundaries, i.e., the grain boundaries must resist being infiltrated by the binder phase. Further, Co has recently been reported as carcinogenic, especially in the form of cemented carbide particle dust. Hence, there is currently a large driving force for replacing Co as the dominating binder for some other transition metal such as Ni or Fe or an alloy.

Wettability is an equilibrium property that is governed by equilibrium interface and surface free energies. Hence, quantifying wettability using atomic-scale calculations involves calculating the interface and surface free energies of the system.

7.1.1 Interface and surface energies at 0 K

In Paper I, interface and surface energies in undoped WC–Co and WC–Ni cemented carbides at 0 K were calculated using density functional theory (DFT). The study included WC/binder phase boundaries, WC/WC grain boundaries and WC and binder surfaces. In all cases the local chemistry of the interface was optimized by considering different interface/surface plane terminations and systematically substituting interface/surface atoms to simulate equilibrium conditions in the cemented carbide. The model interfaces and surfaces are thoroughly presented in Chapter 5. In Paper I, it was found that adsorption of binder atoms to WC surfaces and segregation of binder atoms to WC/WC grain boundaries had a strong effect on the surface and grain boundary energies. In the latter case we found that in essentially all studied grain boundaries atoms from the binder phase in both WC–Co and WC–Ni cemented carbides segregate in half a monolayer proportion. Moreover, there was a weak or no effect from changes in local chemistry on WC/binder phase boundaries and binder surfaces. Additionally, from Paper V it can be concluded that no changes in the local structure of WC/Co phase boundaries occurs at low temperatures.

From Paper I it can be concluded that, in general, the phase boundaries were associated with the lowest excess energies. Grain boundary and binder surface energies were similar and somewhat larger compared with the phase boundary energies. The WC surface energies were considerably larger than any other interface/surface energies. This is expected since it cost a lot to break the covalent bonds in WC compared to the metallic bonds of Co. Further, in the phase and grain boundaries bulk carbide bonds are replaced with carbide-binder bonds or new carbide bonds, hence not as expensive as just breaking the bonds.

When comparing the two binders, Co and Ni, it was found that Ni has the lowest surface energy. Moreover, the reduction in WC surface energy from adsorption of Ni atoms were larger compared with Co. The reduction in grain boundary energy from segregation of binder atoms was found to larger in WC–Co compared with WC–Ni.

7.1.2 Temperature dependent interface and surface free energies

In Paper II, the temperature dependency of WC/Co phase boundaries, WC/WC grain boundaries and WC and Co surfaces in undoped WC–Co cemented carbides were investigated using an analytical bond-order potential (ABOP). This included temperatures above the melting temperature for the binder phase. The free energy methods used, which are presented in Sec. 6.3, were: thermodynamic λ-integration to an Einstein crystal, temperature integration, quasi-harmonic approximation (QHA) and surface stress for liquid surface free energy. Additionally, joining/cleaving simulations to calculate the work of adhesion of WC/Co phase boundaries was used in order to calculate the

WC/Co phase boundary free energy by combining with calculated values for the WC and Co surface free energies.

The results shows that up to the melting point of the binder there is only minor effect on the interface/surface free energies with a general decrease of about 10% from the value at 0 K. Upon melting, the Co surface free energy decreases discontinuously. Since there is no directional dependence of the liquid surface free energy, the size of the discontinuity depends highly on the Co facet studied. However, taking the mean of a Wulff construction using the (111) and (001) facets gives a jump of about 10% from the surface energy at 0 K. Also the WC/Co phase boundary free energies may change discontinuously depending on the type of phase boundary. Additionally, from Paper V it can be concluded that there is only a minor decrease in phase boundary energy from changes in the local structure of WC/Co phase boundaries at temperatures where the binder has molten.

Now, returning to the results in Paper II, the behaviour of the excess free energies for WC/WC grain boundaries and WC surfaces are not affected by the melting of the binder phase. Further, the trend presented for the interface/surface energies in WC–Co cemented carbides in the previous section holds for all studied temperatures. In fact, the WC surface free energies, which have largest absolute value, decrease the least of all interfaces and surfaces.

In Paper VI, Ti was found to segregate to WC/Co phase boundaries in Ti-doped cemented carbides and form thin cubic (Ti,W)C films, both at solid state and liquid phase sintering temperatures. The segregation was found to be in one monolayer proportion and the decrease in WC/Co phase boundary energy from the addition of Ti depended a lot on if gamma phase was precipitated in the material or not. However, it could be comparable to the decrease in grain boundary energy from segregation of Co and Ni atoms.

7.1.3 Wettability

In Paper I, we found that, in both WC–Co and WC–Ni cemented carbides, the wetting of WC surfaces is stronger in W-rich materials compared with C-rich materials and this dependency on the environment is caused by changes in the local chemistry of the interfaces. When the binder wets a WC surface, the WC surface is replaced by a binder surface and a WC/binder phase boundary, and the tendency for wetting is decided by the balance of the interface energies in the dry and wet case. From the DFT calculations we found that, at equilibrium with the binder phase, WC surfaces are generally C-terminated with adsorbed binder atoms or either W or mixed W and C terminated with fractions of the W atoms replaced for binder atoms. Further, the WC/Co phase boundaries generally have W or mixed W and C termination with no substitution of binder atoms and binder surfaces are free from W or C impurities. Hence, there is, generally, a higher W content in the phase boundaries compared to the WC surfaces

and upon wetting of the WC surfaces, W (C) atoms has to be added to (removed from) the interface. This process is easier if there is an abundance of W in the binder.

We found that the wettability of WC surfaces by both binders, Co and Ni, are similar. Further, in both WC–Co and WC–Ni the wetting is only partial at low temperatures. However, by adding the temperature dependencies of the interface/surface free energies from Paper II to the 0 K values for WC–Co we found that wetting is perfect for a W-rich material, while partial for a C-rich material. This result is supported by an experimental study on wettability in WC–Co cemented carbides for various C-contents found in the literature[41].

When the binder phase wets, or infiltrates, a WC/WC grain boundary, the grain boundary is replaced by two WC/binder phase boundaries. Again, it is the balance of interface energies between the dry and wet case that that is the measure of the tendency for for wetting (infiltration). In Paper I, the grain boundaries are found to resist infiltration in by the binder phase in both WC–Co and WC–Ni at 0 K. However, the resistance is weaker in WC–Ni compared to WC–Co, which can be explained by the stronger segregation of binder atoms to WC/WC grain boundaries in WC–Co and lower WC/binder phase boundary energies in WC–Ni. By adding temperature effects from Paper II to the 0 K values for WC–Co we found that grain boundaries will resist infiltration also at liquid phase sintering temperatures, however, the resistance is somewhat weakend. This supports the conclusion that a continuous skeleton of hard phase WC grains inside a matrix of binder phase is built up during the sintering process[4, 30] giving rise to the materials superior mechanical strength. Regarding alternative binders, Ni should wet WC surface equally well as Co, however, there is an increased risk of infiltrating WC/WC grain boundaries at high temperatures.

The formation of cubic WC films at the WC/Co phase boundaries, which were predicted in Paper V, will likely not affect the wetting behaviour drastically since the change in interface energy is very small. Additionally, due to the rather large structural changes needed, it is likely that these films do not form directly during wetting but rather during the solution-reprecipitation stage of the sintering. This is likely also case with complexions formed in doped cemented carbides.

7.2 Grain boundary sliding

Grain boundary sliding is thought to be the most important deformation mechanism of WC–Co cemented carbides at high temperatures and it is believed to be facilitated by grain boundaries being broken up and infiltrated by grain boundaries. In Paper III, an ABOP for WC–Co was fitted and used in molecular dynamics (MD) simulations to study grain boundary sliding with various amounts of Co in the grain boundary at different temperatures. Grain boundary sliding was simulated by moving two WC grains in opposite directions with a constant velocity and measuring the resulting shear stress. The

most stable grain boundary configurations, i.e., with 0.5 monolayer of segregated Co, was found to give the highest shear stress. These grain boundaries were found to amorphize during the sliding which explains the higher shear stress compared to the clean grain boundaries that slid in a manner that resembles misfit dislocation motion, during which, fewer bonds are simultaneously broken. Hence, submonolayer segregation of binder atoms to WC/WC grain boundaries strengthens the material by impeding grain boundary sliding. Furthermore, for Co lamella of 6 atomic layer thickness, i.e. roughly 1 nm, the shear stress dropped by one order of magnitude at 1500 K compared to the most stable configuration. Also at lower temperatures the shear stress was reduced significantly by introducing the Co lamella. Consequently, very thin lamellas of Co is sufficient to facilitate grain boundary sliding. For systems with a few atomic layers of more of Co the melting of Co lowered the shear stress by approximately one order of magnitude.

7.3 Thin cubic films in WC/Co phase boundaries

During sintering, especially in the liquid phase stage, the WC grains grows by means of solution-reprecipitation. To get a material with a high strength it is important to keep the size of the WC grains small. Hence, grain growth inhibitors, such TiC or VC, are added to the material. The grain growth inhibition is believed to be caused by the formation of thin cubic films (complexions) at WC/binder phase boundaries that hinders reprecipitation of W and C to the WC grains. These films have been observed in high resolution TEM studies, however, to understand the thermodynamics of these complexions, atomic scale calculations are crucial.

The study of thin cubic film complexions at WC/Co phase boundaries is spread out over the last three papers of this thesis, i.e., Papers IV-VI. In industry, doped cemented carbides are of most importance and to that end the final paper of this thesis is an investigation of the thermodynamics of cubic (Ti,W)C films in Ti doped cemented carbides. Cubic films are, however, also observed at WC/Co phase boundaries in undoped WC–Co cemented carbides. Consequently, to get deeper understanding of the stabilization of the thin cubic films, the more pure undoped case was studied first.

7.3.1 WC bulk phases

The cubic WC bulk phase, referred to as γ-WC, is only thermodynamically stable above 2800 K and it can contain a lot of C vacancies. Hence, to be able to predict the formation of γ-WC complexions at WC/Co phase boundaries a precise description of γ-WC phase is needed. In Paper IV, γ-WC was therefore thoroughly studied by constructing an alloy cluster expansion (CE) for C vacancies from DFT calculations to find ground states and running MC simulations to find the configurational free energy for vari-

ous C concentration. Since γ-WC with a low vacancy concentration is dynamically unstable at low temperatures, standard vibrational free energy techniques such as harmonic approximation (HA) and QHA are not relevant. Instead, ab-initio molecular dynamics (AIMD) simulations of the ground states were used to construct effective harmonic models (EHMs) for various temperatures, which were then used to find the vibrational free energy. The effect of stronger vibrational free energy for disordered high-temperatures structures was also included. Additionally, electronic free energy was included and, finally, the free energy was optimized with respect to volume which thus incorporated thermal expansion. These free energy methods were presented in Sec. 6.3. δ-WC, i.e. hexagonal WC, which is stable below 2800 K was also studied, however, since δ-WC is essentially stoichiometric, C vacancies were treated in the dilute limit. The free energy landscapes were used to generate a W-C phase diagram in rather good agreement with experimental phase diagrams. It was concluded that the γ-WC phase is far more anharmonic and has a stronger electronic free energy contribution compared to δ-WC. Further, at high temperatures, it was crucial to incorporate disordered structures in the calculation of the vibrational free energy for high C vacancy concentrations.

7.3.2 Undoped cemented carbides

For the thin film complexions it was not feasible to perform an analysis corresponding to the one in Paper IV. Therefore, a simpler modeling was used for the thin films in Paper V. The modeling involved generating alloy CEs based on DFT calculations to find ground states and running MC simulations to find the configurational free energy for multiple thin film structures and treating the vibrations in the HA for the ground states. Then, corrections from the bulk analysis in Paper IV were added.

The study considered thin cubic films in the (0001) WC/ (111) Co phase boundary, see Sec. 5.4.2 for more details, and from the free energy landscape an interfacial phase diagram was created. Thin cubic films were predicted in W-rich materials above 1800 K, however, not in C-rich materials. The films forms more easily in W-rich materials mainly since C vacancies are more favourable under W-rich conditions compared with C-rich conditions. Thin cubic films in undoped cemented carbides are generally not believed to be stable at room temperature, instead it forms during liquid phase sintering and freeze in during the subsequent cooling. Hence, the presence of films also at room temperatures. In the literature, thin cubic films are reported from experiments in both W-rich and C-rich materials, however, more frequently observed in W-rich materials[10]. Furthermore, it is possible that fluctuations in the composition of the material may increase the W content locally thus allowing films to form also in C-rich materials. Hence, the results of Paper V agrees rather well with experiments.

Since, there is still a cost of creating γ-WC at 1800 K very thin films, only 4 W/C atomic layers, were predicted in Paper V. This is somewhat thinner than the films ob-

served experimentally, however, in an experimental set-up films might grow beyond the equilibrium thickness since the transformation of inner atomic layers from γ-WC to δ-WC may be limited by kinetic processes. Further, in experiments only W atoms are visible and very thin cubic films are therefore harder to identify. Moreover, the layer spacings of the thicker model systems agrees well with experimental layer spacings from Ref. [10], indicating that the models are relevant.

7.3.3 Ti-doped cemented carbides

In Paper VI, thin films of cubic structure in Ti-doped cemented carbides was studied. Here, the method used for the undoped case was extended to include W↔Ti substitutions. Thin cubic (Ti,W)C films were predicted at both solid state and liquid phase sintering temperatures. Further, the films were found to be stable also for Ti concentrations when no gamma phase is formed in the material. Hence, the grain inhibition effect should be present already for low amounts of Ti addition. Moreover, since the TiC/Co phase boundary is associated with a considerably higher excess energy compared to the γ-WC/Co phase boundary, Ti was primarily found in the inner layers of the thin films, leaving the outer layer towards Co W-terminated. This structural observation agrees very well with a recent HRTEM study of thin films in Ti doped cemented carbides[110]. Hence, Paper VI provides an atomistic explanation as to why Ti is not found in the terminating carbides planes towards the binder. Furthermore, C vacancy concentrations in the (Ti,W)C film were found to be low and, hence, not a crucial factor for the stabilization of the films. However, they were found to decrease the layer spacing in the cubic film and give a more correct match to layer spacings observed experimentally[110].

8

Outlook

In this thesis interfaces and surfaces in cemented carbides have been thoroughly studied using atomic-scale methods and many new insights to the thermodynamics of the interfaces and surfaces has been found. With the acquired knowledge about atomic-scale computations there are plenty of possible extension to the work in this thesis. Since there is a large drive towards replacing Co as the primary binder, further analysis of interface and surface properties of cemented carbides with alternative binders would be highly valued in the community of cemented carbides. This could include properties such wetting and the formation of complexions which are both important factors in the manufacturing of cemented carbides. Further, the bulk analysis performed in Paper IV could be applied to other systems which could aid in developing thermodynamic databases or phase diagrams. These are crucial assets when new compositions are searched for in order to get a material with the desired phase composition. Moreover, the analysis of thin cubic films in WC/Co phase boundaries are possible to extend to other dopants or even systems with multiple dopants. Furthermore, MD simulations using the ABOP, similar to the ones in Paper III, could be used to simulate cemented carbide microbeam bending to get detailed atomistic information on the failure of these microbeams. This could be a good complement to experimental studies on microbeam bending in cemented carbides found in the literature. Finally, MD simulations with the ABOP could be used to study the initial growth of WC grains from nucleation of W and C atoms from the binder phase.

There are also possibilities for improvements of the methods in the appended studies. For instance, the magnetic free energy contribution and local spin fluctuations, which might be important for Co, has not been included in the temperature dependent free energy calculations. Furthermore, the connection between vibrational and configurational degrees of freedom could be improved by sampling the vibrational free energy contributions for a larger set of structures that are representative for the rele-

vant temperature. This is, however, something that will add more computational time to methods that already consume a considerable amount of computer time. It would, therefore, be more desirable to do a more effective and coupled sampling of the configurational and vibrational degrees of freedom. In MD simulations the times accessible are in general too short to sample a wide enough area in configurational space. However, this shortcoming can perhaps be overcome by effectively couple MD and MC simulations.

Acknowledgments

First of all, I would like to express my sincere gratitude to my supervisor Göran Wahnström. Thank you for giving me the opportunity to pursue this work and to realize my dream to become a scientist in physics. You have been a very enthusiastic, supportive, knowledgeable, and patient supervisor. During my time as a PhD student I had two wonderful children. It therefore means a great deal to me that you have always been such an understanding and supportive manager and I always felt encouraged to spend time with my family.

I would also like thank my co-worker Erik Fransson for the long-lasting collaboration which, according to my opinion, has led to a couple of pretty awesome papers. I would definitely not have gotten this far in the research of cemented carbides without your assistance. Furthermore, I really appreciated all (lengthy) discussions in your office. I'm sorry, Mattias Ångqvist, for frequently disturbing you while working, but yours and Eriks office just seemed like the place to hang out for discussions. However, I would also like to thank you for your collaboration and work on Paper IV. Perhaps, joining mine and Erik's discussions was the best way to avoid the disturbance. Also, thank you for helping me making a nice cover figure for the thesis.

I would like to thank my co-supervisor Hans-Olof Andrén for very interesting discussions and conversations while travelling together. Also, your help with reviewing and proofreading articles and this thesis is much appreciated

Further, I also want to thank all colleagues at the Condensed Matter and Materials Theory group for making it such nice workplace. I would also like to thank my past co-workers Martin Petisme and Sven Johansson for discussions and guidance at the start of my PhD studies.

Moreover, I would also like to thank everybody involved in the joint projects, including people from Sandvik, Seco Tools, KTH, Grenoble INP, and Materials Microstructure at Chalmers. During the recurrent meetings I have learned a lot about cemented carbides and they have therefore been an important part of my research.

Furthermore, I would like to acknowledge the financial support from the Swedish Foundation for Strategic Research (SSF) and the Swedish Research Council (VR) as well as all the computer time that was provided by the Swedish National Infrastructure for Computing (SNIC) on clusters at National Supercomputer Centre (NSC) in Linköping

and at Chalmers Centre for Computational Science and Engineering (C3SE) in Göteborg.

I would also like to thank my parents and my brother for the support and love through the years.

Lastly, I want to thank my fiancée Karolina and my two sons Sebastian and William for making our home a lovely place and for your support, love and all the fun moments through the years.

Bibliography

[1] Ask Hjorth Larsen, Jens Jørgen Mortensen, Jakob Blomqvist, Ivano E Castelli, Rune Christensen, Marcin Dułak, Jesper Friis, Michael N Groves, Bjørk Hammer, Cory Hargus, Eric D Hermes, Paul C Jennings, Peter Bjerre Jensen, James Kermode, John R Kitchin, Esben Leonhard Kolsbjerg, Joseph Kubal, Kristen Kaasbjerg, Steen Lysgaard, Jón Bergmann Maronsson, Tristan Maxson, Thomas Olsen, Lars Pastewka, Andrew Peterson, Carsten Rostgaard, Jakob Schiøtz, Ole Schütt, Mikkel Strange, Kristian S Thygesen, Tejs Vegge, Lasse Vilhelmsen, Michael Walter, Zhenhua Zeng, and Karsten W Jacobsen. The atomic simulation environment—a python library for working with atoms. *J. Phys.: Condens. Matter*, 29:273002, 2017.

[2] Blender Online Community. *Blender - a 3D modelling and rendering package*. Blender Foundation, Stichting Blender Foundation, Amsterdam, 2018.

[3] Wayne D. Kaplan, Dominique Chatain, Paul Wynblatt, and W. Craig Carter. A review of wetting versus adsorption, complexions, and related phenomena: the rosetta stone of wetting. *J. Mater. Sci.*, 48:5681, 2013.

[4] H E Exner. Physical and chemical nature of cemented carbides. *Int. Mater. Rev.*, 24:149, 1979.

[5] Leo Prakash. 1.02 - fundamentals and general applications of hardmetals. In Vinod K. Sarin, editor, *Comprehensive Hard Materials*, page 29. Elsevier, Oxford, 2014.

[6] B. Aronsson. *The origins and growth of cemented carbides*. Sandvik Group, Stockholm, 2005.

[7] Turning re-invented - primeturning™ and coroturn® prime. https://www.youtube.com/watch?v=nCYihCotzHw. Accessed: 2017-07-04.

[8] S. Norgren, J. Garcia, A. Blomqvist, and L. Yin. Trends in the p/m hard metal industry. *Int. J. Refract. Met. Hard Mater.*, 48:31, 2015.

[9] G. Östberg, K. Buss, M. Christensen, S. Norgren, H.-O. Andrén, D. Mari, G. Wahnström, and I. Reineck. Effect of TaC on plastic deformation of WC-Co and Ti(C,N)-WC-Co. *Int. J. Refract. Met. Hard Mater.*, 24:145, 2006.

[10] V. Bounhoure, S. Lay, M. Loubradou, and J. M. Missiaen. Special WC/Co orientation relationships at basal facets of WC grains in WC-Co alloys. *J. Mater. Sci.*, 43:892, 2008.

[11] I. Konyashin, A. Sologubenko, T. Weirich, and B. Ries. Complexion at wc-co grain boundaries of cemented carbides. *Mater. Lett.*, 187:7, 2017.

[12] Xingwei Liu, Xiaoyan Song, Haibin Wang, Xuemei Liu, Fawei Tang, and Hao Lu. Complexions in wc-co cemented carbides. *Acta Mater.*, 149:164, 2018.

[13] Z. Zak Fang, Mark C. Koopman, and Hongtao Wang. 1.04 - cemented tungsten carbide hardmetal-an introduction. In Vinod K. Sarin, editor, *Comprehensive Hard Materials*, page 123. Elsevier, Oxford, 2014.

[14] C.M. Fernandes and A.M.R. Senos. Cemented carbide phase diagrams: A review. *Int. J. Refract. Met. Hard Mater.*, 29:405, 2011.

[15] T. W. Penrice. Alternative binders for hard metals. *J. Mater. Shaping Technol.*, 5:35, 1987.

[16] V.A Tracey. Nickel in hardmetals. *Int. J. Refract. Met. Hard Mater.*, 11:137, 1992.

[17] IJ Shon, KI Na, IY Ko, JM Doh, and JK Yoon. Effect of FeAl3 on properties of (W,Ti)C-FeAl3 hard materials consolidated by a pulsed current activated sintering method. *Ceram. Int.*, 38:5133, 2012.

[18] JZ Long, ZJ Zhang, T. Xu, W. Peng, XY Wei, BZ Lu, and RQ Li. WC-Ni3Al-B composites prepared through Ni+Al elemental powder route. *Trans. Nonferrous Met. Soc. China*, 22:847, 2012.

[19] M. Ahmadian, D. Wexler, T. Chandra, and A. Calka. Abrasive wear of WC–FeAl–B and WC–Ni3Al–B composites. *Int. J. Refract. Met. Hard Mater.*, 23:155, 2005.

[20] Mehdi Ahmadian-Najafabadi, Materials University of Wollongong. School of Mechanical, and Mechatronic Engineering. Sintering, microstructure and properties of WC-FeAl-B and WC-Ni3Al-B composite materials, 2005.

[21] Andrea Mueller-Grunz, Patricia Alveen, Sven Rassbach, Ralph Useldinger, and Steven Moseley. The manufacture and characterization of wc-(al)cocrcufeni cemented carbides with nominally high entropy alloy binders. *Int. J. Refract. Met. Hard Mater.*, 84:105032, 2019.

[22] D. Linder, E. Holmström, and S. Norgren. High entropy alloy binders in gradient sintered hardmetal. *Int. J. Refract. Met. Hard Mater.*, 71:217, 2018.

[23] Erik Holmström, Raquel Lizárraga, David Linder, Armin Salmasi, Wei Wang, Bartek Kaplan, Huahai Mao, Henrik Larsson, and Levente Vitos. High entropy alloys: Substituting for cobalt in cutting edge technology. *Appl. Mater. Today*, 12:322, 2018.

[24] B. Aronsson. Processing-properties relationship in cemented carbide. *Key Eng. Mater.*, 29:529, 1989.

[25] J. W. Lee, D. Jaffrey, and J. D. Browne. Influence of process variables on sintering of WC-25 wt-%Co. *Powder Metall.*, 23:57, 1980.

[26] G S Upadhyaya. *Cemented Tungsten Carbides: Production, Properties, and Testing*. Noyes Publications, 1 edition, 1998.

[27] E Lassner and W-D Schubert. *Tungsten: Properties, Chemistry, Technology of the Element, Alloys, and Chemical Compounds*. Kluwer Academic/Plenum Publishers, 1999.

[28] Pankaj K. Mehrotra. 1.07 - powder processing and green shaping. In Vinod K. Sarin, editor, *Comprehensive Hard Materials*, page 213. Elsevier, Oxford, 2014.

[29] Thomas A. Wolfe, Thomas J. Jewett, and Raj P. Singh Gaur. 1.06 - powder synthesis. In Vinod K. Sarin, editor, *Comprehensive Hard Materials*, page 185. Elsevier, Oxford, 2014.

[30] H.-O. Andrén. Microstructures of cemented carbides. *Mater. Des.*, 22:491, 2001.

[31] Uwe Schleinkofer, Christoph Czettl, and Claude Michotte. 1.16 - coating applications for cutting tools. In Vinod K. Sarin, editor, *Comprehensive Hard Materials*, page 453. Elsevier, Oxford, 2014.

[32] P Schlund, P Kindermann, H.-G Sockel, U Schleinkofer, W Heinrich, and K Görting. Mechanical behaviour of pvd- and cvd-coated hard metals under cyclic loads. *Int. J. Refract. Met. Hard Mater.*, 17(1):193, 1999.

[33] Viktor P. Astakhov. Chapter 6 improvements of tribological conditions. In *Tribology of Metal Cutting*, volume 52 of *Tribology and Interface Engineering Series*, page 326. Elsevier, 2006.

[34] José Garcia and Reinhard Pitonak. The role of cemented carbide functionally graded outer-layers on the wear performance of coated cutting tools. *Int. J. Refract. Met. Hard Mater.*, 36:52, 2013. Special Section: Recent Advances of Functionally Graded Hard Materials.

[35] Mark Fitzsimmons and Vinod K Sarin. Development of cvd wc–co coatings. *Surf. Coat. Tech.*, 137(2):158, 2001.

[36] Randall M. German. 1.08 - consolidation techniques. In Vinod K. Sarin, editor, *Comprehensive Hard Materials*, page 237. Elsevier, Oxford, 2014.

[37] M. Göthelid, S. Haglund, and J. Ågren. Influence of O and Co on the early stages of sintering of WC-Co: A surface study by AES and STM. *Acta Mater.*, 48:4357, 2000.

[38] V. Bounhoure, S. Lay, F. Charlot, A. Antoni-Zdziobek, E. Pauty, and J.M. Missiaen. Effect of c content on the microstructure evolution during early solid state sintering of WC–Co alloys. *Int. J. Refract. Met. Hard Mater.*, 44:27, 2014.

[39] J. Kishino, H. Nomura, S.-G. Shin, H. Matsubara, and T. Tanase. Computational study on grain growth in cemented carbides. *Int. J. Refract. Met. Hard Mater.*, 20:31, 2002.

[40] V. Bounhoure, J. M. Missiaen, S. Lay, and E. Pauty. Discussion of nonconventional effects in solid-state sintering of cemented carbides. *J. Am. Ceram. Soc.*, 92:1396, 2009.

[41] I. Konyashin, A.A. Zaitsev, D. Sidorenko, E.A. Levashov, B. Ries, S.N. Konischev, M. Sorokin, A.A. Mazilkin, M. Herrmann, and A. Kaiser. Wettability of tungsten carbide by liquid binders in WC–Co cemented carbides: Is it complete for all carbon contents? *Int. J. Refract. Met. Hard Mater.*, 62, Part B:134, 2017.

[42] A. Fernández Guillermet. Thermodynamic properties of the Co-W-C system. *Metall. Trans. A*, 20A:935, 1989.

[43] A. Fernández Guillermet. The Co–Fe–Ni–W–C phase diagram: a thermodynamic description and calculated sections for (Co–Fe–Ni) bonded cemented WC tools. *Z. Metallkd.*, 80:83, 1989.

[44] Gopal S. Upadhyaya. 2 - crystal structure and phase equilibria. In *Cemented Tungsten Carbides*, page 7. William Andrew Publishing, Westwood, NJ, 1998.

[45] T.W. Penrice. Some characteristics of the binder phase in cemented carbides. *Int. J. Refract. Met. Hard Mater.*, 15:113, 1997. Wear Resistant Materials for the South African Industry.

[46] Bernhard Wittmann, Wolf-Dieter Schubert, and Benno Lux. WC grain growth and grain growth inhibition in nickel and iron binder hardmetals. *Int. J. Refract. Met. Hard Mater.*, 20:51, 2002.

[47] Z. Roulon, J.M. Missiaen, and S. Lay. Carbide grain growth in cemented carbides sintered with alternative binders. *Int. J. Refract. Hard Met.*, 86:105088, 2020.

[48] E O Hall. The deformation and ageing of mild steel: III discussion of results. *P. Phys. Soc. Lond. B*, 64:747, 1951.

[49] N J Petch. The cleavage strength of polycrystals. *J. Iron Steel Inst.*, 174:25, 1953.

[50] Jonathan Weidow and Hans-Olof Andrén. Grain and phase boundary segregation in WC–Co with small V, Cr or Mn additions. *Acta Mater.*, 58:3888, 2010.

[51] J. Weidow and H.-O. Andrén. APT analysis of WC–Co based cemented carbides. *Ultramicroscopy*, 111:595, 2011.

[52] Amine Yousfi. *Microstructure Development of WC-Co Based Cemented Carbides During Creep Testing*. PhD thesis, Chalmers University of Technology, Göteborg, Sweden, 2016.

[53] R Frykholm and H.-O Andrén. Development of the microstructure during gradient sintering of a cemented carbide. *Mater. Chem. Phys.*, 67:203, 2001.

[54] Peng Fan, Z. Zak Fang, and Jun Guo. A review of liquid phase migration and methods for fabrication of functionally graded cemented tungsten carbide. *Int. J. Refract. Met. Hard Mater.*, 36:2, 2013. Special Section: Recent Advances of Functionally Graded Hard Materials.

[55] I. Konyashin, A.A. Zaitsev, D. Sidorenko, E.A. Levashov, S.N. Konischev, M. Sorokin, S. Hlawatschek, B. Ries, A.A. Mazilkin, S. Lauterbach, and H.-J. Kleebe. On the mechanism of obtaining functionally graded hardmetals. *Mater. Lett.*, 186:142, 2017.

[56] I. Konyashin, B. Ries, F. Lachmann, and A.T. Fry. Gradient wc-co hardmetals: Theory and practice. *Int. J. Refract. Met. Hard Mater.*, 36:10, 2013.

[57] Daniel Tiger's Neighborhood.

[58] Sabine Lay and Jean-Michel Missiaen. 1.03 - microstructure and morphology of hardmetals. In Vinod K. Sarin, editor, *Comprehensive Hard Materials*, page 91. Elsevier, Oxford, 2014.

[59] José García, Verónica Collado Ciprés, Andreas Blomqvist, and Bartek Kaplan. Cemented carbide microstructures: a review. *Int. J. Refract. Met. Hard Mater.*, 80:40, 2019.

[60] A. S. Kurlov and A. I. Gusev. Tungsten carbides and W-C phase diagram. *Inorg. Mater.*, 42:121, 2006.

[61] Alexey S. Kurlov and Aleksandr I. Gusev. *Phases and Equilibria in the W–C and W–Co–C Systems*, page 5. Springer International Publishing, Cham, 2013.

[62] P. A. Korzhavyi, L. V. Pourovskii, H. W. Hugosson, A. V. Ruban, and B. Johansson. Ab initio study of phase equilibria in tic_x. *Phys. Rev. Lett.*, 88:015505, 2001.

[63] Hugh O. Pierson. 3 - interstitial carbides, structure and composition. In *Handbook of Refractory Carbides and Nitrides*, page 17. William Andrew Publishing, Westwood, NJ, 1996.

[64] A. A. Rempel, R. Würschum, and H.-E. Schaefer. Atomic defects in hexagonal tungsten carbide studied by positron annihilation. *Phys. Rev. B*, 61:5945, 2000.

[65] Edmund K. Storms. *The Refractory Carbides*, volume 2 of *Refractory Materials*. Academic Press, 1967.

[66] J Weidow, S A E Johansson, H-O Andrén, and G Wahnström. Transition metal solubilities in WC in cemented carbide materials. *J. Am. Ceram. Soc.*, 94:605, 2011.

[67] Amy Y. Liu, Renata M. Wentzcovitch, and Marvin L. Cohen. Structural and electronic properties of wc. *Phys. Rev. B*, 38:9483, 1988.

[68] L. F. Mattheiss and D. R. Hamann. Bulk and surface electronic structure of hexagonal wc. *Phys. Rev. B*, 30:1731, 1984.

[69] Alexandr I. Gusev, Andrej A. Rempel, and Andreas J. Magerl. *Strongly Nonstoichiometric Compounds*, page 43. Springer Berlin Heidelberg, Berlin, Heidelberg, 2001.

[70] Hugh O. Pierson. 2 - the refractory carbides. In *Handbook of Refractory Carbides and Nitrides*, page 8. William Andrew Publishing, Westwood, NJ, 1996.

[71] Mikael Christensen, Göran Wahnström, C Allibert, and S Lay. Quantitative analysis of WC grain shape in sintered WC-Co cemented carbides. *Phys. Rev. Lett.*, 94:066105, 2005.

[72] S. Lay, D. Donnadieu, and M. Loubradou. Polarity of prismatic facets delimiting WC grains in WC-Co alloys. *Micron*, 41:472, 2010.

[73] M V G Petisme, S A E Johansson, and G Wahnström. A computational study of interfaces in WC–Co cemented carbides. *Model. Simul. Mater. Sc.*, 23:045001, 2015.

[74] M. B. Stearns. 1.1.2.2 phase diagrams, lattice constants and elastic moduli: Datasheet from landolt-börnstein - group iii condensed matter · volume 19a: "3d, 4d and 5d elements, alloys and compounds" in springermaterials, 1986.

[75] T. Nishizawa and K. Ishida. The Co (cobalt) system. *Bull. Alloy Phase Diagrams*, 4:387, 1983.

[76] M. Hellsing. High resolution microanalysis of binder phase in as sintered wc–co cemented carbides. *Mater. Sci. Technol.*, 4:824, 1988.

[77] Jonathan Weidow and Hans-Olof Andrén. Binder phase grain size in WC–Co-based cemented carbides. *Scr. Mater.*, 63:1165, 2010.

[78] K.P. Mingard, B. Roebuck, J. Marshall, and G. Sweetman. Some aspects of the structure of cobalt and nickel binder phases in hardmetals. *Acta Mater.*, 59:2277, 2011.

[79] K. Hilpert, D. Kobertz, V. Venugopal, M. Miller, H. Gerads, F. J. Bremer, and H. Nickel. Phase diagram studies on the Al-Ni system. *Z. Naturforsch. pt. A*, 42:1327, 1987.

[80] Max Hansen and Kurt Anderko. *Constitution of binary alloys*. McGraw-Hill, New York, 2. edition, 1958.

[81] W. M. Haynes, editor. *CRC Handbook of Chemistry and Physics*. CRC Press/Taylor and Francis, Boca Raton, FL, 97th edition, 2016. Internet version accessed January 2017.

[82] B. Legendre and M. Sghaier. Curie temperature of nickel. *J. Therm. Anal. Calorim.*, 105:141, 2011.

[83] John Chipman. Thermodynamics and phase diagram of the Fe-C system. *Metall. Trans.*, 3:55, 1972.

[84] C. H. Allibert. Sintering features of cemented carbides WC-Co processed from fine powders. *Int. J. Refract. Met. Hard Mater.*, 19:53, 2001.

[85] C.-S. Kim, T. R. Massa, and G. S. Rohrer. Interface character distributions in WC-Co composites. *J. Am. Ceram. Soc.*, 91:996, 2008.

[86] Chang-Soo Kim and Gregory S. Rohrer. Geometric and crystallographic characterization of WC surfaces and grain boundaries in WC-Co composites. *Interface Sci.*, 12:19, 2004.

[87] S. Hagège, J. Vicens, G. Nouet, and P. Delavignette. Analysis of structure defects in tungsten carbide. *Phys. Status Solidi A*, 61:675, 1980.

[88] F. Ueda, H. Doi, F. Fujiwara, and H. Masatomi. Bend Deformation and Fracture of WC–Co Alloys at Elevated Temperatures. *T. Jpn. I. Met.*, 18(3):247, 1977.

[89] F; FUJIWARA Y; MASATOMI H DOI, H; UEDA. Influence of carbide grain size on elevated temperature tensile creep of wc-10%co alloy. *Int. J. Refract. Hard Met.*, 3:146, 1984.

[90] G. Wirmarka, G.L. Dunlop, and C. Chatfield. Tensile creep of wc–co cemented carbides at 800–900 c. *Int. J. Refract. Hard Met.*, 5:153, 1986.

[91] D. Mari, U. Marti, and P. C. Silva. A new photolithographic technique to detect the local deformation of materials: application to WC–Co composites. *Mater. Sci. Eng. A*, 158:203, 1992.

[92] Gustaf Östberg, Katharina Buss, Mikael Christensen, Susanne Norgren, Hans-Olof Andrén, Daniele Mari, Göran Wahnström, and Ingrid Reineck. Mechanisms of plastic deformation of WC–Co and Ti(C, N)–WC–Co. *Int. J. Refract. Met. Hard Mater.*, 24:135, 2006.

[93] D. Mari, S. Bolognini, G. Feusier, T. Viatte, and W. Benoit. Experimental strategy to study the mechanical behaviour of hardmetals for cutting tools. *Int. J. Refract. Met. Hard Mater.*, 17:209, 1999.

[94] Karin Mannesson, Mattias Elfwing, Alexandra Kusoffsky, Susanne Norgren, and John Ågren. Analysis of WC grain growth during sintering using electron backscatter diffraction and image analysis. *Int. J. Refract. Met. Hard Mater.*, 26:449, 2008.

[95] A. Henjered, M. Hellsing, H. O. Andrén, and H. Nordén. Quantitative microanalysis of carbide/carbide interfaces in WC–Co-based cemented carbides. *Mater. Sci. Technol.*, 2:847, 1986.

[96] Jonathan Weidow and Hans-Olof Andrén. Grain and phase boundary segregation in WC–Co with TiC, ZrC, NbC or TaC additions. *Int. J. Refract. Met. Hard Mater.*, 29:38, 2011.

[97] A.P. Sutton and R.W. Balluffi. *Interfaces in crystalline materials.* Monographs on the physics and chemistry of materials. Clarendon Press, 1995.

[98] V. Randle. Role of grain boundary plane in grain boundary engineering. *Mater. Sci. Technol.*, 26:774, 2010.

[99] R. C. Pond and W. Bollmann. The symmetry and interfacial structure of bicrystals. *Philos. Trans. R. Soc. London, Ser. A*, 292:449, 1979.

[100] S. Hagége, G. Nouet, and P. Delavignette. Grain boundary analysis in TEM. IV. Coincidence and the associated defect structure in tungsten carbide. *Phys. Status Solidi A*, 62:97, 1980.

[101] J. Vicens, M. Benjdir, G. Nouet, A. Dubon, and J. Y. Laval. Cobalt intergranular segregation in WC-Co composites. *J. Mater. Sci.*, 29:987, 1994.

[102] S. Lay and M. Loubradou. Characteristics and origin of clusters in submicron WC-Co cermets. *Philos. Mag.*, 83:2669, 2003.

[103] Vineet Kumar, Zhigang Zak Fang, S. I. Wright, and M. M. Nowell. An analysis of grain boundaries and grain growth in cemented tungsten carbide using orientation imaging microscopy. *Metall. Mater. Trans. A*, 37:599, 2006.

[104] Jong-Dae Kim, Suk-Joong L. Kang, and Joo-Wan Lee. Formation of grain boundaries in liquid-phase-sintered WC–Co alloys. *J. Am. Ceram. Soc.*, 88:500, 2005.

[105] Sabine Lay and Jean-Michel Missiaen. Atomic structure of the $\Sigma = 2$ twist carbide grain boundary in WC–Co alloys. *Phil. Mag.*, 93:1146, 2013.

[106] A.E. Johansson, Sven, Martin Petisme, and Göran Wahnström. A computational study of special grain boundaries in WC–Co cemented carbides. *Comp. Mater. Sci.*, 98:345, 2015.

[107] Mikael Christensen and Göran Wahnström. Effects of cobalt intergranular segregation on interface energetics in WC–Co. *Acta Mater.*, 52:2199, 2004.

[108] Mikael Christensen and Göran Wahnström. Co-phase penetration of WC $(10\bar{1}0)$ / WC $(10\bar{1}0)$ grain boundaries from first principles. *Phys. Rev. B*, 97:115415, 2003.

[109] Y. Wang, M. Heusch, S. Lay, and C.H. Allibert. Microstructure evolution in the cemented carbides WC–Co I. Effect of the C/W ratio on the morphology and defects of the WC grains. *Phys. Status Solidi A*, 193:271, 2002.

[110] Arno Meingast, Ernesto Coronel, Andreas Blomqvist, Susanne Norgren, Göran Wahnström, and Martina Lattemann. High resolution stem investigation of interface layers in cemented carbides. *Int. J. Refract. Met. Hard Mater.*, 72:135, 2018.

[111] S. Lay, S. Hamar-Thibault, and A. Lackner. Location of VC in VC, Cr3C2 codoped WC–Co cermets by HREM and EELS. *Int. J. Refract. Met. Hard Mater.*, 20:61, 2002.

[112] S. Lay, S. Hamar-Thibault, and M. Loubradou. Accommodation of the lattice mismatch at the VCx-WC interface. *Interface Sci.*, 12:187, 2004.

[113] S A E Johansson and G Wahnström. Theory of ultrathin films at metal–ceramic interfaces. *Philos. Mag. Lett.*, 90:599, 2010.

[114] S A E Johansson and G Wahnström. A computational study of thin cubic carbide films in WC/Co interfaces. *Acta Mater.*, 59:171, 2011.

[115] S. Lay, J. Thibault, and S. Hamar-Thibault. Structure and role of the interfacial layers in vc-rich wc-co cermets. *Philos. Mag.*, 83:1175, 2003.

[116] K. Mohan and P.R. Strutt. Observation of co nanoparticle dispersions in wc nanograins in WC-Co cermets consolidated from chemically synthesized powders. *Nanostruct. Mater.*, 7:547, 1996.

[117] K. Mohan and P.R. Strutt. Microstructure of spray converted nanostructured tungsten carbide-cobalt composite. *Mater. Sci. Eng., A*, 209:237, 1996.

[118] Paul Arthur Schilpp. *Albert Einstein : philosopher-scientist.* The library of living philosophers: 7. Library of Living Philosophers, 1949.

[119] Bruno Predel, Michael Hoch, and Monte J. Pool. *Phase Diagrams and Heterogeneous Equilibria: A Practical Introduction.* Springer Science & Business Media, March 2013. Google-Books-ID: BPXxCAAAQBAJ.

[120] Leili Gharaee. *First principles study of tungsten-based alloys: From defect thermodynamics to phase diagrams.* PhD thesis, Chalmers University of Technology, 2017.

[121] Patrick R. Cantwell, Ming Tang, Shen J. Dillon, Jian Luo, Gregory S. Rohrer, and Martin P. Harmer. Grain boundary complexions. *Acta Mater.*, 62:1, 2014.

[122] Sven A.E. Johansson and G. Wahnström. First-principles derived complexion diagrams for phase boundaries in doped cemented carbides. *Curr. Opin. Solid St. M.*, 20:299, 2016.

[123] J-O Andersson, Thomas Helander, Lars Höglund, Pingfang Shi, and Bo Sundman. Thermo-calc & dictra, computational tools for materials science. *Calphad*, 26:273, 2002.

[124] R. Shuttleworth. The surface tension of solids. *Proc. Phys. Soc. London, Sect. A*, 63:444, 1950.

[125] L Ramqvist. Wetting of metallic carbides by liquid copper, nickel, cobalt, and iron. *Int. J. Powder Metall.*, 1:2, 1965.

[126] Gene Whyman, Edward Bormashenko, and Tamir Stein. The rigorous derivation of young, cassie–baxter and wenzel equations and the analysis of the contact angle hysteresis phenomenon. *Chem. Phys. Lett.*, 450:355, 2008.

[127] P. Roura and Joaquim Fort. Local thermodynamic derivation of young's equation. *J. Colloid Interface Sci.*, 272:420, 2004.

[128] Lasse Makkonen. Young's equation revisited. *J. Phys. Condens. Matter*, 28:135001, 2016.

[129] M. V. G. Petisme, S. Johansson, and G. Wahnström. Molecular dynamics simulations of WC/WC grain boundary sliding: the effect of thin cobalt films on sliding resistance. *Proceedings of the 18th Plansee Seminar*, 2013.

[130] M. V. G. Petisme, M. A. Gren, and G. Wahnström. Molecular dynamics simulation of WC/WC grain boundary sliding resistance in WC-Co cemented carbides at high temperature. *Int. J. Refract. Met. Hard Mater.*, 49:75, 2015.

[131] M W Finnis. The theory of metal-ceramic interfaces. *J. Phys.: Condens. Matter*, 8:5811, 1996.

[132] Cahn, J. W. Transitions and phase equilibria among grain boundary structures. *J. Phys. Colloques*, 43:C6–199, 1982.

[133] Tetsuya Suzuki, Kunio Shibuki, Toshiyuki Suzuki, and Yuichi Ikuhara. Grain boundary in cemented carbide. *Philos. Mag. Lett.*, 71:289, 1995.

[134] Maxime Pellan. *Development of grain boundaries and phase boundaries in WCCo cemented carbides.* PhD thesis, Université Grenoble Alpes, 2015.

[135] S. A. E. Johansson and G. Wahnström. First-principles study of an interfacial phase diagram in the V-doped WC–Co system. *Phys. Rev. B*, 86:035403, 2012.

[136] Richard Phillips Feynman, Robert B. Leighton, and Matthew Sands. *The Feynman lectures on physics.* Addison-Wesley, 1975.

[137] R.M. Martin. *Electronic Structure: Basic Theory and Practical Methods.* Cambridge University Press, 2004.

[138] M. Born and R. Oppenheimer. Zur quantentheorie der molekeln. *Annalen der Physik*, 389:457, 1927.

[139] P. Hohenberg and W. Kohn. Inhomogeneous electron gas. *Phys. Rev.*, 136:B864, 1964.

[140] W. Kohn and L. J. Sham. Self-consistent equations including exchange and correlation effects. *Phys. Rev.*, 140:A1133, 1965.

[141] A. D. Becke. Density-functional exchange-energy approximation with correct asymptotic behavior. *Phys. Rev. A*, 38:3098, 1988.

[142] John P. Perdew and Yue Wang. Accurate and simple analytic representation of the electron-gas correlation energy. *Phys. Rev. B*, 45:13244, 1992.

[143] J. P. Perdew, K. Burke, and M. Ernzerhof. Generalized gradient approximation made simple. *Phys. Rev. Lett.*, 77:3865, 1996.

[144] R. Armiento and A. E. Mattsson. Functional designed to include surface effects in self-consistent density functional theory. *Phys. Rev. B*, 72:085108, 2005.

[145] John P. Perdew, Adrienn Ruzsinszky, Gábor I. Csonka, Oleg A. Vydrov, Gustavo E. Scuseria, Lucian A. Constantin, Xiaolan Zhou, and Kieron Burke. Restoring the density-gradient expansion for exchange in solids and surfaces. *Phys. Rev. Lett.*, 100:136406, 2008.

[146] M. Dion, H. Rydberg, E. Schröder, D. C. Langreth, and B. I. Lundqvist. Van der waals density functional for general geometries. *Phys. Rev. Lett.*, 92:246401, 2004.

[147] Kyuho Lee, Éamonn D. Murray, Lingzhu Kong, Bengt I. Lundqvist, and David C. Langreth. Higher-accuracy van der waals density functional. *Phys. Rev. B*, 82:081101, 2010.

[148] Kristian Berland and Per Hyldgaard. Exchange functional that tests the robustness of the plasmon description of the van der waals density functional. *Phys. Rev. B*, 89:035412, 2014.

[149] Felix Bloch. Über die Quantenmechanik der Elektronen in Kristallgittern. *Z. Physik*, 52:555, 1929.

[150] P. E. Blöchl. Projector augmented-wave method. *Phys. Rev. B*, 50:17953, 1994.

[151] H. J. Monkhorst and J. D. Pack. Special points for Brillouin-zone integrations. *Phys. Rev. B*, 13:5188, 1976.

[152] M. Methfessel and A. T. Paxton. High-precision sampling for Brillouin-zone integration in metals. *Phys. Rev. B*, 40:3616, 1989.

[153] Peter E. Blöchl, O. Jepsen, and O. K. Andersen. Improved tetrahedron method for brillouin-zone integrations. *Phys. Rev. B*, 49:16223, 1994.

[154] G. Kresse and J. Furthmüller. Efficient iterative schemes for ab initio total-energy calculations using a plane-wave basis set. *Phys. Rev. B*, 54:11169, 1996.

[155] G. Kresse and J. Furthmüller. Efficiency of ab-initio total energy calculations for metals and semiconductors using a plane-wave basis set. *Comp. Mater. Sci.*, 6:15, 1996.

[156] M P Allen and D J Tildesley. *Computer Simulations of Liquids.* Clarendon Press, 1987.

[157] Jan Tobochnik Harvey Gould. *An introduction to computational simulation methods: appplications to physical systems Part I.* Addison-Wesley, 1987.

[158] Jones J. E. On the determination of molecular fields. —ii. from the equation of state of a gas. *Proc. R. Soc. Lond. A*, 106:463, 1924.

[159] Murray S. Daw and M. I. Baskes. Embedded-atom method: Derivation and application to impurities, surfaces, and other defects in metals. *Phys. Rev. B*, 29:6443, 1984.

[160] Murray S. Daw, Stephen M. Foiles, and Michael I. Baskes. The embedded-atom method: a review of theory and applications. *Mater. Sci. Rep.*, 9:251, 1993.

[161] G. C. Abell. Empirical chemical pseudopotential theory of molecular and metallic bonding. *Phys. Rev. B*, 31:6184, 1985.

[162] J. Tersoff. New empirical approach for the structure and energy of covalent systems. *Phys. Rev. B*, 37:6991, 1988.

[163] Donald W. Brenner. Empirical potential for hydrocarbons for use in simulating the chemical vapor deposition of diamond films. *Phys. Rev. B*, 42:9458, 1990.

[164] Karsten Albe, Kai Nordlund, and Robert S. Averback. Modeling the metal-semiconductor interaction: Analytical bond-order potential for platinum-carbon. *Phys. Rev. B*, 65:195124, 2002.

[165] Steve Plimpton. Fast Parallel Algorithms for Short-Range Molecular Dynamics. *J. Comput. Phys.*, 117:1, 1995.

[166] Large-scale atomic/molecular massively parallel simulator. http://lammps.sandia.gov. Accessed: 2018-09-30.

[167] Mattias Ångqvist, William A. Muñoz, J. Magnus Rahm, Erik Fransson, Céline Durniak, Piotr Rozyczko, Thomas H. Rod, and Paul Erhart. ICET – A Python Library for Constructing and Sampling Alloy Cluster Expansions. *Adv. Theory Simul.*, 0:1900015, 2019.

[168] J.M. Sanchez, F. Ducastelle, and D. Gratias. Generalized cluster description of multicomponent systems. *Physica A*, 128:334, 1984.

[169] Atsushi Togo and Isao Tanaka. First principles phonon calculations in materials science. *Scr. Mater.*, 108:1, 2015.

[170] Keivan Esfarjani, Gang Chen, and Harold T. Stokes. Heat transport in silicon from first-principles calculations. *Phys. Rev. B*, 84:085204, 2011.

[171] Keivan Esfarjani and Harold T. Stokes. Method to extract anharmonic force constants from first principles calculations. *Phys. Rev. B*, 77:144112, 2008.

[172] Fei Zhou, Weston Nielson, Yi Xia, and Vidvuds Ozoliņš. Lattice Anharmonicity and Thermal Conductivity from Compressive Sensing of First-Principles Calculations. *Phys. Rev. Lett.*, 113:185501, 2014.

[173] Fei Zhou, Weston Nielson, Yi Xia, and Vidvuds Ozoliņš. Compressive sensing lattice dynamics. i. general formalism. *Phys. Rev. B*, 100:184308, 2019.

[174] Fei Zhou, Babak Sadigh, Daniel Åberg, Yi Xia, and Vidvuds Ozoliņš. Compressive sensing lattice dynamics. ii. efficient phonon calculations and long-range interactions. *Phys. Rev. B*, 100:184309, 2019.

[175] Terumasa Tadano and Shinji Tsuneyuki. Quartic anharmonicity of rattlers and its effect on lattice thermal conductivity of clathrates from first principles. *Phys. Rev. Lett.*, 120:105901, 2018.

[176] Terumasa Tadano and Shinji Tsuneyuki. First-principles lattice dynamics method for strongly anharmonic crystals. *J. Phys. Soc. Jpn.*, 87:041015, 2018.

[177] Fredrik Eriksson, Erik Fransson, and Paul Erhart. The Hiphive Package for the Extraction of High-Order Force Constants by Machine Learning. *Adv. Theory Simul.*, 2:1800184, 2019.

[178] B. J. Alder and T. E. Wainwright. Studies in Molecular Dynamics. I. General Method. *J. Chem. Phys.*, 31:459, 1959.

[179] Daan Frenkel, Berend Smit. *Understanding Molecular Simulation.* Elsevier, 2002.

[180] F. Ercolessi. A molecular dynamics primer. `http://cms.sjtu.edu.cn/doc/reading/md/A_Molecular_Dynamics_Primer_(Ercolessi).pdf`(2020/03/16), 1997.

[181] Loup Verlet. Computer "experiments" on classical fluids. i. thermodynamical properties of lennard-jones molecules. *Phys. Rev.*, 159:98, 1967.

[182] William C. Swope, Hans C. Andersen, Peter H. Berens, and Kent R. Wilson. A computer simulation method for the calculation of equilibrium constants for the formation of physical clusters of molecules: Application to small water clusters. *J. Chem. Phys.*, 76:637–649, 1982.

[183] Mark Tuckerman. *Statistical Mechanics: Theory and Molecular Simulation.* OUP Oxford, 2010. Google-Books-ID: Lo3Jqc0pgrcC.

[184] Nicholas Metropolis, Arianna W. Rosenbluth, Marshall N. Rosenbluth, Augusta H. Teller, and Edward Teller. Equation of state calculations by fast computing machines. *J Chem. Phys.*, 21:1087, 1953.

[185] J. Thijssen. Lecture notes advanced statistical mechanics ap3021g. https://www.scribd.com/doc/219066261/Thijssen-J-Lectures-Notes-Advanced-Statical-Mechanics (2020/03/16), 2008.

[186] E. B. Tadmor and R. E. Miller. *Modeling Materials: Continuum, Atomistic and Multiscale Techniques.* Cambridge University Press, 2011.

[187] H. J. C. Berendsen, J. P. M. Postma, W. F. van Gunsteren, A. DiNola, and J. R. Haak. Molecular dynamics with coupling to an external bath. *J. Chem. Phys.*, 81:3684, 1984.

[188] Shuichi Nosé. A unified formulation of the constant temperature molecular dynamics methods. *J. Chem. Phys.*, 81:511, 1984.

[189] William G. Hoover. Canonical dynamics: Equilibrium phase-space distributions. *Phys. Rev. A*, 31:1695, 1985.

[190] Michael S. Sellers, Martin Lisal, and John K. Brennan. Free-energy calculations using classical molecular simulation: application to the determination of the melting point and chemical potential of a flexible RDX model. *Phys. Chem. Chem. Phys.*, 18:7841, 2016.

[191] John G. Kirkwood. Statistical mechanics of fluid mixtures. *J. Chem. Phys.*, 3:300, 1935.

[192] Alessandra Satta, F. Willaime, and Stefano de Gironcoli. Vacancy self-diffusion parameters in tungsten: Finite electron-temperature lda calculations. *Phys. Rev. B*, 57:11184, 1998.

[193] Olle Eriksson, J. M. Wills, and Duane Wallace. Electronic, quasiharmonic, and anharmonic entropies of transition metals. *Phys. Rev. B*, 46:5221, 1992.

[194] Duane C Wallace. *Thermodynamics of Crystals.* Wiley, 1972.

[195] Brent Fultz. Vibrational thermodynamics of materials. *Prog. Mater. Sci.*, 55(4):247–352, May 2010.

[196] Ling Ti Kong. Phonon dispersion measured directly from molecular dynamics simulations. *Comput. Phys. Commun.*, 182:2201 – 2207, 2011.

[197] Tommy Andersson. *One-shot free energy calculations for crystalline materials.* Master's thesis, Chalmers University of Technology, Gothenburg, Sweden, 2012.

[198] Olle Hellman, Peter Steneteg, I. A. Abrikosov, and S. I. Simak. Temperature dependent effective potential method for accurate free energy calculations of solids. *Phys. Rev. B*, 87:104111, 2013.

[199] Daan Frenkel and Anthony J. C. Ladd. New monte carlo method to compute the free energy of arbitrary solids. application to the fcc and hcp phases of hard spheres. *J. Chem. Phys.*, 81:3188, 1984.

[200] Rodrigo Freitas, Mark Asta, and Maurice de Koning. Nonequilibrium free-energy calculation of solids using lammps. *Comp. Mater. Sci.*, 112:333, 2016.